②

FINAL REPORT

Interface Engineering in Alumina/Glass Composites

Contract No. 89-J-1459
March 1, 1989 - February 29, 1992

Principal Investigator
Prof. K. K. Chawla

Department of Materials and Metallurgical Engineering,
New Mexico Institute of Mining and Technology,
Socorro, NM 87801.

Submitted to
Dr. S. G. Fishman
Project Manager
Office of Naval Research
Arlington, VA 22217.

Statement A per telecon
Dr. Steven Fishman ONR/Code 1131
Arlington, VA 22217-5000

NWW 4/8/92

Accession For	
NTIS GRA&I	☑
DTIC TAB	☐
Unannounced	☐
Justification	
By	
Distribution/	
Availability Codes	
Dist	Avail and/or Special
A-1	

CONTENTS

Executive Summary

List of Figures

List of Tables

1. Introduction
2. Materials
3. Experimental Procedure
4. Results and Discussion
5. Conclusions
6. References

Appendix A: Effect of Tin Dioxide Coating on Tensile Strength of PRD-166 Fibers.
Appendix B: Role of the SnO_2 Interphase in an Alumina/Glass Composite: A Fractographic Study.
Appendix C: Characterization of Tin Dioxide Interphase Coating in an Alumina/Glass Composite.
Appendix D: Effect of Interfacial Roughness and Thermal Stresses in Alumina/Glass and Alumina/Tin Dioxide/Glass Composites.
Appendix E: Effect of Fiber Coating on the Mechanical Properties of a Nextel 480 Fiber Reinforced Glass Matrix Composite.
Appendix F: Effect of Interfacial Roughness on Fiber Pullout in Alumina/Tin Dioxide/Glass Composites.
Appendix G: Effect of Boron Nitride Coating on the Tensile Strength of Nextel 480 Fibers.
Appendix H: Some Observations on the Paper "Influence of Tin Dioxide Interphase on the Residual Stresses in Alumina/Glass Composites."
Appendix I: Report Distribution

EXECUTIVE SUMMARY

The work done in the past three years has demonstrated the feasibility of developing alumina fiber based glass matrix composites for structural applications by applying an interface engineering approach. The composites consisting of a glass matrix containing coated and uncoated continuous alumina type fibers, were produced by slurry impregnation method. A tin dioxide coating was used for the PRD-166 (alumina+zirconia) fiber, while a boron nitride coating was used for the Nextel 480 (alumina+silica+boria) fiber. The coatings were applied by chemical vapor deposition (CVD). Important parameters in the coating process, in order to obtain a uniform coating on the fiber surface, are the deposition temperature and time. Tin dioxide coating forms an effective barrier between alumina and glass, and thereby prevents strong chemical bonding between the components of this composite system.

Significant improvements in the mechanical properties can be achieved by incorporation of such fibers into a brittle matrix. The primary mode of toughening in coated PRD-166/glass composites is crack deflection and fiber bridging while in coated Nextel/glass and Saphikon/glass composites, fiber pullout also occurs. A strong potential exists for enhancing toughness even further provided the surface roughness of the interfaces can be controlled. Preliminary tests carried out on smooth single crystal alumina fiber reinforced glass matrix composites have indicated that extensive fiber matrix debonding and pullout can result with SnO_2 coating.

Nextel 480 fiber reinforced mullite matrix composites were fabricated using a sol-gel precursor route. This method of fabricating the composites produced a fine grained mullite which improved the sinterability of the mullite matrix by lowering the sintering

temperature. This lower sintering temperature aided fabrication of the composites and reduced the thermal damage of the fibers. Mullite/mullite composites are being developed for elevated temperature structural applications.

LIST OF FIGURES

Fig. 1. The interface engineering approach.

Fig. 2. Scanning micrograph of PRD-166 fiber. Note the distribution and size of the zirconia particles (white in the figure). Arrow indicates one such particle.

Fig. 3. Scanning micrograph of Nextel 480 fiber. Note the oval cross section.

Fig. 4. Setup of the CVD process for coating SnO_2.

Fig. 5. Schematic of the slurry impregnation method used in composite fabrication.

Fig. 6. Hot pressing schedule used in composite fabrication.

Fig. 7. Setup used for single fiber testing.

Fig. 8. Specimen configuration used in strength and toughness measurements.

Fig. 9. Optical micrographs of PRD-166/glass composite illustrating the distribution of fibers in the matrix.

fig. 10. Optical micrograph of Nextel 480/glass composite illustrating the distribution of fibers in the matrix.

Fig. 11. Fiber misorientation in PRD-166/glass system.

(a) $V_f = 0.11$ (b) $V_f = 0.4$

Fig. 12. Fiber breakage in PRD-166/glass system.

(a) $V_f = 0.11$ (b) $V_f = 0.4$

Fig. 13. Scanning micrographs of (a) PRD-166/glass fracture surface at two magnifications. Note the flat brittle fracture. SEM.

(b). PRD-166/SnO_2/glass fracture surface at two magnifications. Note

crack branching, partial debonding and crack bridging. SEM.

Fig. 14. Fractographs of (a) uncoated and (b) BN coated Nextel/glass composites illustrating the differences in the extent of bonding and fiber pullout.

Fig. 15. Optical micrograph of a BN coated (0.3 um) Nextel 480/mullite composite produced using a colloidal sol-gel processed mullite powder, illustrating an uniform fiber distribution and high matrix densification.

Fig. 16. Scanning micrograph of a BN coated (0.3 um) Nextel 480/mullite composite produced using a colloidal sol-gel processed mullite powder, showing strong interfacial bonding. 'F' indicates the fiber.

Fig. 17. Change in the morphology of the SnO_2 coating with increasing coating temperature. (a) 500 °C (b) 750 °C

Fig. 18. SIMS analysis of the surface of an SnO_2 coated PRD-166 fiber reinforced glass matrix composite illustrating the Sn^+ and SnO^+ distribution.

Fig. 19. Zr^+, Sn^+, and Al^+ maps of the surface of an SnO_2 coated PRD-166 fiber reinforced glass matrix composite by SIMS.

Fig. 20. Scanning micrograph illustrating the rough nature of the SnO_2 coating on PRD-166 fiber.

Fig. 21. Schematic (a) and scanning micrograph (b) illustrating smoothening of Nextel 480 fiber surface by the BN coating.

Fig. 22. Variation in bend strength with fiber volume fraction for PRD-166/glass and PRD-166/SnO_2/glass composite systems.

Fig. 23. Work of fracture as a function of fiber volume fraction for PRD-

166/glass and PRD-166/SnO_2/glass systems.

Fig. 24. Transverse bend strength versus fiber volume fraction for the PRD-166/glass and PRD-166/SnO_2/glass composites. Transverse fibers perpendicular to the bend plane.

Fig. 25. Transverse bend strength versus fiber volume fraction for the PRD-166/glass and PRD-166/SnO_2/glass composites. Transverse fibers parallel to the bend plane.

Fig. 26. Static fracture toughness as obtained from the Chevron notched specimens for uncoated and SnO_2 coated PRD-166/glass composites as a function of fiber volume fraction.

Fig. 27. Stress-displacement curves for an uncoated and a SnO_2 coated PRD-166/glass composite in a bend test.

Fig. 28. Strength of uncoated and SnO_2 coated PRD-166 fiber composites as a function of temperature.

Fig. 29. Stress-displacement curves for an uncoated and a BN coated Nextel 480/glass composite.

Fig. 30. Fractographs at two magnifications for a BN coated Nextel 480/glass composite exhibiting matrix cracking and fiber pullout.

Fig. 31 Work of fracture of BN coated Nextel/glass composites as a function of coating thickness.

Fig. 32. Strength of uncoated and BN coated Nextel fiber composites as a function of temperature.

Fig. 33. Stress-displacement curves for an uncoated and two BN coated Nextel

480/mullite matrix composites.

Fig. 34. Percent linear change (PLC) versus temperature for (a) uncoated and (b) SnO_2 coated PRD-166/glass composites.

Fig. 35. Percent linear change (PLC) versus temperature for (a) uncoated and (b) BN coated Nextel 480/glass composites.

Fig. 36. Schematic of two- and three-element models used in thermal stress analysis.

Fig. 37. Thermal stress distribution in PRD-166/glass and PRD-166/SnO_2/glass composites.(a) radial stress (b) tangential stress (c) axial stress

Fig. 38. Thermal stresses in the BN coating for a BN coated Nextel 480/glass composite.

Fig. 39. Nanoindentation load-unload curves for (a) PRD-166/glass and (b) PRD-166/SnO_2/glass composite.

Fig. 40. An optical micrograph and a schematic of an indentation crack propagating unimpeded through the PRD-166/glass interface.

Fig. 41. An optical micrograph and a schematic of an indentation crack being deflected at the PRD-166 fiber/SnO_2 coating interface.

Fig. 42. Fiber pullout in the Saphikon/SnO_2/glass composite.

LIST OF TABLES

Table 1. a. Chemical composition of PRD-166 fiber.

b. Physical properties of PRD-166 fiber.

Table 2. a. Chemical composition of Nextel 480 fiber.

b. Physical properties of Nextel 480 fiber.

Table 3. a. Chemical composition of N51 A glass matrix.

b. Physical properties of N51 A glass matrix.

Table 4. Properties of commercial mullite powder used as a matrix material.

Table 5. Properties of SnO_2.

Table 6. Conditions for deposition of SnO_2 by CVD process.

Table 7. Characteristics of colloidal precursors.

Table 8. Weibull parameters of PRD-166 fiber.

Table 9. Weibull parameters of Nextel 480 fiber.

Table 10. Strength of Nextel/glass composites.

Table 11. Static fracture toughness of Nextel/glass composites.

Table 12. Fracture energy of the Nextel/glass composites.

Table 13. Bend strength and work of fracture of the mullite/mullite composites fabricated using a colloidal sol-gel processed mullite powder.

Table 14. Comparison of experimental coefficient of thermal expansion of PRD-166/glass and PRD-166/SnO_2/glass composites with the theoretical predictions of various models.

Table 15. Roughness amplitude (A), fiber radius (rf) and (A/rf) ratio for PRD-166 and Saphikon fibers.

1. INTRODUCTION

Ceramics and glasses exhibit relatively high thermal stability combined with low density and chemical inertness as compared to metals and polymers. However, they fail to find wide application in structural applications because of their brittle nature. Incorporation of high strength and high modulus fibers is a very promising method of improving the toughness of such brittle ceramics. This increase in the toughness results from various energy absorbing mechanisms such as fiber/matrix debonding, crack deflection, crack bridging, and fiber pullout, induced by the introduction of the fibers into the matrix. Such mechanisms of toughening have been studied extensively in various composite systems, and have been documented in literature [1-3].

Of the various fibers which can be potentially used as reinforcements for ceramic or glass matrices, alumina-based fibers are one of the most promising. They possess adequate strength and stiffness. Unlike carbon fibers, alumina based fibers possess excellent thermal stability in oxidizing atmospheres even at elevated temperatures. They are also superior as compared to SiC based fibers, which have a tendency to decompose and react in the presence of glass matrices [4,5]. However, one of the drawbacks of such alumina based fibers is their high reactivity with silica. The alumina fibers react very strongly with silica if present in the matrix, consequently forming a strong chemical bond [6-8]. Such a strong bond is not conducive to toughening processes such as fiber/matrix debonding, crack deflection, crack bridging, and pullout. As a result such alumina based fibers are unsuitable for use with glass and other silica containing matrices. The easiest and most versatile method of preventing such a reaction between the fiber and matrix, is by the application of a coating on the fiber surface. Such a coating would act as a diffusion barrier between the fiber and matrix, and thereby prevent chemical reaction between the two components. Consequently, the resultant bonding will be weak in this case. A judicious choice of a coating material is very important. Such an interface engineering approach is shown in Fig. 1.

Solubility studies indicate that tin dioxide has no solubility in alumina as and is only slightly soluble in silica [9,10]. This non-solubility between tin dioxide and alumina promotes a relatively weak bonding between the fiber and coating, and produces conditions suitable for enhanced toughness. The main propagating crack in such a system would be expected to deflect along the weak fiber/coating interface. Additionally, fiber/matrix debonding and fiber pullout would also be major contributors to the toughness of the composite.

Another material of interest as a fiber coating in such (alumina+silica)-based fiber/silica-based matrix composites is boron nitride. Boron nitride is very widely used as a high temperature lubricant and has also been shown to be effective as a fiber coating for ceramic matrix composites [11-13].

Work done in the last three years has demonstrated the feasibility of using such coatings effectively. These studies include specimen fabrication, extensive mechanical property characterization, interface and coating characterization, and, last but not least, a thermal stress analysis. Details of these studies are documented below.

2. MATERIALS

PRD-166 fiber (DuPont) was primarily used in most of the studies. PRD-166 is an α-alumina based fiber containing 15-20 v/o of yttria stabilized tetragonal zirconia particles, Fig. 2. The average grain size of the alumina was about 0.5 μm and that of the zirconia particles about 0.3 μm. Nextel 480 (3M Co.) fiber which is essentially a mullite fiber containing small amounts of boria, was also studied. This fiber has an oval cross section, Fig. 3. Both uncoated and BN coated fibers were obtained from 3M Co. In addition to these two fibers, single crystal alumina (Saphikon) fiber was also used in a few experiments. Details of the physical and mechanical properties of the PRD-166 and Nextel 480 fibers are provide in Tables 1 and 2, respectively.

N51A glass (Owens Illinos) was used as a matrix in these composites. The nominal composition and physical properties of the N51A glass are given in Table 3. Mullite powder was also used as the matrix for a few samples. The mullite powder was obtained commercially and was also produced by a colloidal sol-gel route. Details of the commercially obtained mullite powder are provided in Table 4.

Bulk alumina (99.7%) required for some initial testing was obtained in the form of bars from Coors Porcelain Co.

The choice of tin dioxide as an interphase between alumina and glass follows the work of Maheshwari et al. [6]. Tin dioxide was chosen because it shows no solubility with alumina up to 1400 °C, and very little solubility in glass. These results have been confirmed by quantitative electron microprobe work. The CVD process of coating tin dioxide was used for coating the fibers. Properties of tin dioxide are listed in Table 5.

3. EXPERIMENTAL PROCEDURE

3.1. CVD of tin dioxide:

After various trials, the CVD setup shown in Fig. 4 was used. The reaction vessel was an alumina tube, 50 cm long and 5 cm in diameter. Dry nitrogen was used as a carrier gas for $SnCl_4$ at a flow rate of nitrogen at 1 liter/min. Oxygen was passed at a rate of 0.6 liter/min through water heated to 80 °C. The alumina fiber tows were placed in the central hot zone of the reactor. The deposition was done for 5 minutes at 500° C. The final conditions for the deposition of SnO_2 are given in Table 6. The deposition occurs as per the chemical reaction given below.

$$SnCl_4(l) + 2H_2O(g) = SnO_2(s) + 4HCl(g)$$

Additional details of the coating process can be obtained from ref.[11] in Appendix C.

3.2. Fabrication of glass matrix composites

Alumina fiber reinforced glass matrix composites were fabricated using a slurry impregnation technique [2]. A schematic of the fabrication process is shown in Fig. 5. The amount of glass in the slurry, rate at which the fibers are pulled through the slurry, variation in the composition of the slurry, and the amount of agitation used to mix the slurry, all control the final properties of the composite obtained. The slurry consisted of glass frit, 2-propanol, and an organic binder to impart green strength to the tapes and facilitate their handling. The typical proportion of binder to frit to 2-propanol was 0.25:1:3 by volume.

A continuous fabrication process was used for making the unidirectional tapes. The fiber tows were impregnated with 325 mesh glass frit and laid out on mylar sheets to form the prepegs. The tapes were peeled off the mylar tape, cut, stacked, and heated to 500 °C in air to remove the binder. This was followed by hot pressing in a graphite lined die in argon atmosphere at a temperature of 925 °C and pressure of 3 MPa. The hot pressing schedule used is shown in Fig. 6. Additional details of the process are given in ref. [3] in Appendix E.

3.3 Fabrication of mullite matrix composites

Fabrication of mullite fiber reinforced mullite matrix composites was pursued by a sol-gel route. Use of commercially available mullite powder results in a theoretical density of 92% when hot pressed at 1500 °C. These temperatures are relatively on the higher side. It is necessary to be able to fabricate such composites at lower temperatures in order to reduce degradation to the fibers. Sintering of commercially available mullite powders does not give the desired density and mechanical properties when sintered at temperatures below 1500 °C.

Sol-gel processing offers a viable alternative to conventional pressing techniques for producing such composites for elevated temperature structural use. The polymeric based sol-gel precursor route can be used to produce fine powders and thereby reduce the densification temperature to around 1250 °C. However, the major drawback of this technique is the careful drying procedure required, when used as a matrix.

The colloidal sol-gel processed powders overcome the disadvantages of the above mentioned process, at the same time retaining the advantages of the sol-gel technique. Fabrication of the mullite matrix composites was undertaken using this approach. Characteristics of the precursors used are given in Table 7. The mullite powder produced by the sol-gel precursor route was fabricated as per the process described above in 3.2.

3.4 Microstructural examination

Optical and scanning electron microscopy were used for general characterization of the microstructure of the composites to determine the volume fraction and distribution of the fibers in the matrix. SEM was used to evaluate the grain size of alumina and the zirconia particle size in the PRD-166 fibers. The fracture surfaces of the as received and coated fibers were also characterized by an SEM coupled with an Energy dispersive analysis system (EDS). Secondary ion mass spectroscopy (SIMS) was also used to characterize the microstructure. SIMS is a technique of mass spectrometry of ionized particles. When a flux of primary ions is directed on the specimen to be analyzed, a high yield of secondary ions can be obtained under appropriate conditions. These secondary ions are analyzed by a mass spectrometer to give a mass spectrum of the surface under examination. This technique inspite of its excellent elemental sensitivity has not been applied extensively to characterize ceramic materials. This is mainly because ion bombardment of ceramics and other insulating materials results in a charge buildup on the sample surface. This charge build up can affect the material response.

The dynamic SIMS used in this study uses a fine primary ion beam (less than 100 microns) to sputter the sample. The beam has a moderate energy (1-20 keV) and current (1-10 nA). The primary ion beam source can be cesium, gallium or argon. The secondary ions are ejected from the specimen during sputtering, and analyzed in a mass spectrometer.

3.5 Mechanical Property testing

Various mechanical tests done in this project are described below.

3.5.1. Single fiber testing

Single fiber testing was carried out on uncoated and coated fibers in order to verify the strength and to examine the effect of the coating on the fiber strength. The setup used to measure the single fiber strength is shown in Fig. 7. The tests were done by mounting individual fibers on a paper frame. The sides of each frame were carefully cut after the assembly was gripped in the tensile testing machine. An Instron machine with a 5 N load cell and a cross head speed of 0.1mm/s was used. Additional details are given in ref. [9] in Appendix A.

3.5.2. Indentation testing

Indentation machines with highly resolved load and displacement sensing capabilities, called nanoindentor machines, have recently become available. Such machines can provide quantitative information from very small areas. These machines are especially useful in determining fiber/matrix interfacial strengths. Nanoindentation tests were carried out on the PRD-166/glass and Nextel 480/glass systems in order to determine the interfacial bonding and to study the interaction between the matrix crack and the fiber and coating.

3.5.3. Mechanical strength and toughness

Three-point and four-point bend tests were used to evaluate the strength of the coated and uncoated fiber composites. Static fracture toughness measurements were done on Single Edge Notched Beam (SENB) specimens in accordance with Ref. [14]. Chevron notched samples were also used in evaluating the static toughness. The specimen configurations used are shown in Fig. 8. The work of fracture was determined from the area under the load -displacement curves [15]. Other details of the testing procedures used are given in ref. [6] in Appendix E.

3.5.4. Thermal expansion behavior

Thermal expansion behavior of various composites produced was studied using an Orton dilatometer, model 1000 D. The thermal expansion was recorded by an LVDT. The LVDT used in this particular apparatus had a linear resolution of ± 0.25 % of the total LVDT range of 0.318 cm, and a repeatability of 6.25×10^{-4} cm.

4. RESULTS AND DISCUSSION

4.1 Microstructural characterization

Optical micrographs of the polished surfaces of uncoated PRD-166/glass and Nextel 480/glass composites are shown in Figs. 9 and 10 respectively. Note the distribution of fibers within the matrix. Studies carried out on the PRD-166/glass and PRD-166/SnO_2/glass systems revealed some interesting information about the fiber misorientation. Increasing the volume fraction of the fibers was found to result in less misorientation. However, the amount of fiber breakage was found to increase with volume fraction. The data on misorientation and fiber breakage measured for two different volume fractions of 11% and 40% are summarized in Figs. 11 and 12, respectively. These studies are important in determining the overall fiber contribution to the composite strength, because the fiber orientation and fiber length can affect the composite properties significantly.

Scanning micrographs of the fractured surfaces of the uncoated and SnO_2 coated PRD-166/glass and uncoated and BN coated Nextel 480/glass matrix composites are provided in Figs. 13 and 14 respectively. Note the strong bonding between the uncoated fibers and the matrix (in case of the PRD-166/glass and Nextel 480/glass systems). Introduction of the fiber coatings results in weakening of the fiber/matrix interface. As a results the fracture features observed in the case of the uncoated fiber composites are inherently brittle in nature, while the features observed in case of the coated fiber composites exhibit more graceful characteristics.

The sol-gel precursor route resulted in a Nextel 480 fiber/mullite matrix composite having a theoretical density of 96%, incorporating 16 volume percent of fibers. Scanning micrograph in Fig. 15 illustrates the uniform distribution of fibers obtained in the composite. The BN coating applied to the fibers disappeared during the fabrication process. Coating thicknesses as much as 0.3 μm was found to be assimilated during fabrication. Extensive damage was also caused to the fibers during the fabrication process, Fig. 16.

4.1.1. Characterization of SnO_2 interphase

A detailed metallographic investigation of the tin dioxide interphase produced at different temperatures and different times was made. Hydrogen Iodide was used as an etchant to reveal the grain structure and shape. The details of this work have been published and are provided in ref. [6] in Appendix C. Low temperature (500 °C) resulted in uniform columnar grain growth, while higher temperatures (750 °C) resulted in an irregular lateral growth Figure 17. Increasing the deposition time at either of these temperatures resulted in extended columnar growth. A temperature of 500 °C and deposition times of the order of 5 min was found to produce the most desirable structure.

Results of the SIMS characterization of the microstructure of the PRD-166 fiber/tin dioxide/glass matrix composite are shown in Figs. 18 and 19. In Fig. 18, the Sn^+ and SnO^+ maps can be seen in the top half. The Sn in the coating is localized to the coating only. No diffusion into the fiber or matrix is apparent. An SEM picture of the mapped region can be seen in the bottom half of the same picture.

Maps of Zr^+, Sn^+, and Al^+ are shown in Fig. 19. As is evident from the map, the zirconia is restricted to the fiber only. Note also that there is no outward diffusion of Zr from the PRD-166 fiber into the coating or the matrix.

4.2 Single fiber testing

The as received alumina fibers showed a Weibull mean strength of 1375 MPa, while the SnO_2 coated fibers exhibited a decreasing tensile strength with increasing coating thickness. The loss in the strength of the tin dioxide coated PRD-166 fibers is attributed to exposure of the fibers to elevated temperatures during the deposition process, and the thermal stresses generated during the deposition of the tin dioxide coating. In addition the roughness of the coating created stress concentration sites, which in turn further reduced the strength of the coated fibers, Fig. 20. Detailed observations and single fiber testing of coated and uncoated PRD-166 fibers are given in Table 8.

The uncoated Nextel 480 fibers exhibited a Weibull mean strength of 1766 MPa. The strength of these fibers was found to increase significantly with the application of the coating. This large increase in the strength is attributed to the smoothening of the rough surface of the fibers by the application of this coating. Unlike the rough SnO_2 coated PRD-166 fibers, the smooth BN coating has a "crack healing" effect on the fiber surface, thereby effectively reducing the size of the flaw on the fiber surface. Other details of the Weibull analysis are provided in Table 9. Scanning micrograph in Fig. 21 illustrates the fiber surface healing effect by the BN coating.

4.3 Strength and toughness measurement

The results of room temperature three-point bend strengths of coated and uncoated alumina fiber composites in the longitudinal direction as a function of volume fraction of fibers are presented in Fig. 22. A significant strengthening was obtained by incorporating the fibers into the glass matrix. The work of fracture associated with these fractured samples increased with fiber volume fraction, Fig. 23.

Transverse bend strength results, for two different orientations of uncoated and coated PRD-166 fiber/glass composites, are presented in Figs. 24 and 25, respectively. The transverse bend strength was, not unexpectedly, significantly lower than the longitudinal bend strength. The transverse bend strength increased with fiber volume fraction up to a certain point, and decreased thereafter. Reasons for this anomalous behavior are still under investigation.

The static fracture toughness as determined by using the maximum load criterion increased with fiber volume fraction, Fig. 26. The fracture energy determined from the load displacement curves also increased with the strength. The stress-displacement curves for the uncoated and SnO_2 coated fiber composites are shown in Fig. 27.

The elevated temperature tests carried out on uncoated and coated fiber composites revealed that the strength of these composites decreased with increasing temperatures, Fig. 28. This was attributed to the weakening of the parent glass matrix.

Results of the strength of the uncoated and coated Nextel 480/glass composites are presented in Table 10. The strength of the coated composites increased slightly over the unreinforced glass matrix. The reason for this lack of increase in the strength of the composite is still under investigation.

The toughness values of the Nextel 480 composites are presented in Table 11 while the fracture energy of the composites is tabulated in Table 12. The fracture energy of the BN coated fiber composites was significantly higher than that of the uncoated fiber composite. The failure of a BN coated fiber composites was far more graceful as compared to the brittle characteristics exhibited by the uncoated fiber system, Fig. 29. Extensive matrix cracking and fiber pullout were major contributors to the energy absorbed by the composite, as can observed in Fig. 30. The work of fracture of these BN coated fiber composites increased with coating thickness, Figure 31. This was as a result of the healing process of the fiber surface.

Elevated temperature tests revealed that the strength of such BN coated fiber composites actually increased with increasing temperature up to 400 °C and decreased thereafter, Figure 32. This is probably as a result of enhanced interfacial bonding with matrix softening. Above a certain temperature however, the matrix weakens substantially and the composite strength drops.

Summary of the mechanical tests carried out on the Nextel fiber/mullite matrix composites produced by the sol-gel precursor route are given in Table 13. The strength in bending and the work of fracture of these composites were significantly improved over the unreinforced mullite matrix. For a BN coating thickness of up to 0.3 um, the bonding between the fibers and matrix was very strong and the composite failure characteristics were brittle in nature. Increasing the coating thickness to 1 microns was found to remedy the problem as can be seen from the stress-displacement curves in Fig. 33. This study is still in progress.

4.5 Thermal expansion measurements

The coefficient of thermal expansion of the composites was determined from the thermal expansion curves. Results of the thermal expansion measurements carried out on the PRD-166/glass and Nextel 480/glass composite systems are presented in Figs. 34 and 35, respectively. The thermal expansion coefficients for the uncoated and SnO_2 coated PRD-166/glass composites have been compared with the theoretically predicted values of various models for fiber reinforced composites in Table 14. Of all the models, Schapery's model appears to fit the experimental data the best. It is also worthwhile noting that the difference between the experimental and theoretical values is relatively larger for the uncoated fiber composite system. This is because absence of the coating will in all likelihood lead to formation of a reaction zone at the fiber/matrix interface, thereby affecting the overall composite expansion.

4.6 Effects of thermal stress

Effects of fiber/matrix processing induced thermal stresses and interface roughness in PRD-166 fiber/glass and PRD-166/SnO_2/glass matrix composites were evaluated using two- and three-element models, Fig. 36. Thermal stress analysis showed radial tensile stress at the fiber/coating and coating/matrix interfaces, Fig. 37. A study of indentation cracks showed that the interfacial radial tensile stress combined with the relatively weak mechanical bonding between alumina and tin dioxide provided conditions propitious for crack deflection, a desirable feature from a toughness point of view. However, the tin dioxide coated PRD-166 fiber/glass matrix composite did not exhibit any sliding in the nanoindentation test. This was attributed to the fiber surface roughness induced compressive radial stress which was an order of magnitude larger than the thermal tensile radial stress.

A similar thermal stress analysis was also carried out on the BN coated Nextel 480/glass composites. In this case the thermal stresses existing at the interfaces were minimal. Results of the analysis for the BN coated Nextel fiber composites are given in Fig. 38.

Details of the thermal stress analysis carried out are provided in Appendix D.

4.7 Indentation testing

The results of the indentation tests performed are shown in Fig. 39 for the coated and uncoated fiber composites. No sliding was obtained in the coated and uncoated PRD-166 glass matrix systems, although some sliding was detected in the BN coated Nextel 480/glass system. However a major limitation of the equipment used was its maximum load capacity, which was probably the reason we did not cause any sliding in the PRD-166/glass system. However, this fact does not undermine the strong bonding existing in the system.

Figures 40 and 41 illustrate the interaction of a matrix crack (introduced by indentation) with the fiber/matrix interface in the PRD-166/glass and PRD-166/SnO_2/glass systems, respectively. The tensile residual stresses at the interface are not effective in deflecting the matrix crack because of the strong chemical bonding existing between the fiber and matrix in the PRD-166/glass system. On the other hand, the SnO_2 coating when present on the fiber surface reduces the extent of bonding, thereby creating conditions suitable for crack deflection (at the fiber/coating interface). The fact that the crack tends to follow the inner circumference, i. e., the fiber/SnO_2 coating interface, is understandable inasmuch as the fiber/SnO_2 coating interface is purely mechanical in nature while there may be some chemical bonding between SnO_2 and glass.

4.8 Surface roughness effects

The surface of the fiber has a pronounced effect on the debonding and pullout characteristics of the alumina/glass system. This was demonstrated by incorporating relatively smooth single crystal fiber alumina fibers (Saphikon) in the glass matrix. Fracture surface of these samples showed extensive fiber/matrix debonding and pullout. The average pullout length in these Saphikon/SnO_2/glass composites was 106 μ, which was five times larger than that in the PRD-166/SnO_2/glass composite. The important point to note here is that the pullout occurred at the fiber/coating interface. This is expected since SnO_2 and alumina have no mutual solid solubility and the interface is weak in the absence of roughness-induced clamping. However, SnO_2 does have some solubility in glass. These features can be observed in Fig. 42.

Surface roughness parameters were determined for PRD-166 and Saphikon fibers. Details of the surface roughness parameters are given in Table 15. The ratio of the average surface asperity to the radius of the fiber was 0.064 for the uncoated PRD-166 fiber and 0.009 for the uncoated Saphikon fiber. The asperity ratio for the SnO_2 coated PRD-166 fiber was 0.05, and for the SnO_2 coated Saphikon was 0.047.

5. CONCLUSIONS

The work done during this project has demonstrated the feasibility of successfully using tin dioxide as a coating for alumina fiber-based glass matrix composites. Although chemical bonding between the fiber and matrix was suppressed by the presence of the coating, mechanical keying between the components (PRD-166 fiber and tin dioxide) because of the rough fiber surface provided adequate load transfer, but also inhibited some of the energy absorbing processes such as fiber pullout, which are necessary for a full realization of the toughness enhancement potential. This was demonstrated in a composite containing a relatively smooth fiber such as Saphikon. The fracture surface in these composites exhibited extensive crack deflection and neat fiber pullout, thereby illustrating the interface engineering approach utilized in this project for toughness enhancement by incorporating a relatively weak interface.

Boron nitride was as a coating for the Nextel 480/glass composite system. The presence of boron nitride weakened the fiber/matrix interface sufficiently to induce a large amount of matrix cracking and extensive fiber pullout. The fracture energy of these composites was significantly enhanced (by a factor of 15) due to the incorporation of the fibers, without significantly reducing the strength of the composites.

The sol-gel precursor technique has been shown to be very effective in improving the sinterability of mullite matrix based composites. The matrix powder obtained by such a technique had a fine size and aided in the fabrication process.

6. REFERENCES

1. K. K. Chawla, **Composite Materials: Science and Engineering**, Springer Verlag, New York, 1987.
2. K. M. Prewo, J. J. Brennan, and G. K. Layden, Am. Ceram. Soc. Bull., **65** (1986) 305.
3. R. Levitt, J. Mater. Sci., **8** (1974) 1847.
4. T. Mah and H. A. Lipsitt, J. Mater. Sci., **19** (1984) 1191.
5. J. J. Brennan and K. M. Prewo, J. Mater. Sci., **17** (1982) 2317.
6. A. Maheshwari, K. K. Chawla, and T. A. Michalske, Mater. Sci. Engg., **A107** (1989) 269.
7. T. A. Michalske and J. J. Hellmann, J. Am. Ceram. Soc., 71 (1988) 725.
8. J. L. Keddie and T. A. Michalske, SANDIA Report **SAND 87-1884, UC-25,** Sandia National Laboratory, New Mexico, Jan. 88.
9. L. J. Manfredo and R. N. McNally, J. Am. Ceram. Soc., **67** (1984) C 155.
10. V. J. Barczak and R. H. Insey, J. Am. Ceram. Soc., **45** (1962) 144.
11. F. D. Gac, LOS ALAMOS Report **LA 11592-T,** Los Alamos National Laboratory, New Mexico, 1989.
12. R. N. Singh and S. B. Giddipali, J. Am. Ceram. Soc., **71** (1988) C 100.
13. M. K. Brun and R. N. Singh, Adv. Ceram. Mater., **3** (1988) 553.
14. G. K. Bansal asd W. H. Duckworth in **Fracture Mechanics Applied to Brittle Materials**, ASTM Special Technical Publication 678, edited by

S. W. Freiman, American Socity for Testing and Materials, Philadelphia, 1979, pp. 38-46.

15. D. C. Phillips, J. Mater. Sci., 7 (1972) 1175.

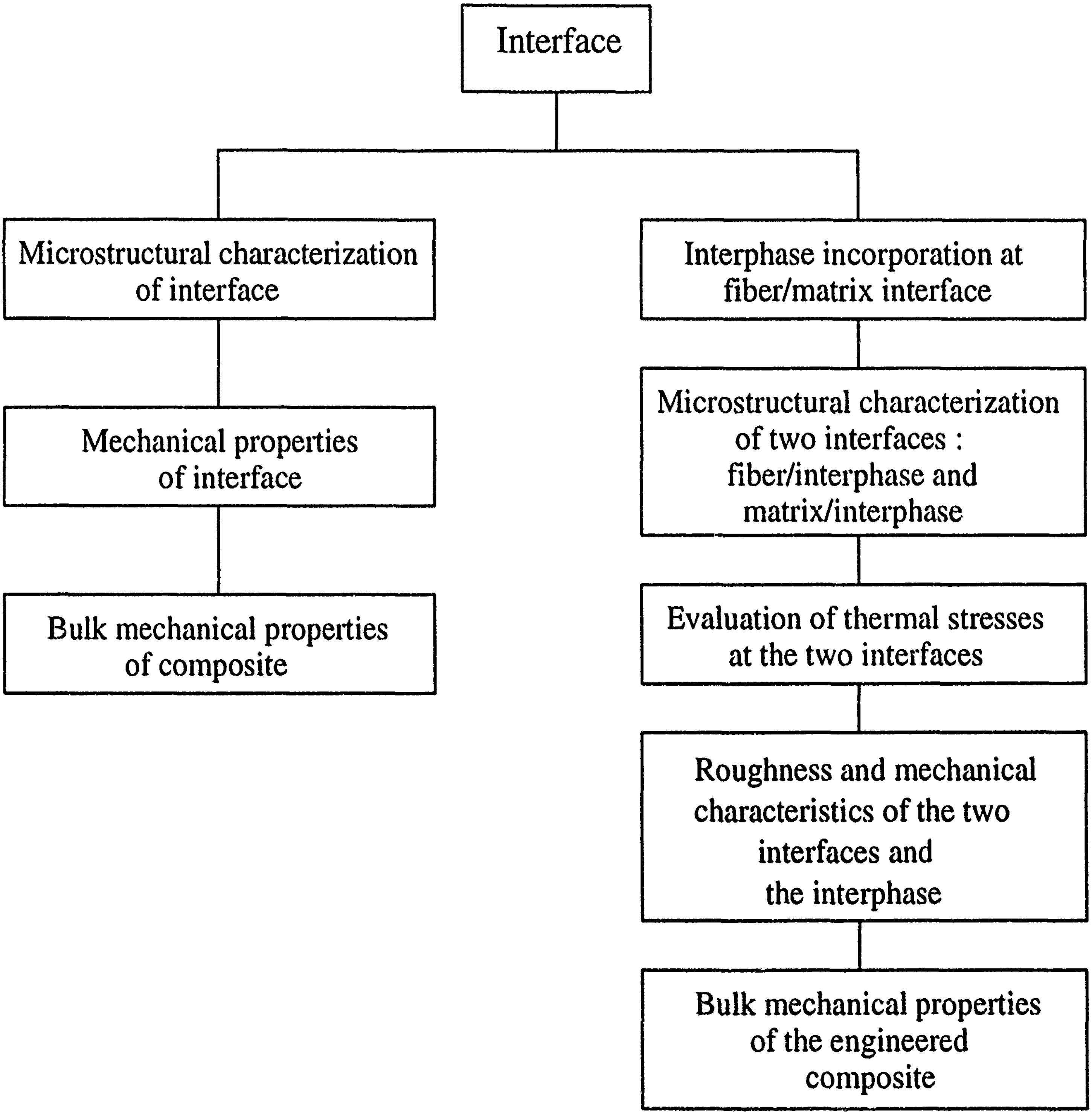
Interface
Microstructural characterization of interface
Mechanical properties of interface
Bulk mechanical properties of composite
Interphase incorporation at fiber/matrix interface
Microstructural characterization of two interfaces : fiber/interphase and matrix/interphase
Evaluation of thermal stresses at the two interfaces
Roughness and mechanical characteristics of the two interfaces and the interphase
Bulk mechanical properties of the engineered composite

Figure 1

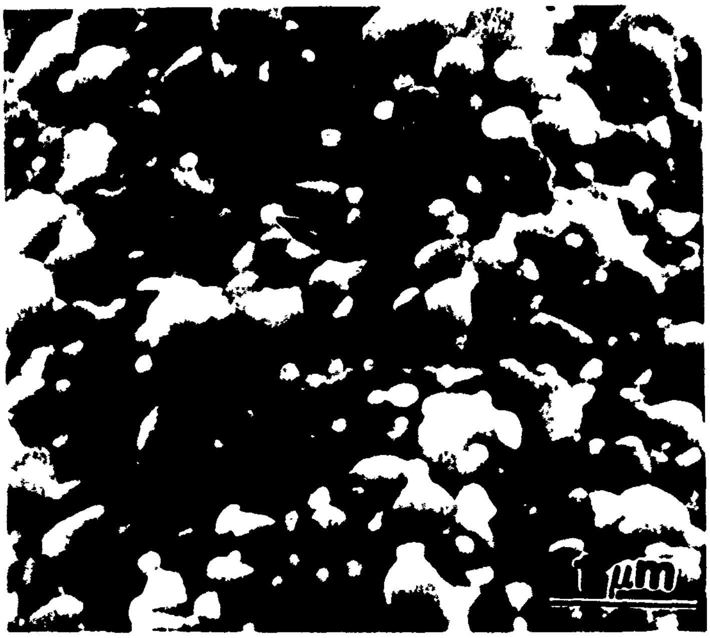

Figure 2

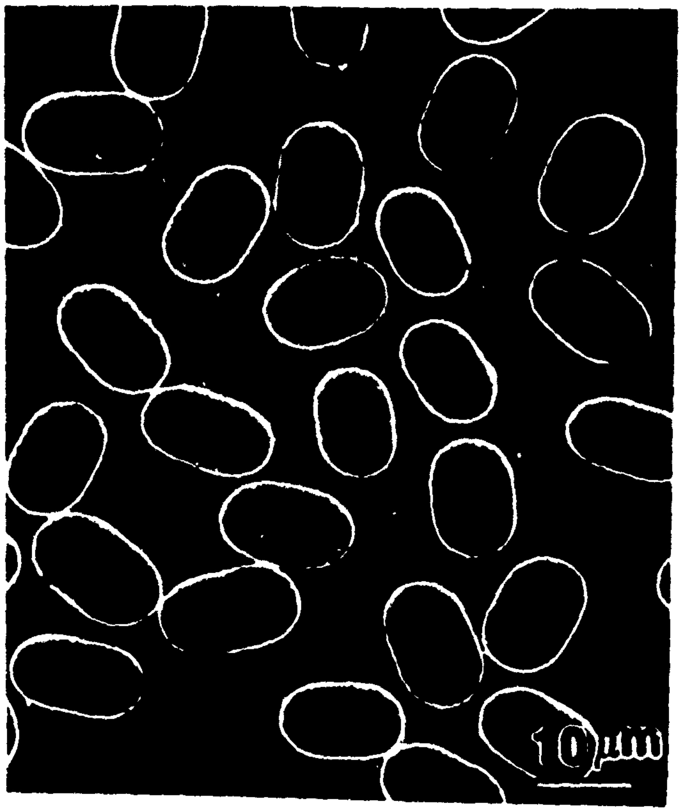

Figure 3

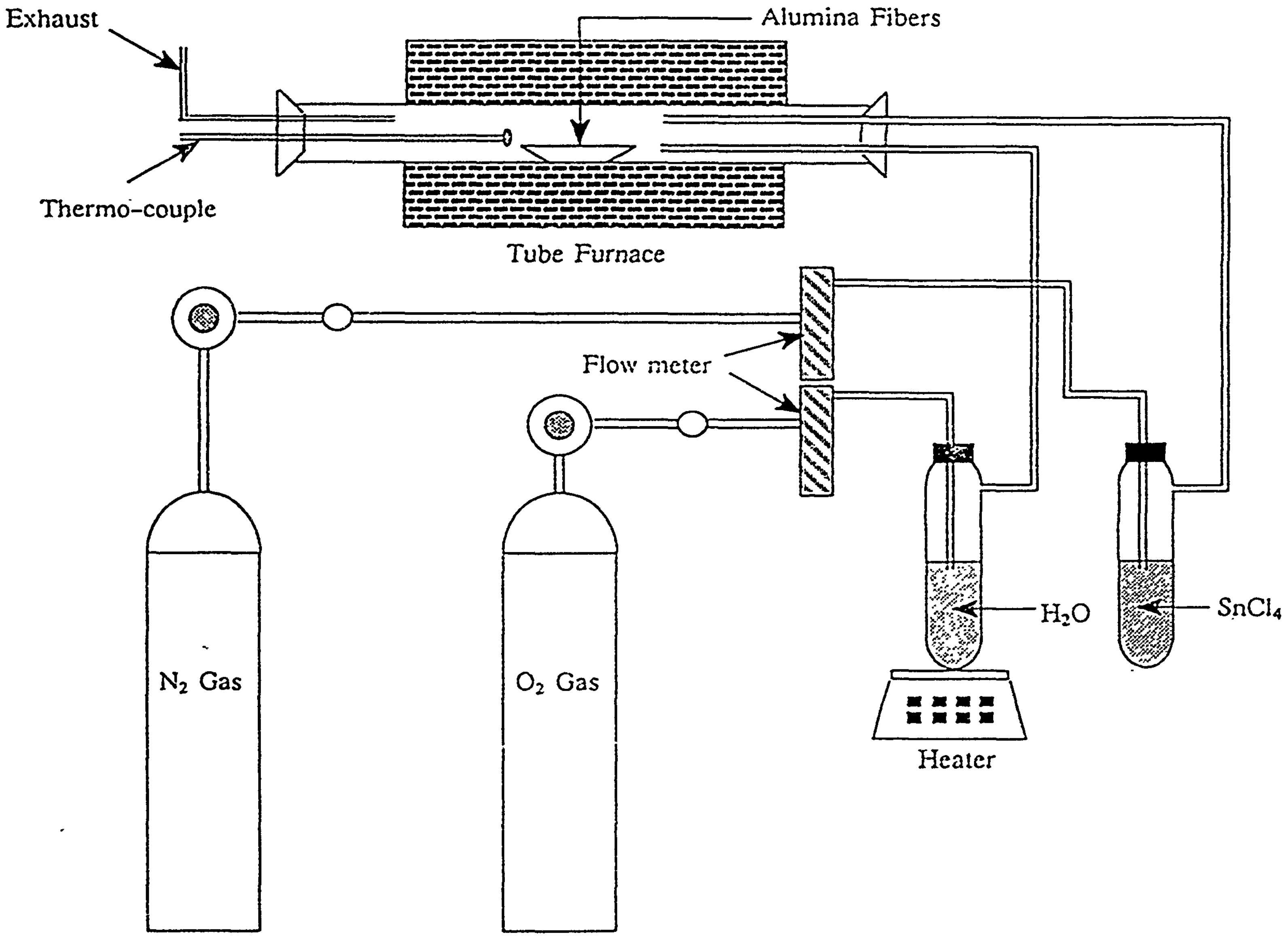
Exhaust
Alumina Fibers
Thermo-couple
Tube Furnace
Flow meter
H_2O
$SnCl_4$
Heater
N_2 Gas
O_2 Gas

Figure 4

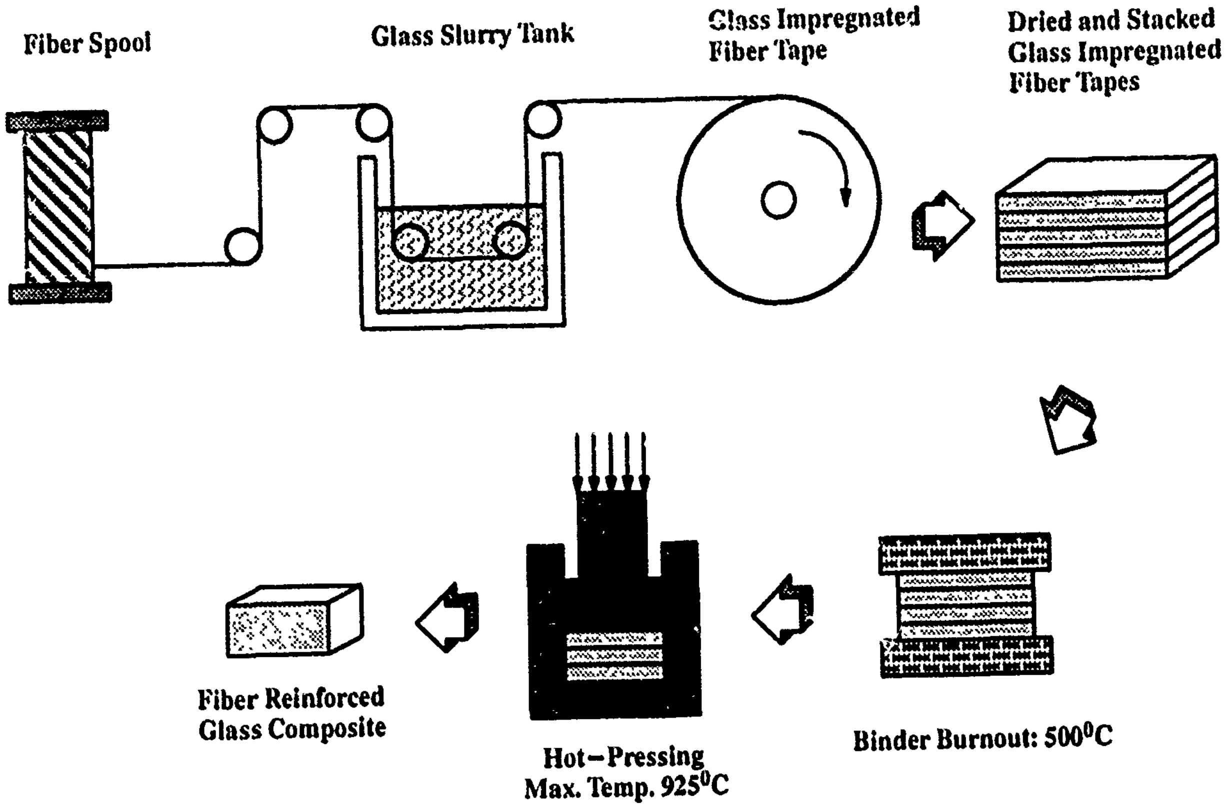
Fiber Spool
Glass Slurry Tank
Glass Impregnated Fiber Tape
Dried and Stacked Glass Impregnated Fiber Tapes
Binder Burnout: 500°C
Hot-Pressing Max. Temp. 925°C
Fiber Reinforced Glass Composite

Figure 5

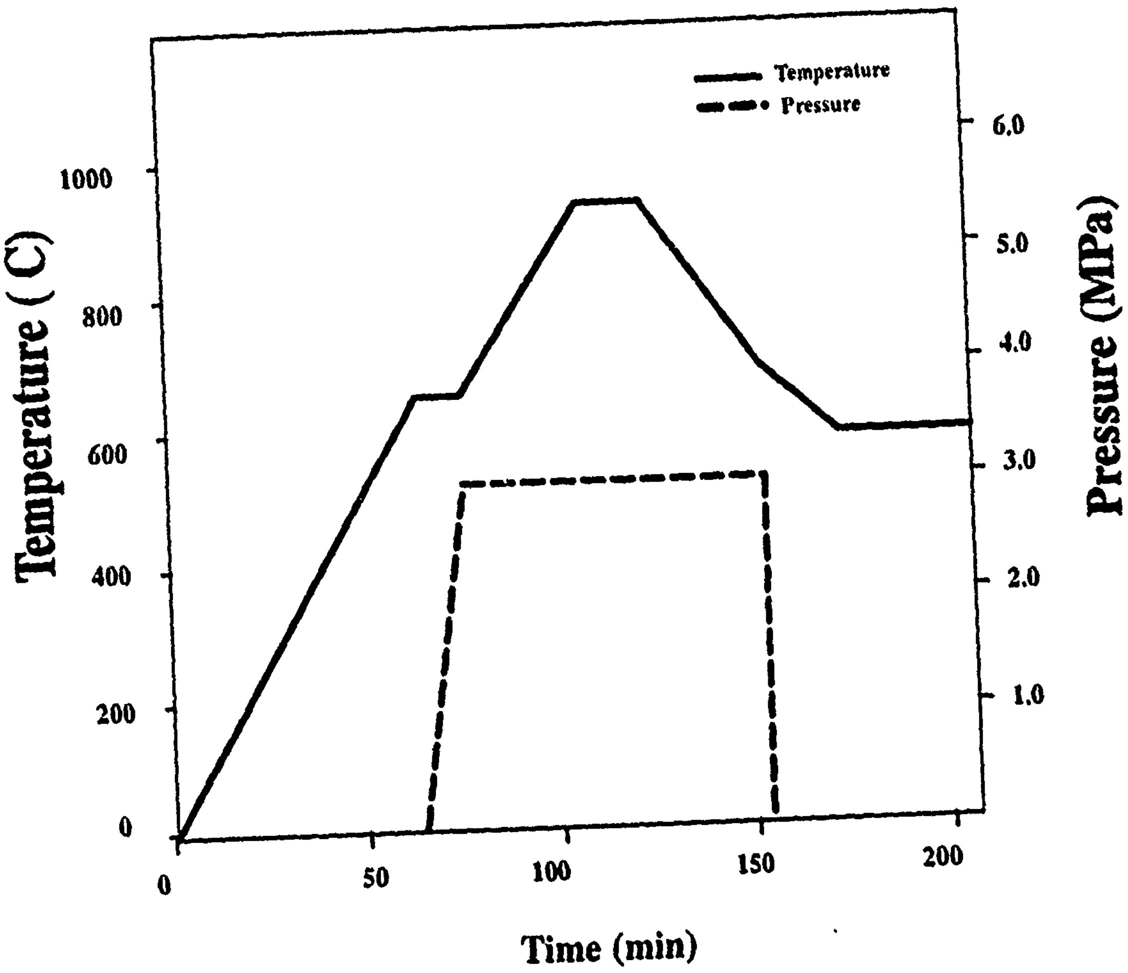
Temperature
Pressure
Temperature (C)
1000
800
600
400
200
0
Pressure (MPa)
6.0
5.0
4.0
3.0
2.0
1.0
0
50
100
150
200
Time (min)

Figure 6.

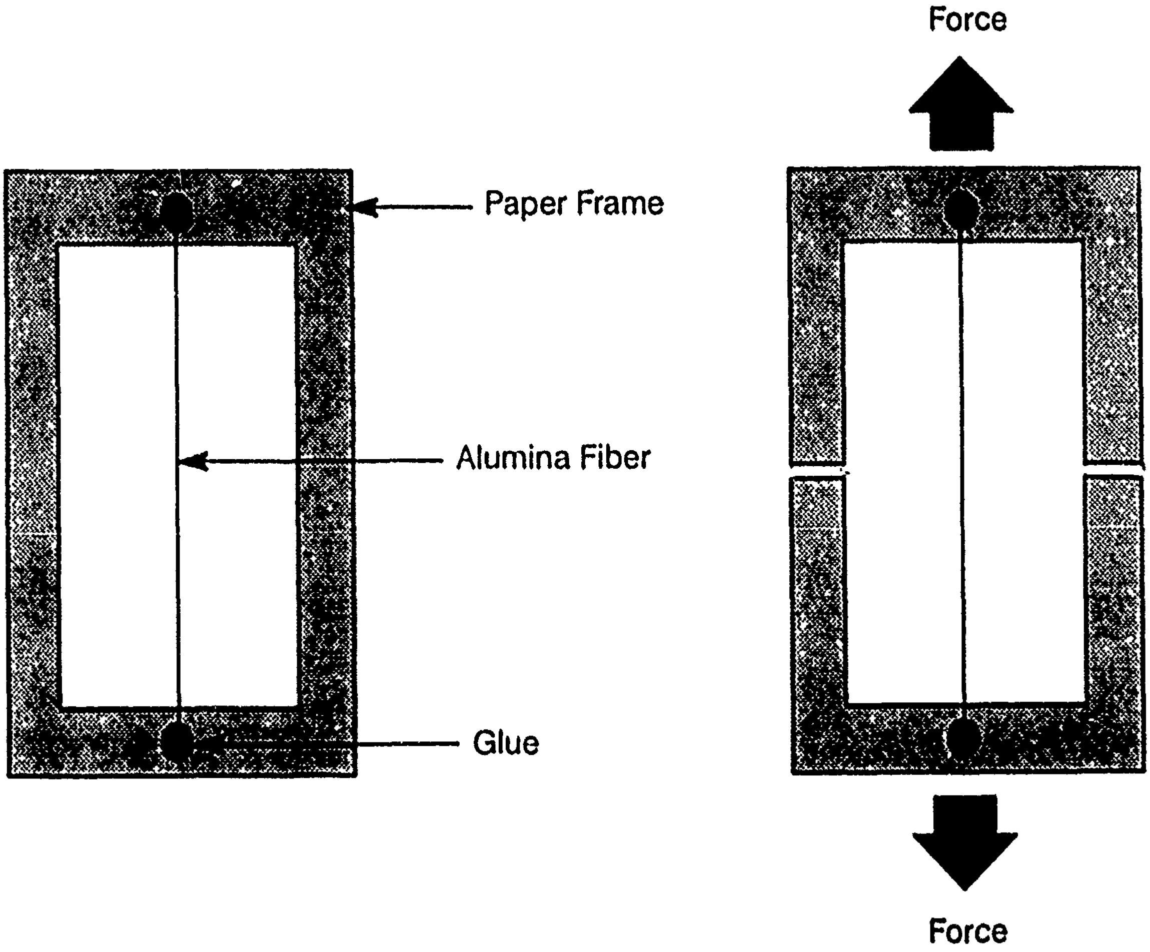

Figure 7

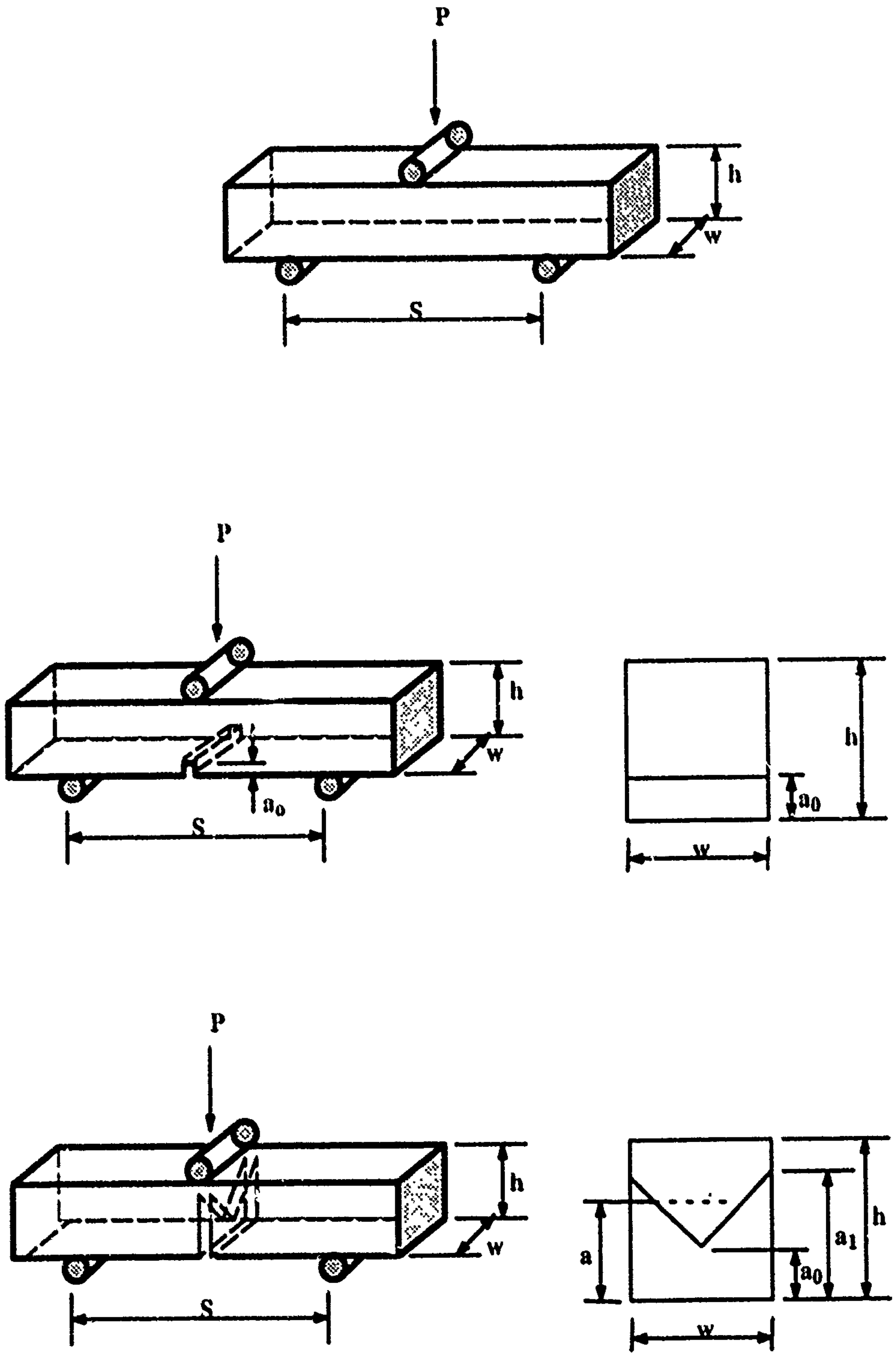

$\alpha_0 = a_0/h$

$\alpha_1 = a_1/h$

$\alpha = a/h$

$\theta = 60^0$

Figure 8

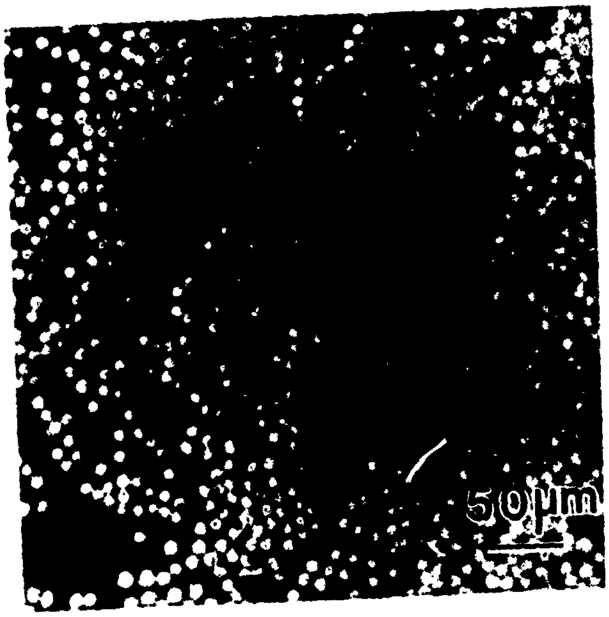

Figure 9

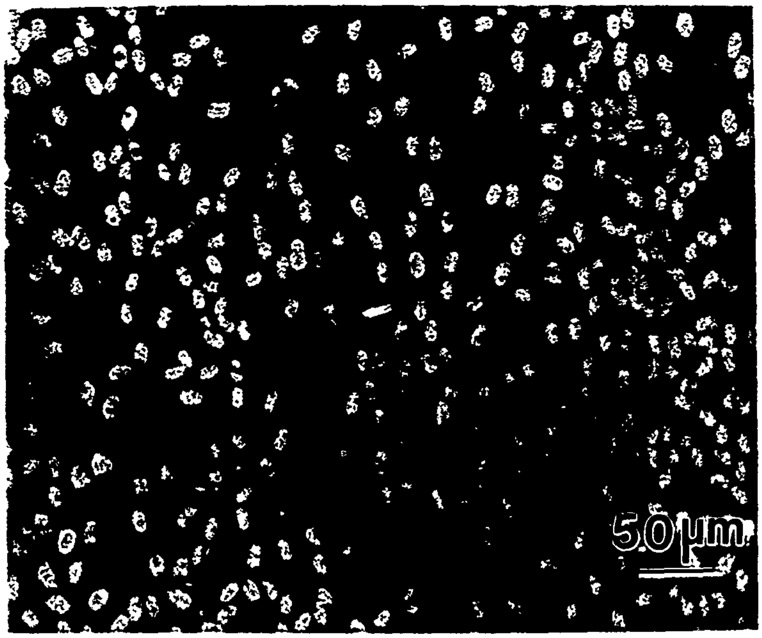

Figure 10

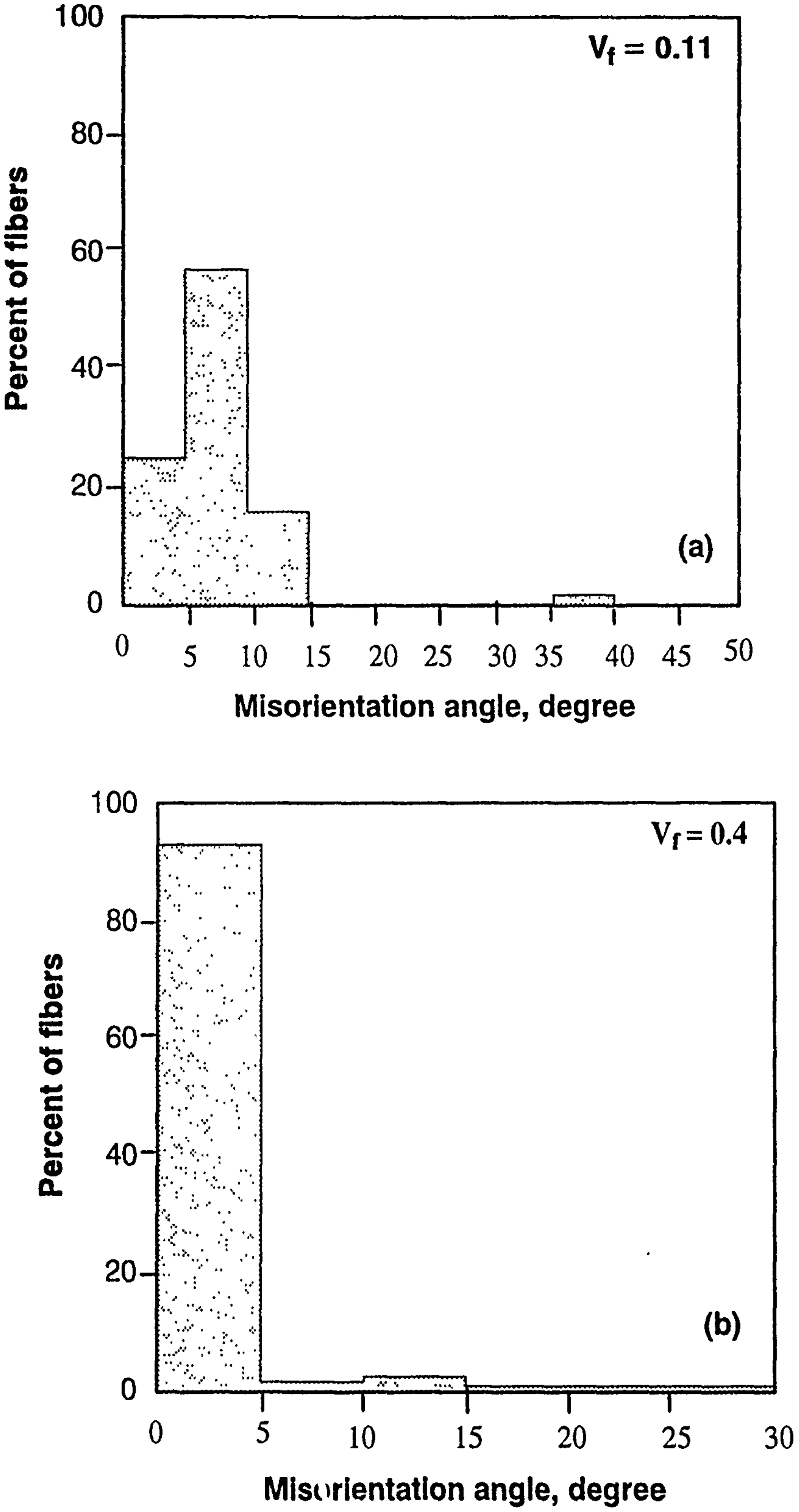
Vf = 0.11
(a)
Percent of fibers
100
80
60
40
20
0
0
5
10
15
20
25
30
35
40
45
50
Misorientation angle, degree
Vf = 0.4
(b)
Percent of fibers
100
80
60
40
20
0
0
5
10
15
20
25
30
Misorientation angle, degree

Figure 11

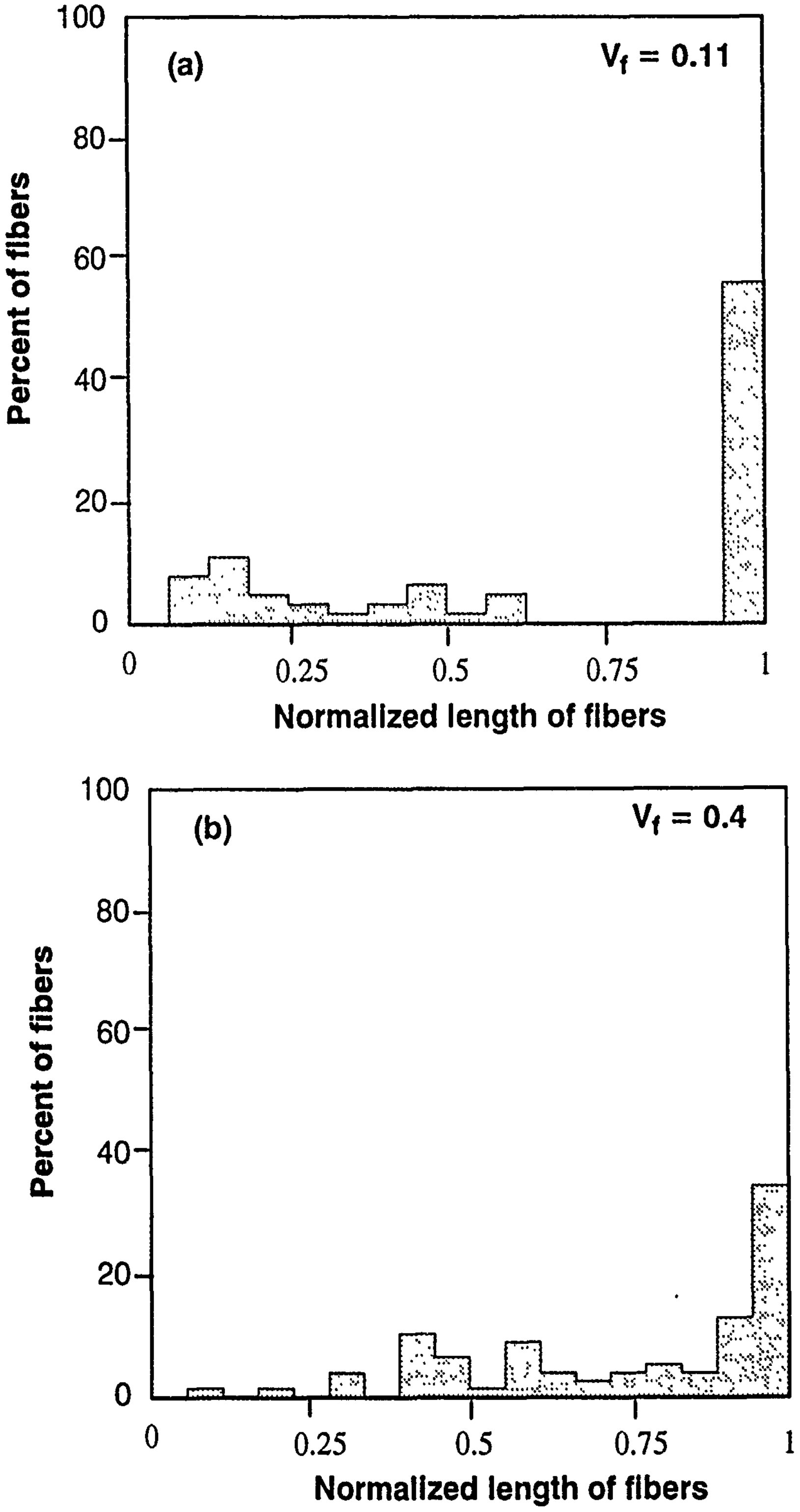
(a)
Vf = 0.11
100
80
60
40
20
0
Percent of fibers
0
0.25
0.5
0.75
1
Normalized length of fibers
(b)
Vf = 0.4
100
80
60
40
20
0
Percent of fibers
0
0.25
0.5
0.75
1
Normalized length of fibers

Figure 12

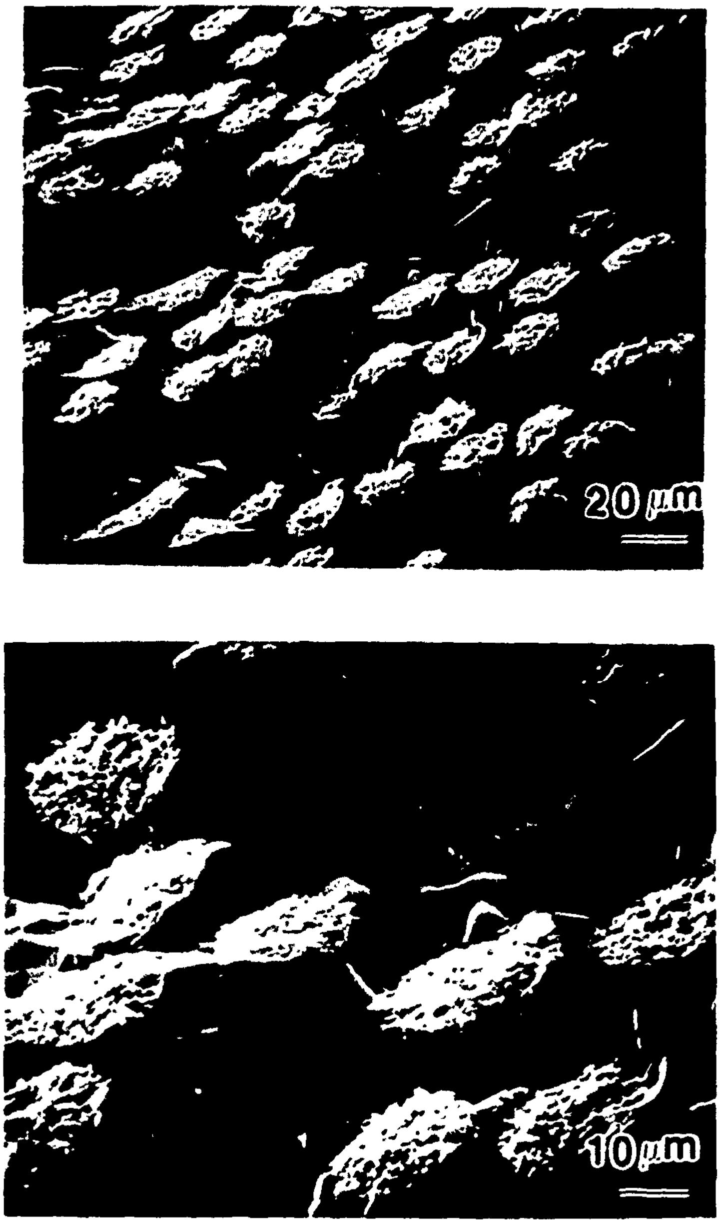

Figure 13 (a)

Figure 13 (b)

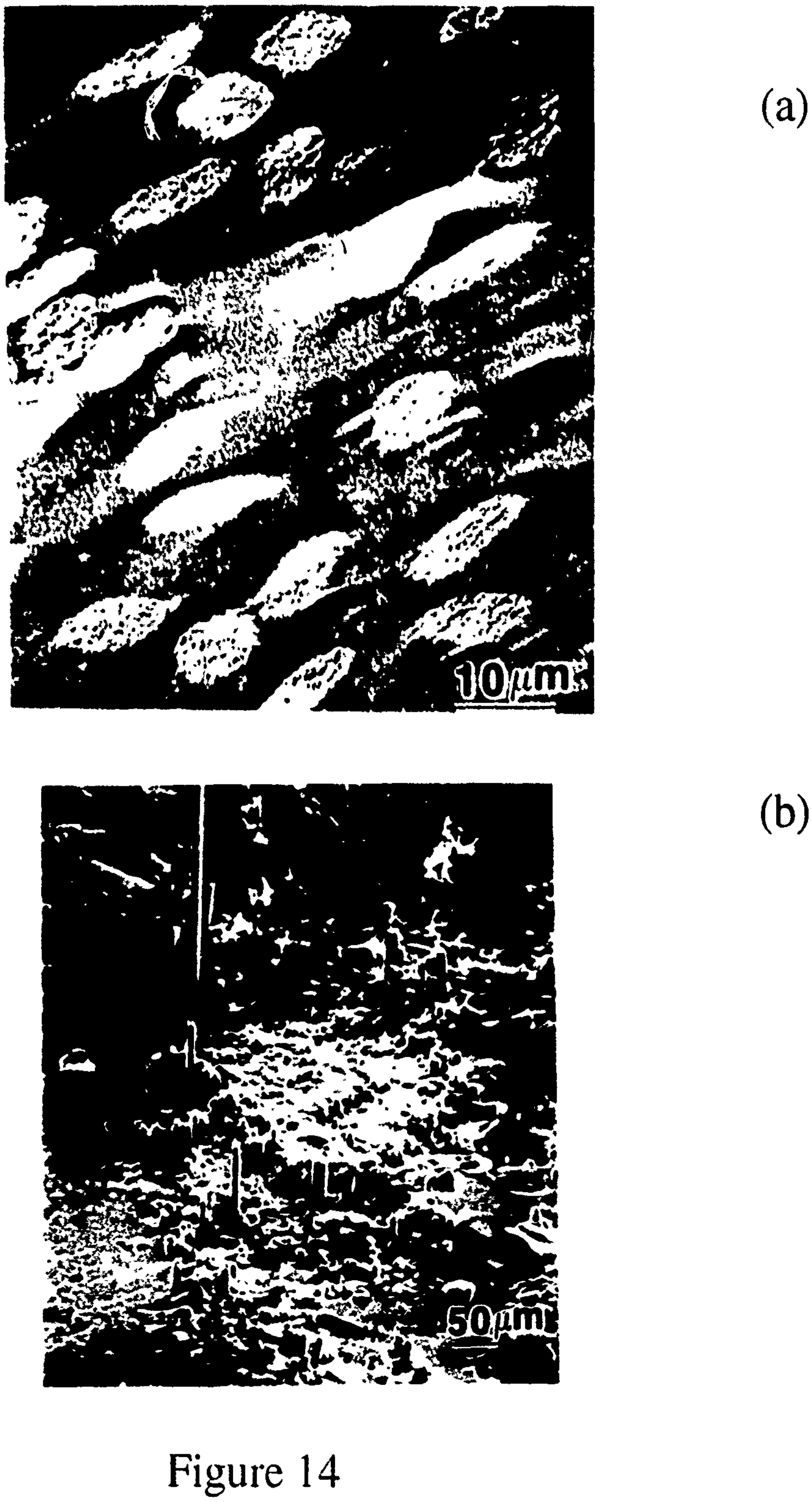

Figure 14

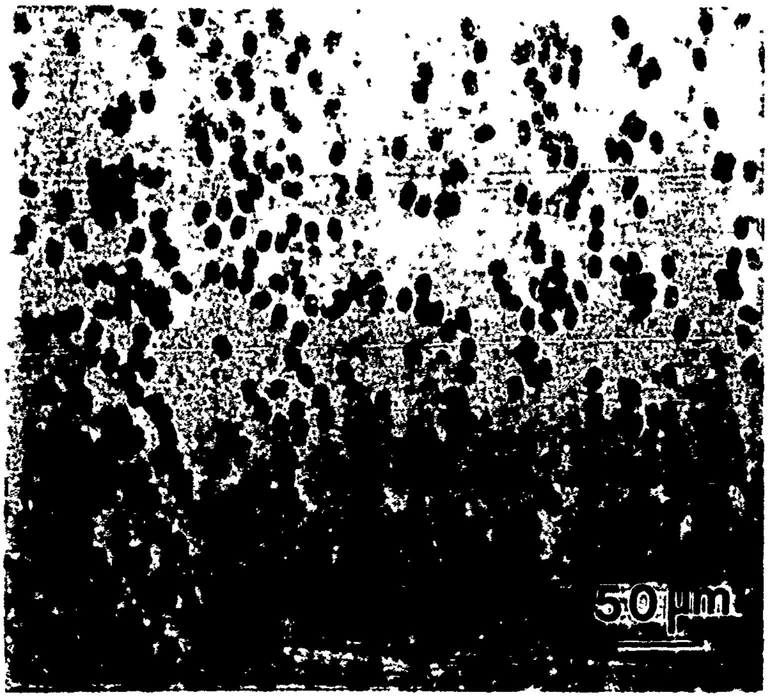

Figure 15

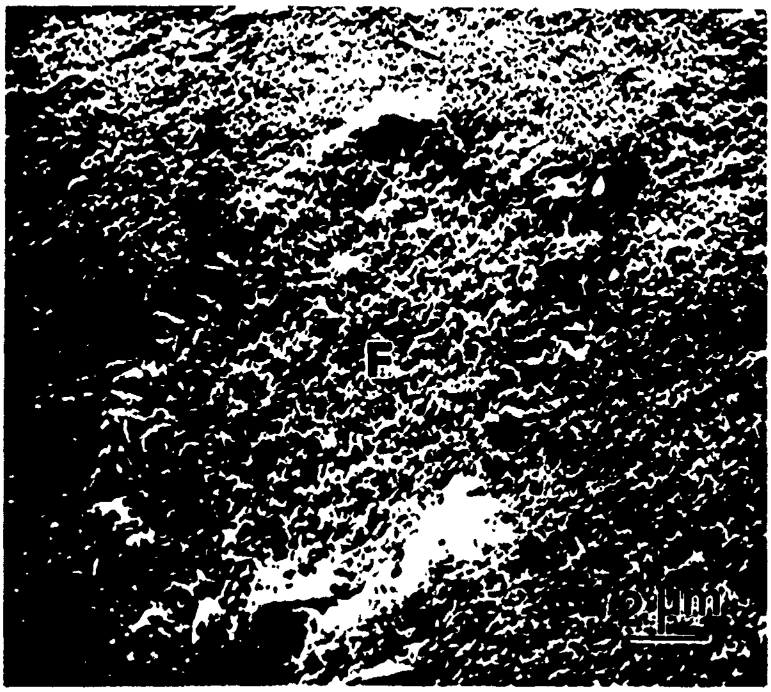

Figure 16

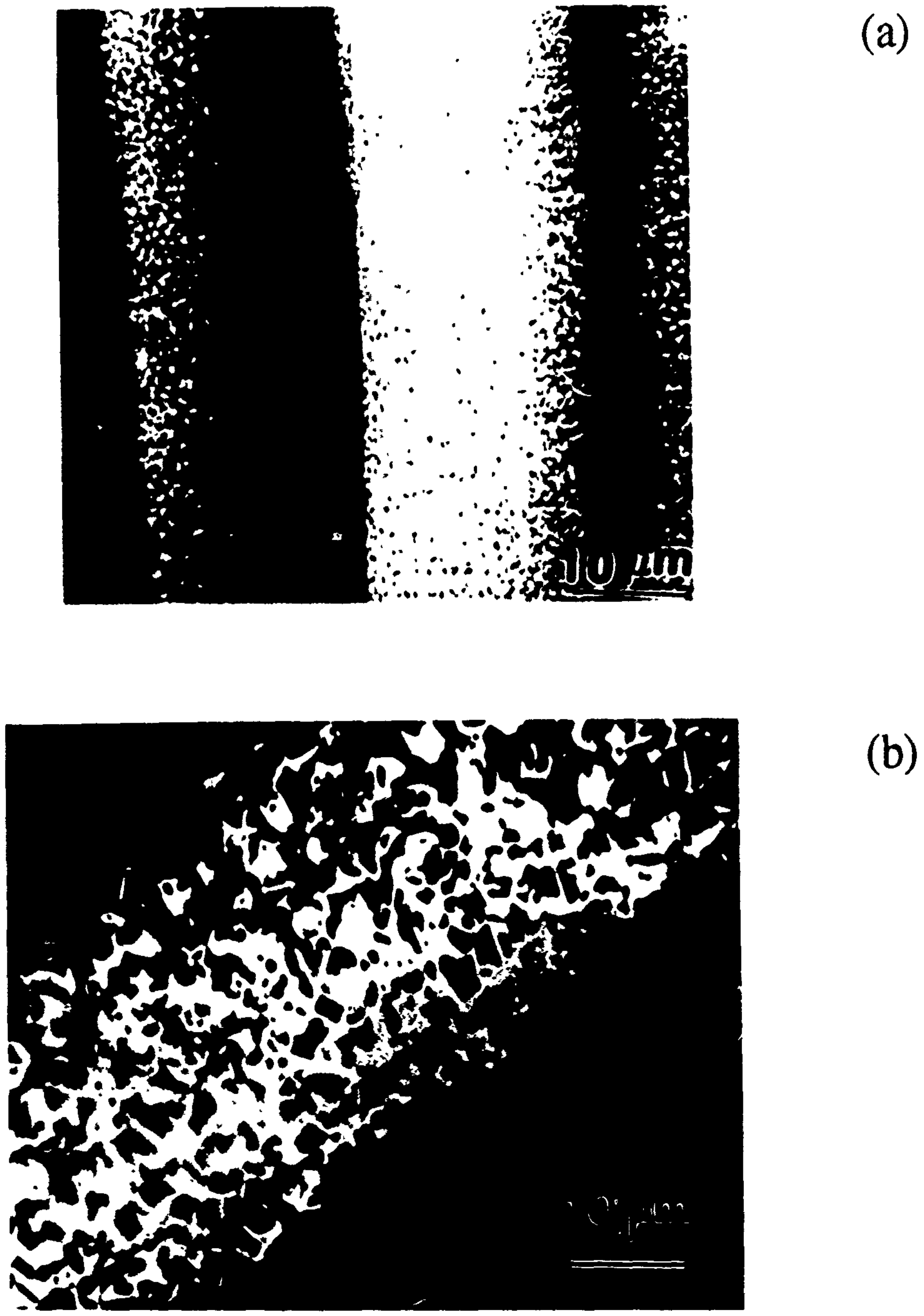

Figure 17

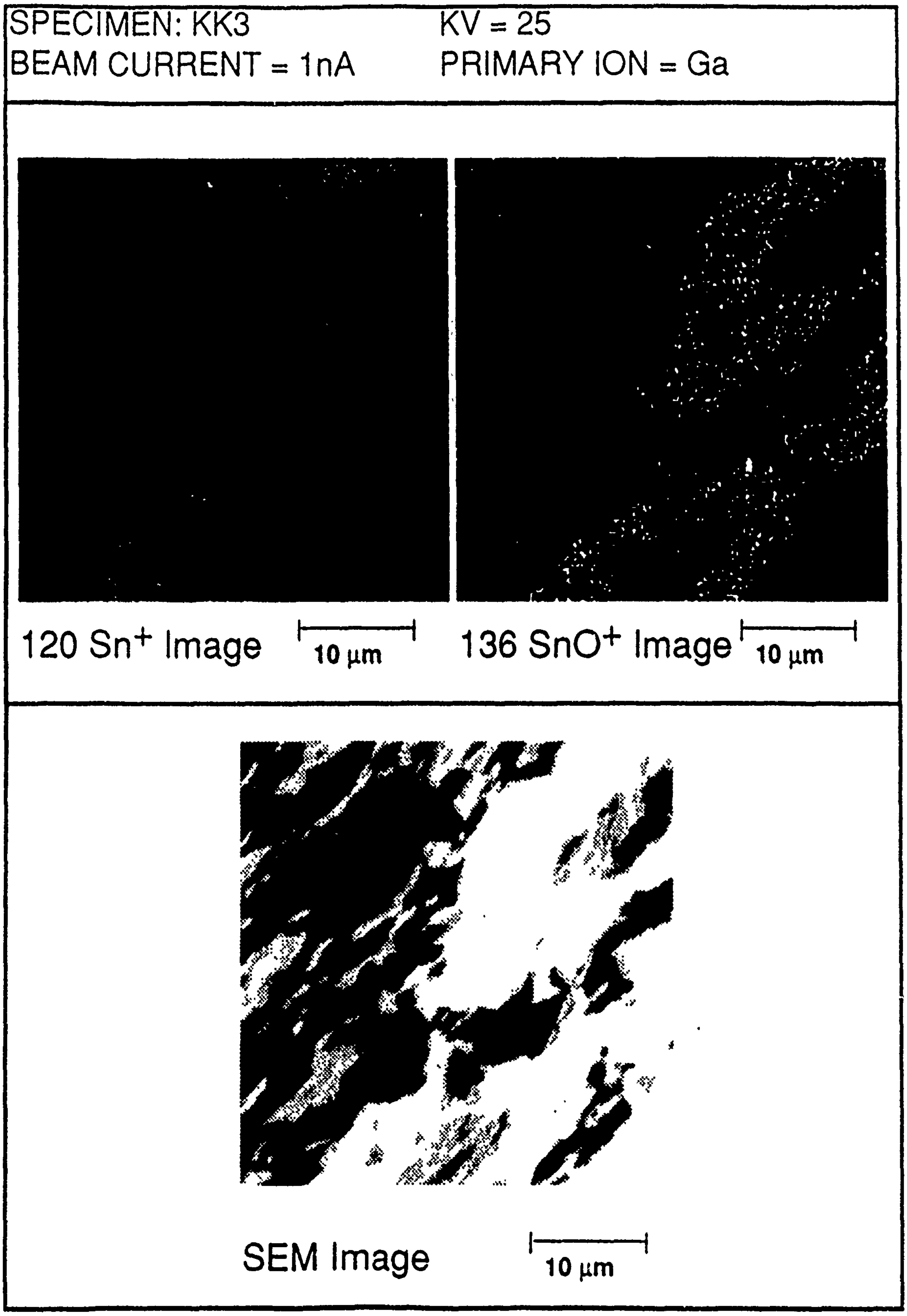
SPECIMEN: KK3
KV = 25
BEAM CURRENT = 1nA
PRIMARY ION = Ga
120 Sn+ Image
10 µm
136 SnO+ Image
10 µm
SEM Image
10 µm

Figure 18

SPECIMEN: KK3 KV = 25
BEAM CURRENT = 1 nA PRIMARY ION = Ga

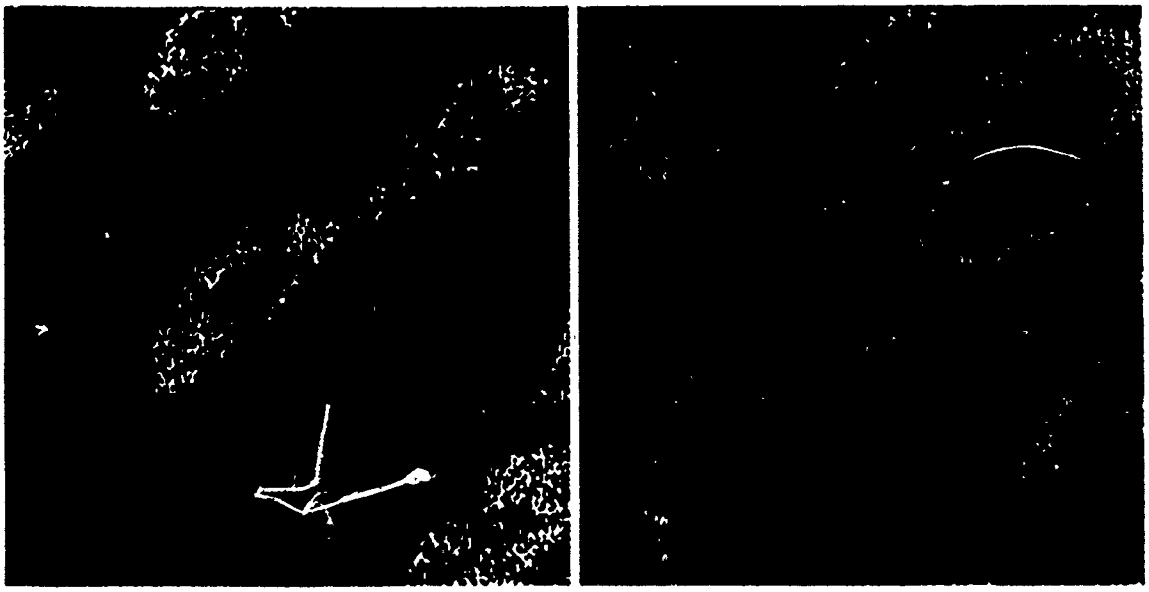
90 Zr^{+} Image

120 Sn^{+} Image

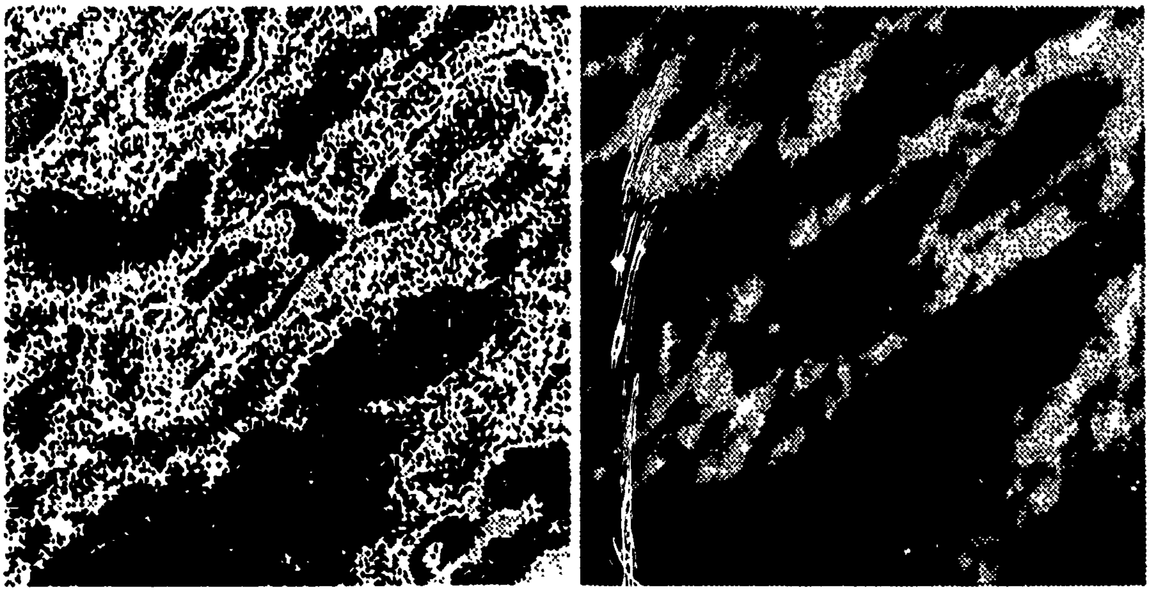
27 Al^{+} Image

SEM Image

Figure 19

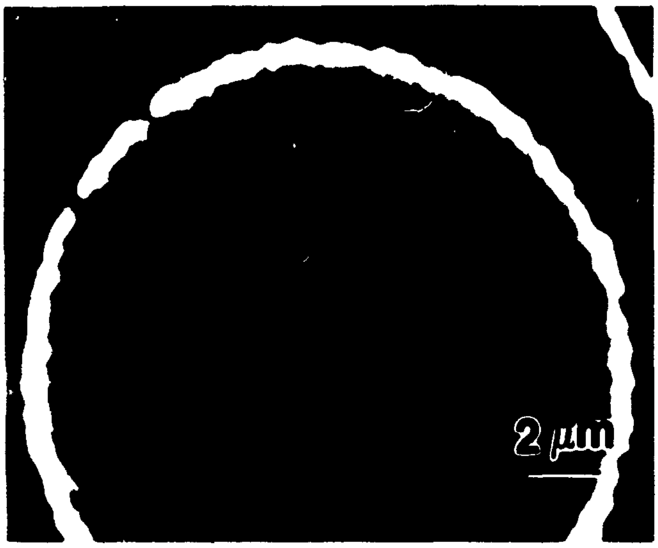

Figure 20

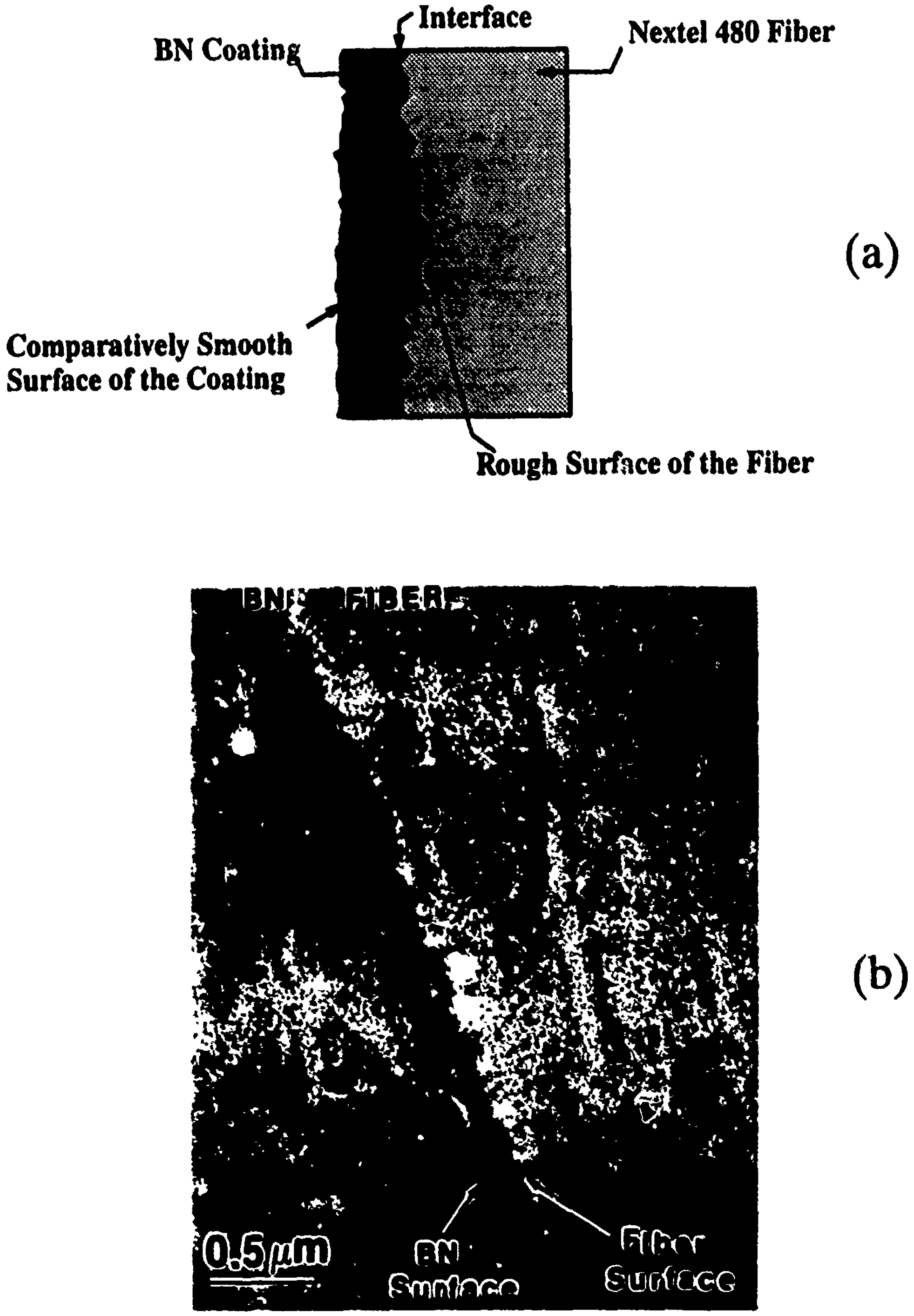
Interface
BN Coating
Nextel 480 Fiber
(a)
Comparatively Smooth Surface of the Coating
Rough Surface of the Fiber
BN
FIBER
(b)
0.5 µm
BN Surface
Fiber Surface

Figure 21

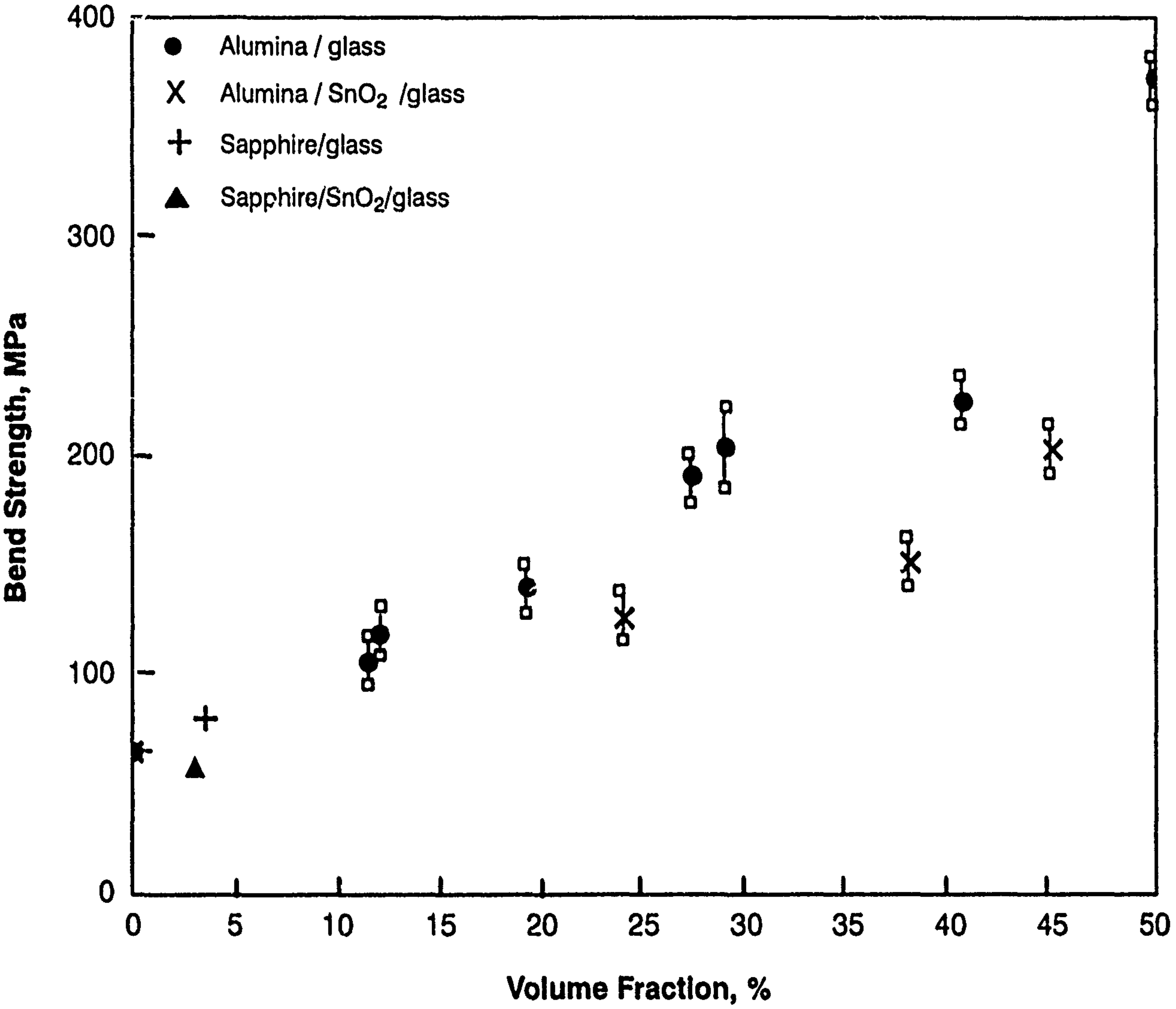
400
300
200
100
0
Bend Strength, MPa
0
5
10
15
20
25
30
35
40
45
50
Volume Fraction, %
● Alumina / glass
X Alumina / SnO_2 /glass
+ Sapphire/glass
▲ Sapphire/SnO_2/glass

Figure 22

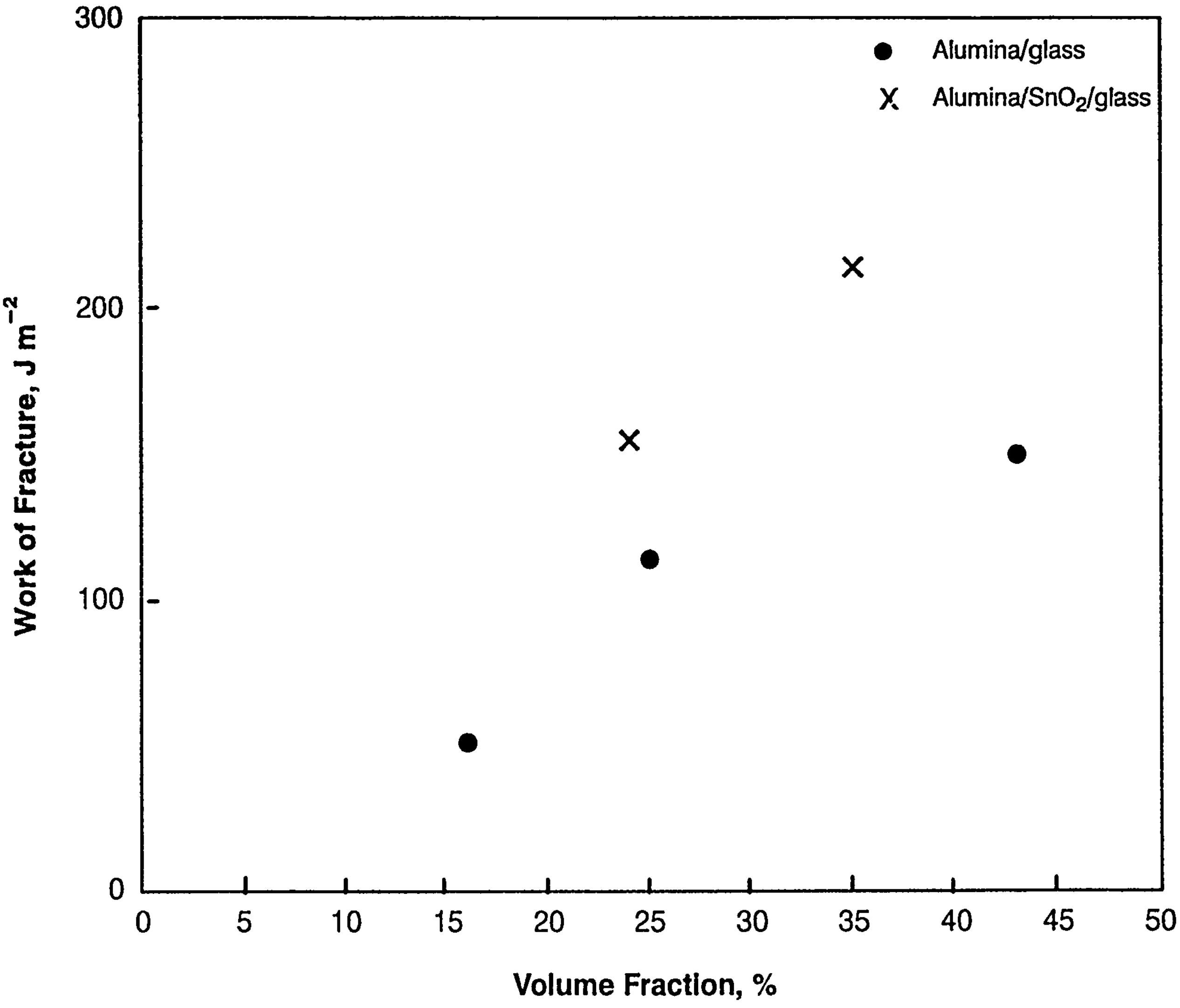
Work of Fracture, J m^{-2}
300
200
100
0
0
5
10
15
20
25
30
35
40
45
50
Volume Fraction, %
● Alumina/glass
X Alumina/SnO$_2$/glass

Figure 23

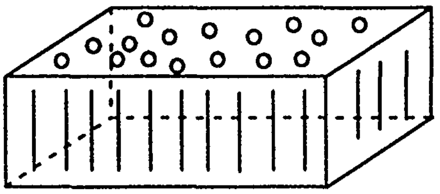

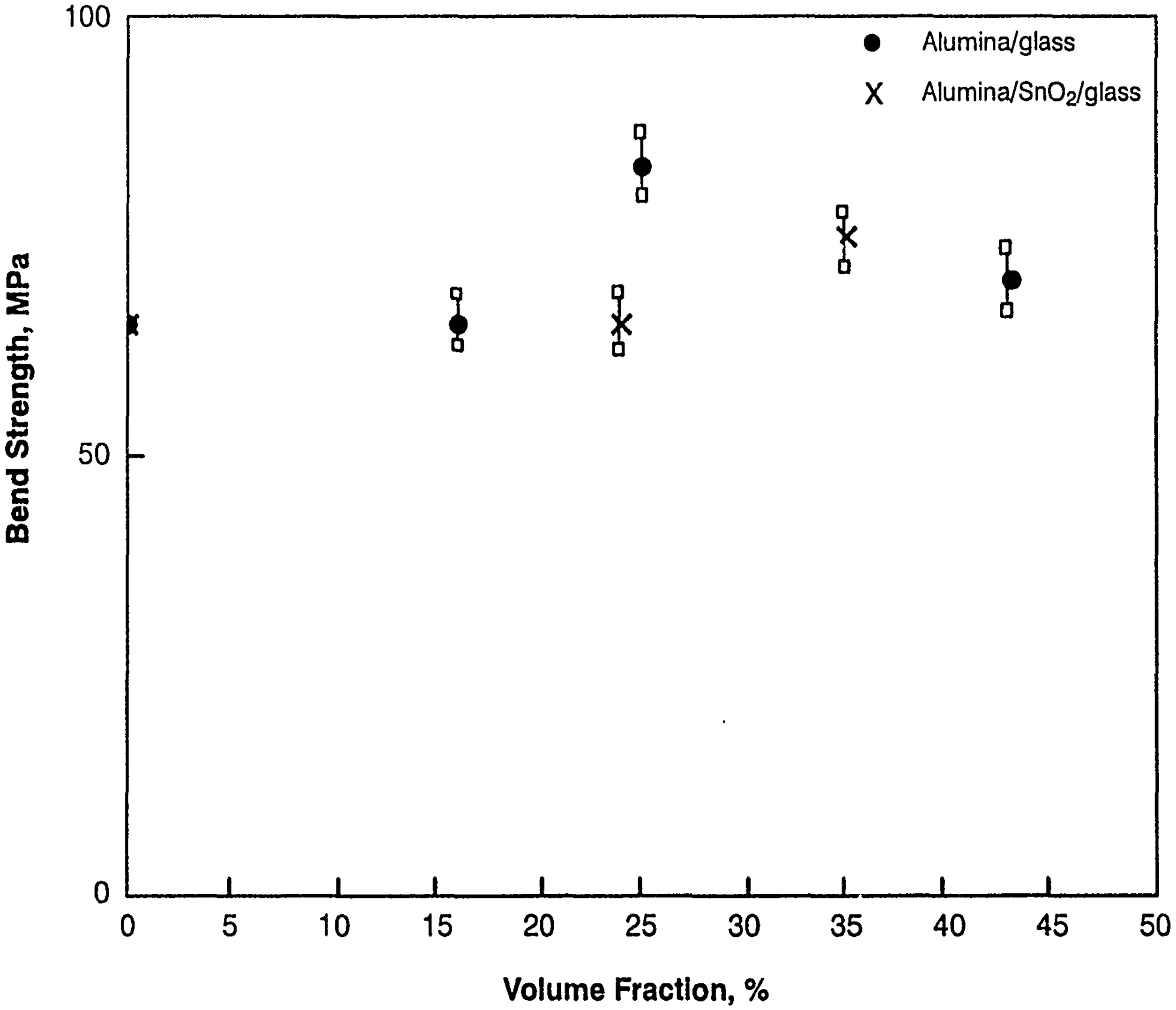
100
50
0
Bend Strength, MPa
0
5
10
15
20
25
30
35
40
45
50
Volume Fraction, %
● Alumina/glass
X Alumina/SnO2/glass

Figure 24

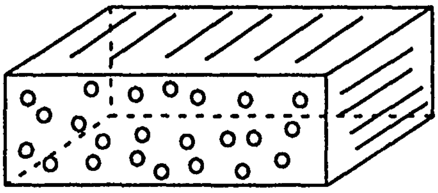

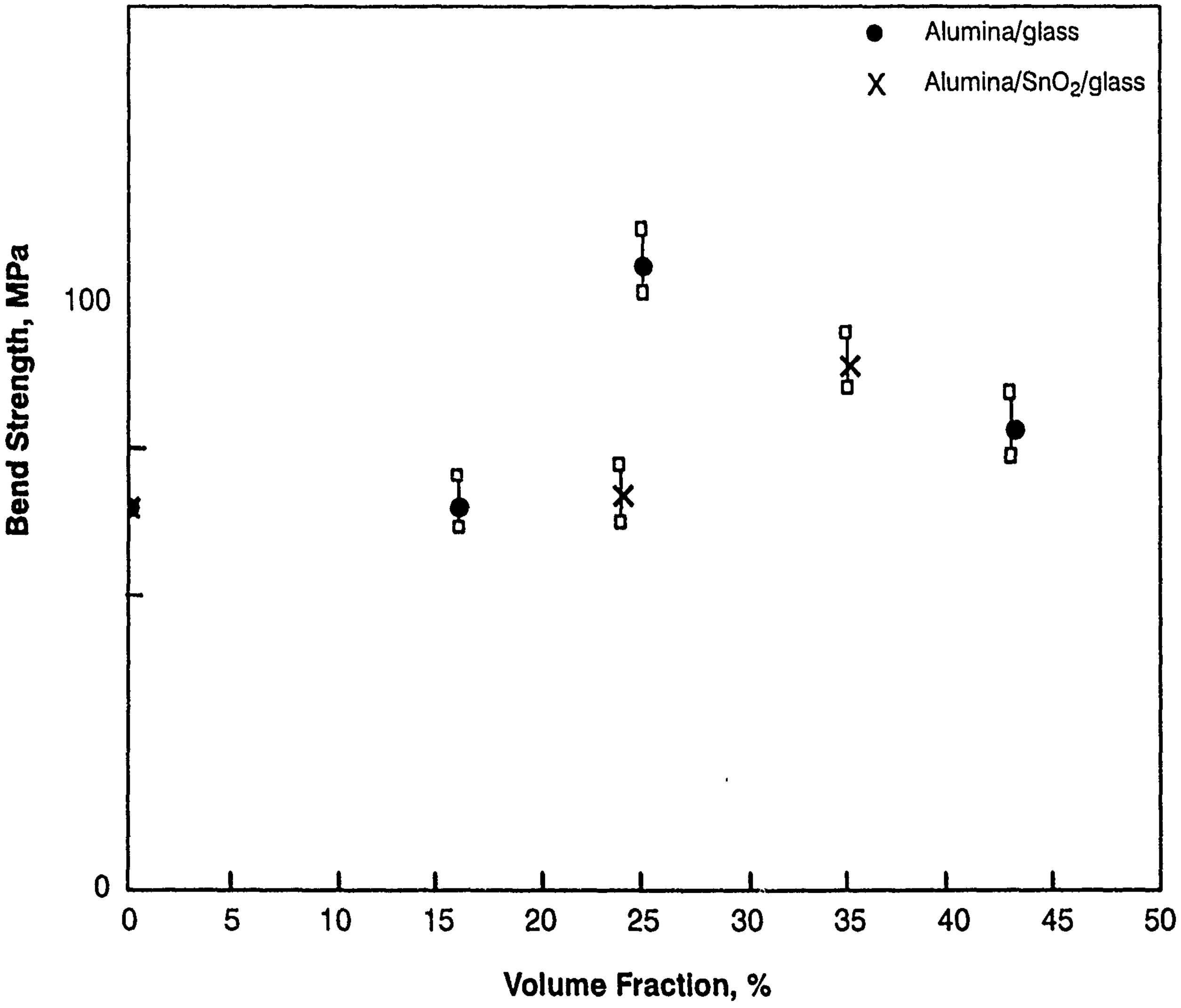
Alumina/glass
Alumina/SnO_2/glass
Bend Strength, MPa
100
0
0
5
10
15
20
25
30
35
40
45
50
Volume Fraction, %

Figure 25

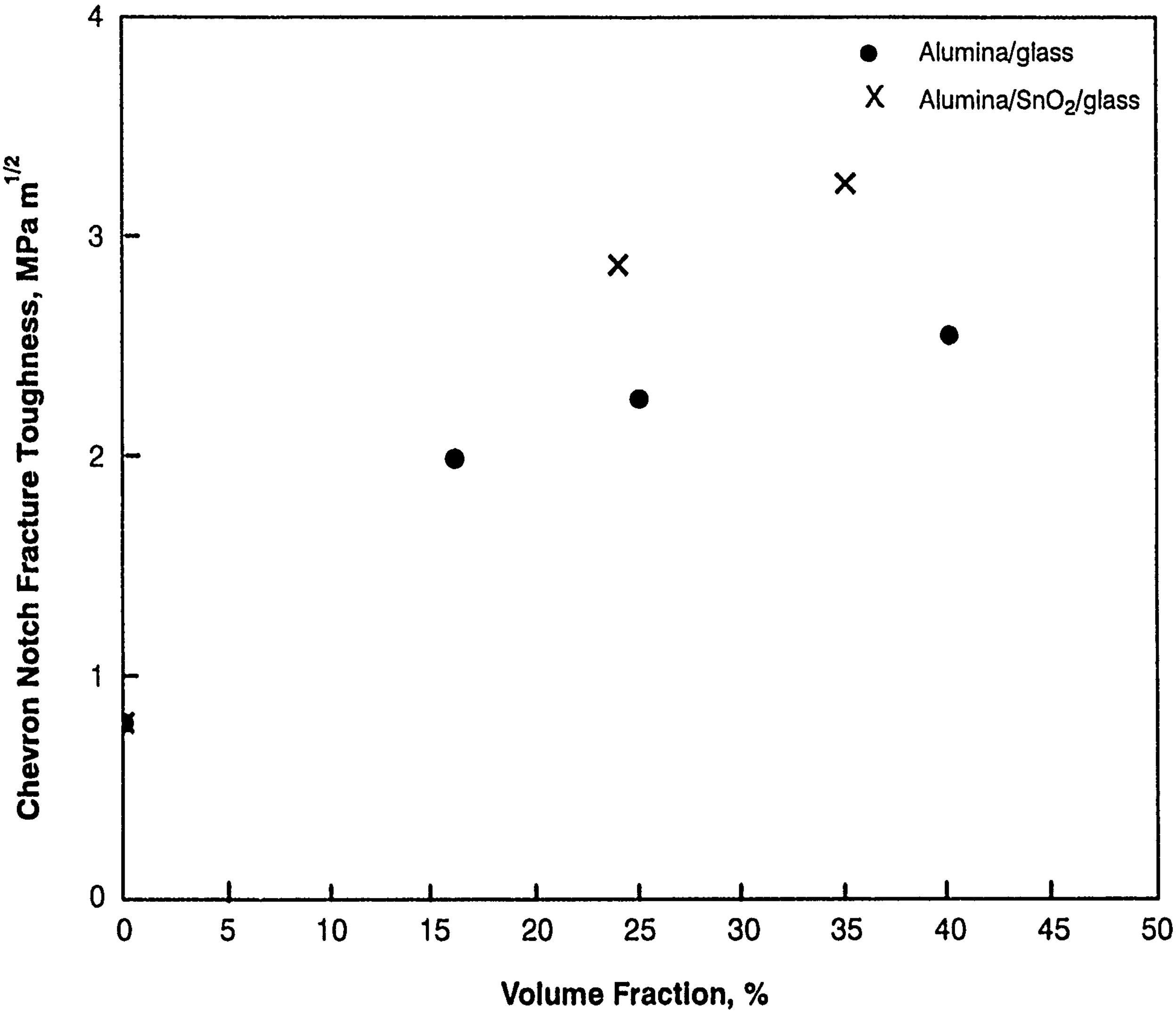

Alumina/glass
Alumina/SnO2/glass
Chevron Notch Fracture Toughness, MPa m^1/2
Volume Fraction, %
0
1
2
3
4
0
5
10
15
20
25
30
35
40
45
50

Figure 26

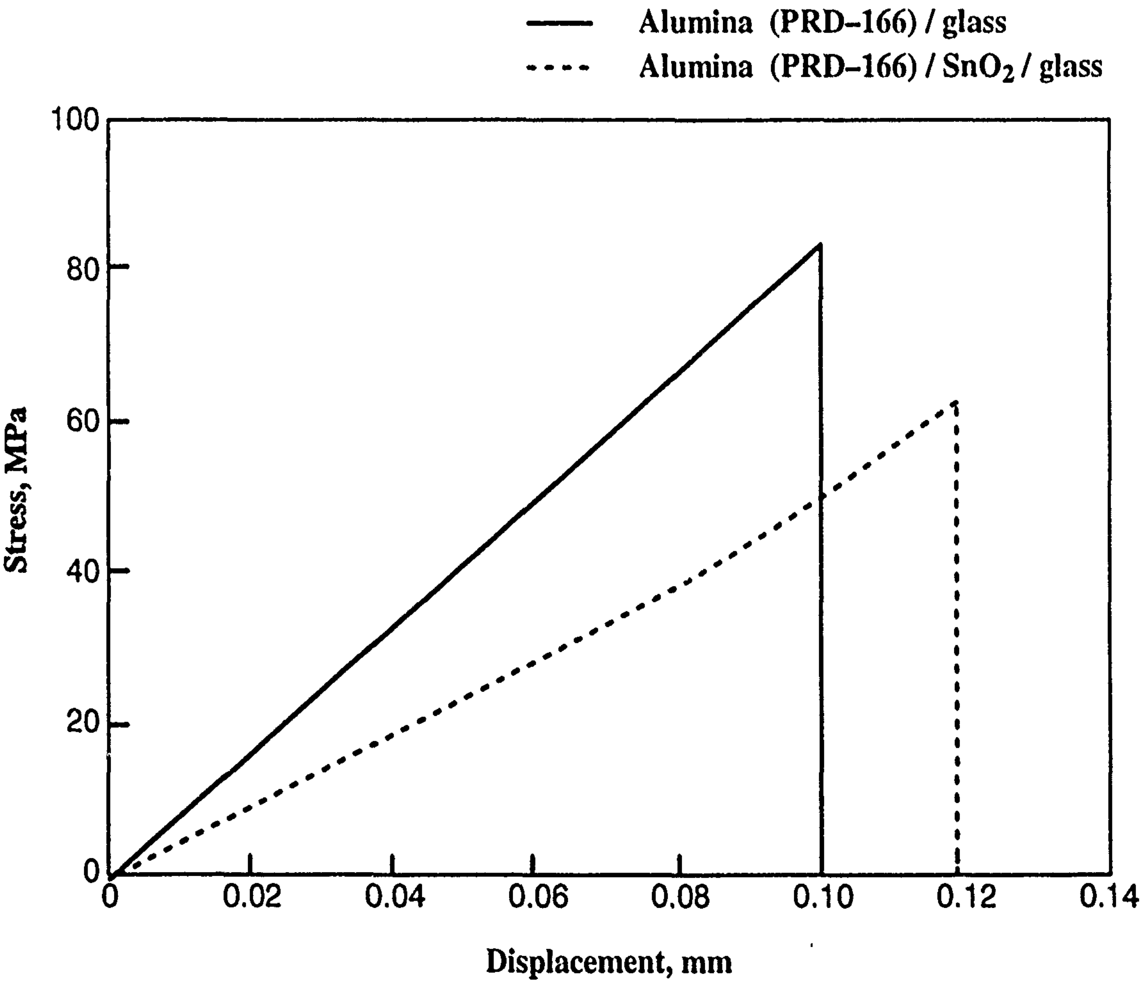
Alumina (PRD-166) / glass
Alumina (PRD-166) / SnO_2 / glass
Stress, MPa
Displacement, mm
0
20
40
60
80
100
0
0.02
0.04
0.06
0.08
0.10
0.12
0.14

Figure 27

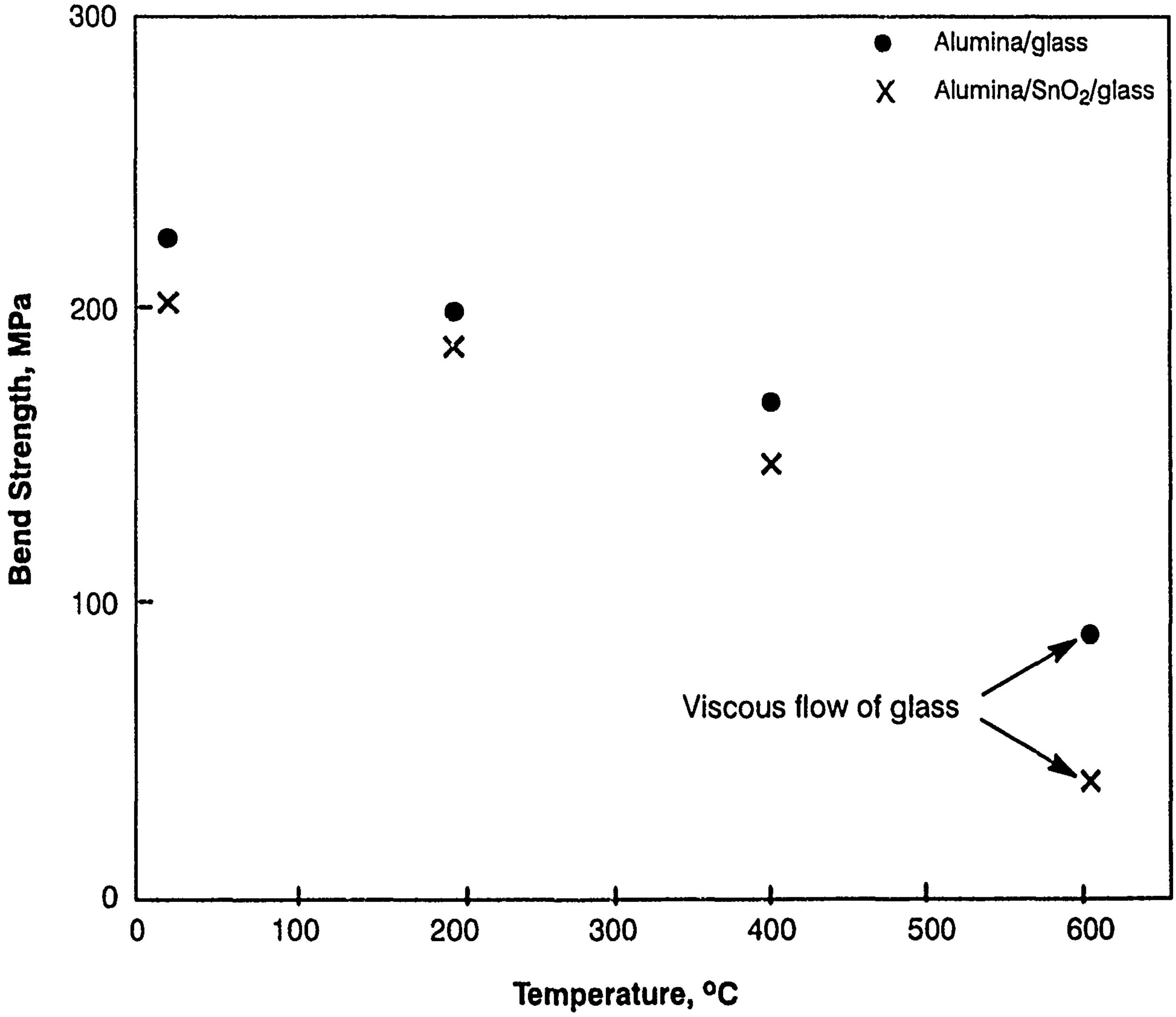
Bend Strength, MPa
300
200
100
0
Temperature, °C
0
100
200
300
400
500
600
● Alumina/glass
X Alumina/SnO_2/glass
Viscous flow of glass

Figure 28

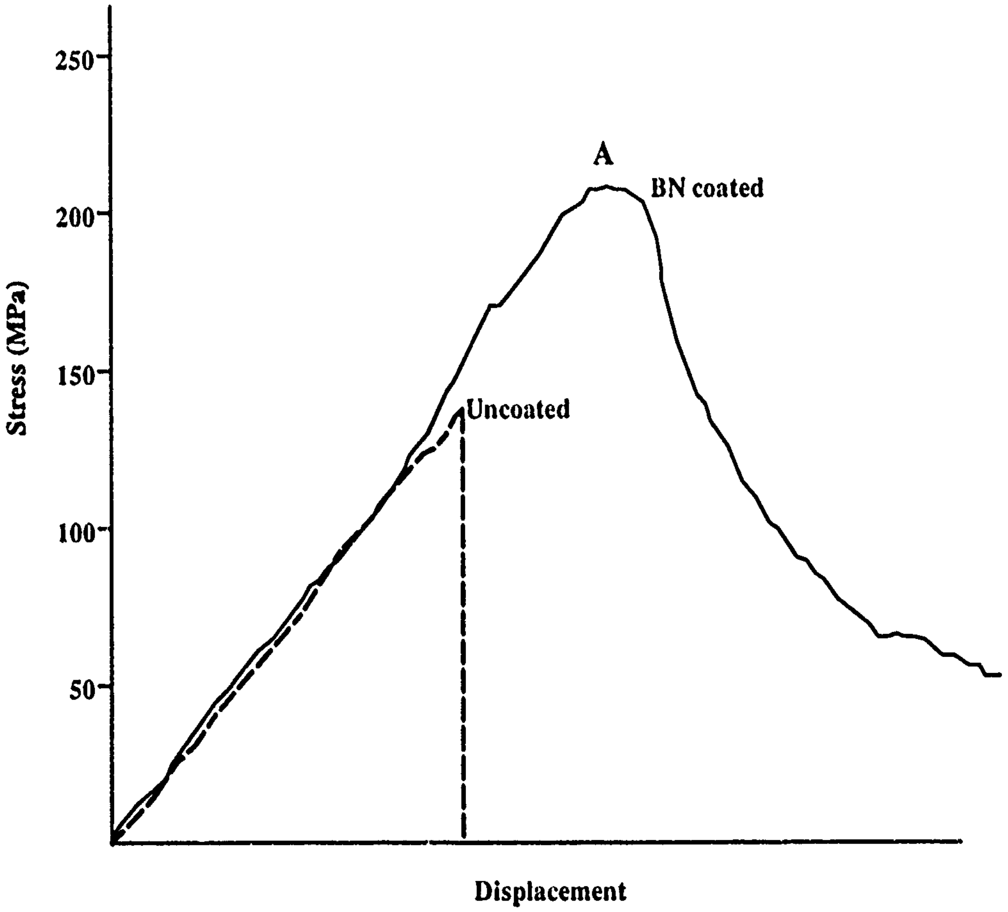
250
200
150
100
50
Stress (MPa)
A
BN coated
Uncoated
Displacement

Figure 29

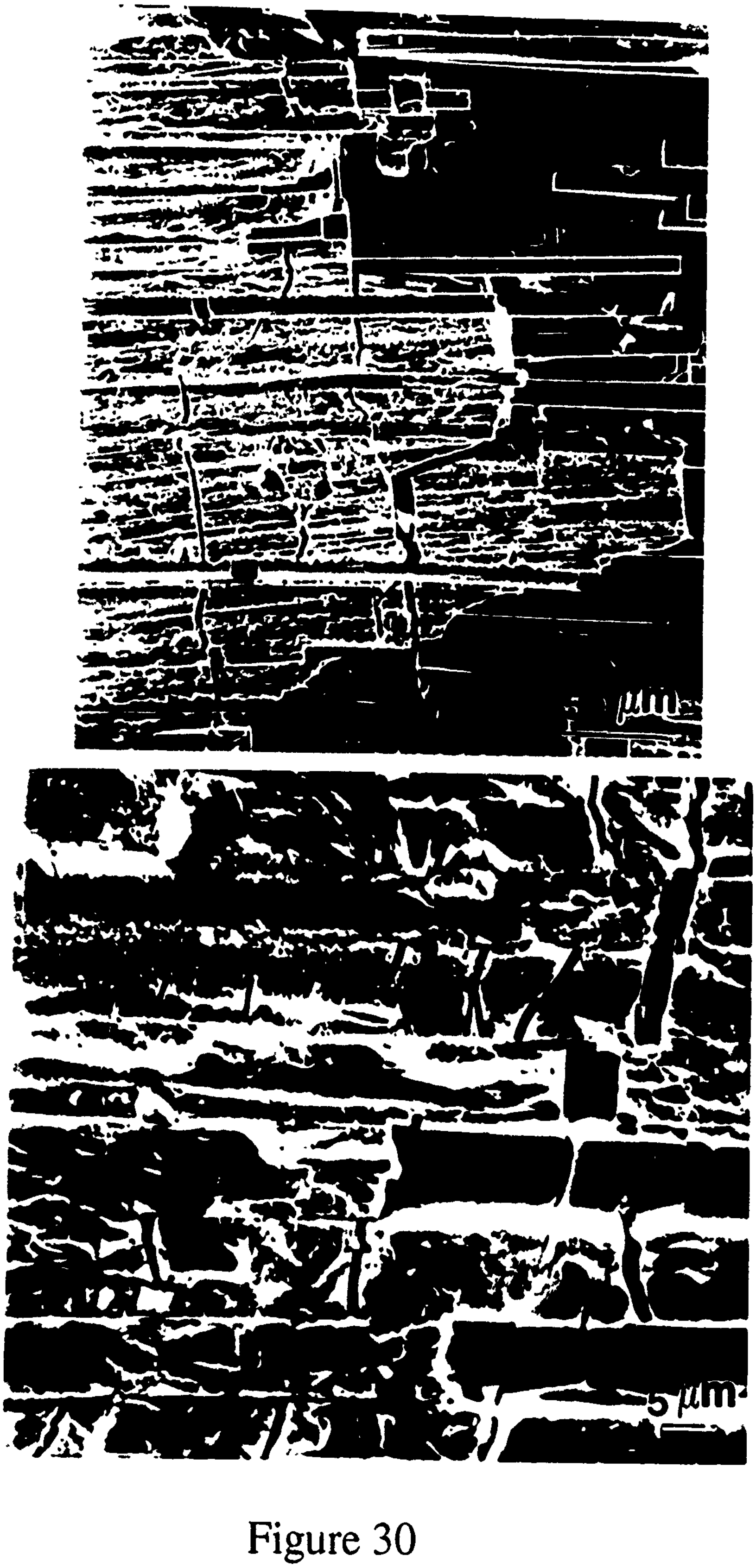

Figure 30

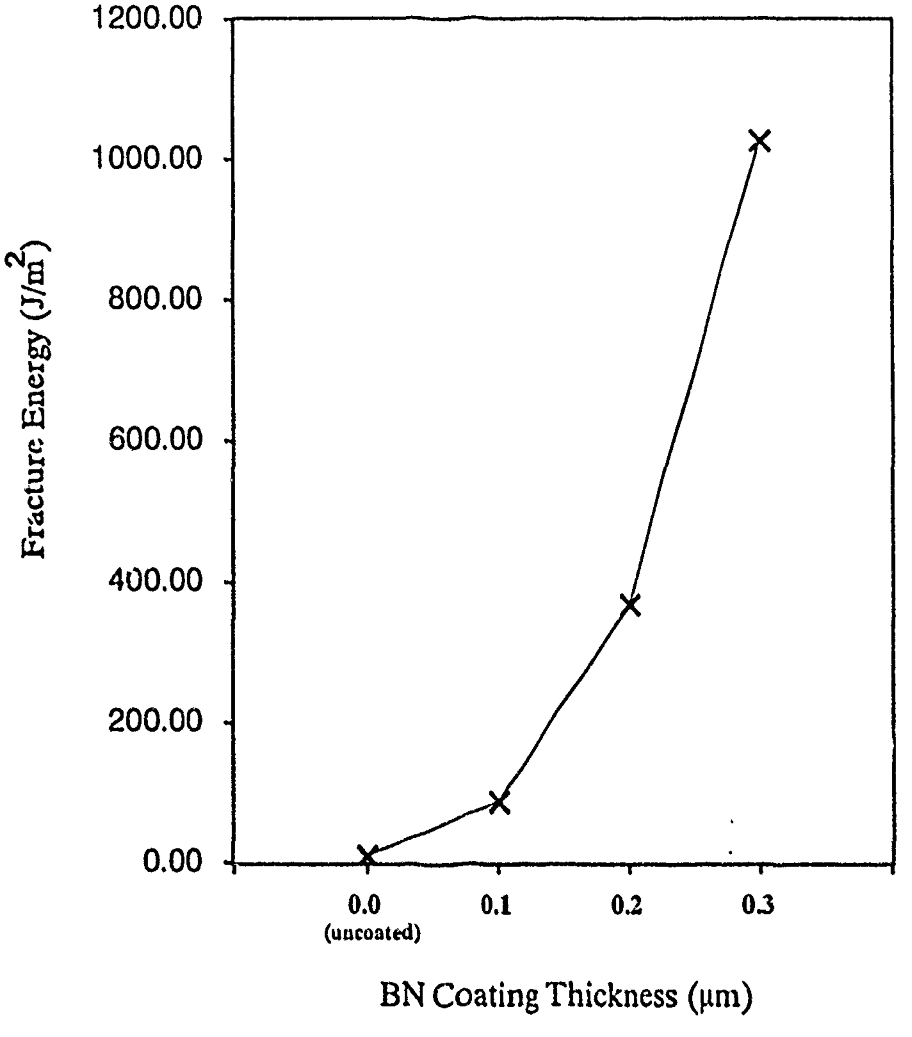
1200.00
1000.00
800.00
600.00
400.00
200.00
0.00
Fracture Energy (J/m^2)
0.0
(uncoated)
0.1
0.2
0.3
BN Coating Thickness (μm)

Figure 31

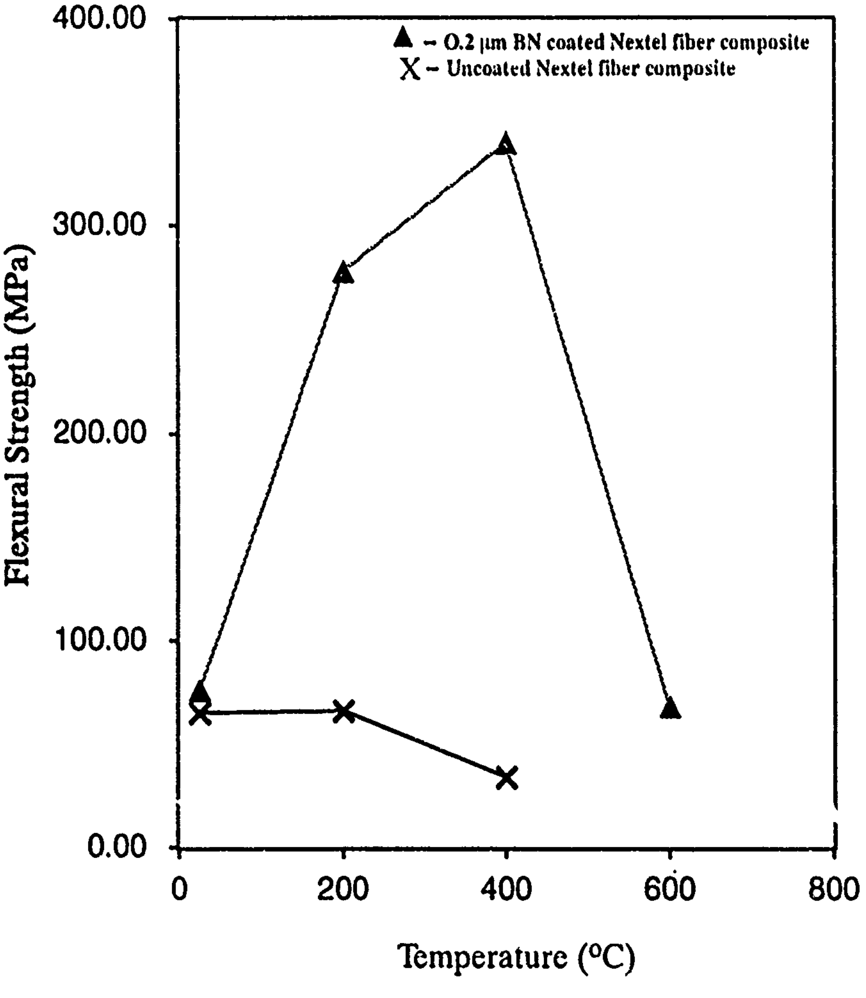
400.00
300.00
200.00
100.00
0.00
Flexural Strength (MPa)
▲ – O.2 μm BN coated Nextel fiber composite
X – Uncoated Nextel fiber composite
0
200
400
600
800
Temperature (°C)

Figure 32

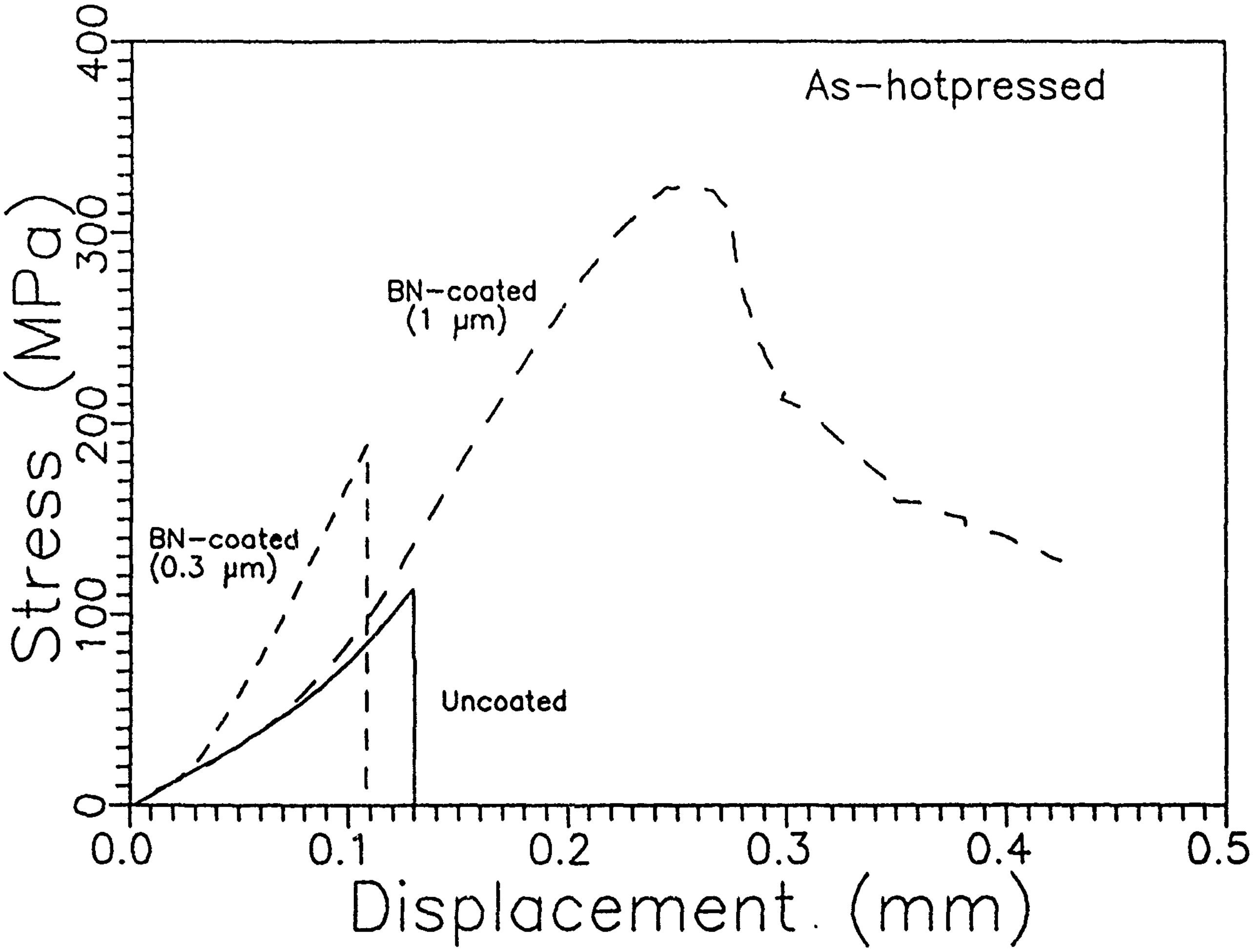
As−hotpressed
BN−coated
(1 μm)
BN−coated
(0.3 μm)
Uncoated
Stress (MPa)
0
100
200
300
400
0.0
0.1
0.2
0.3
0.4
0.5
Displacement (mm)

Figure 33

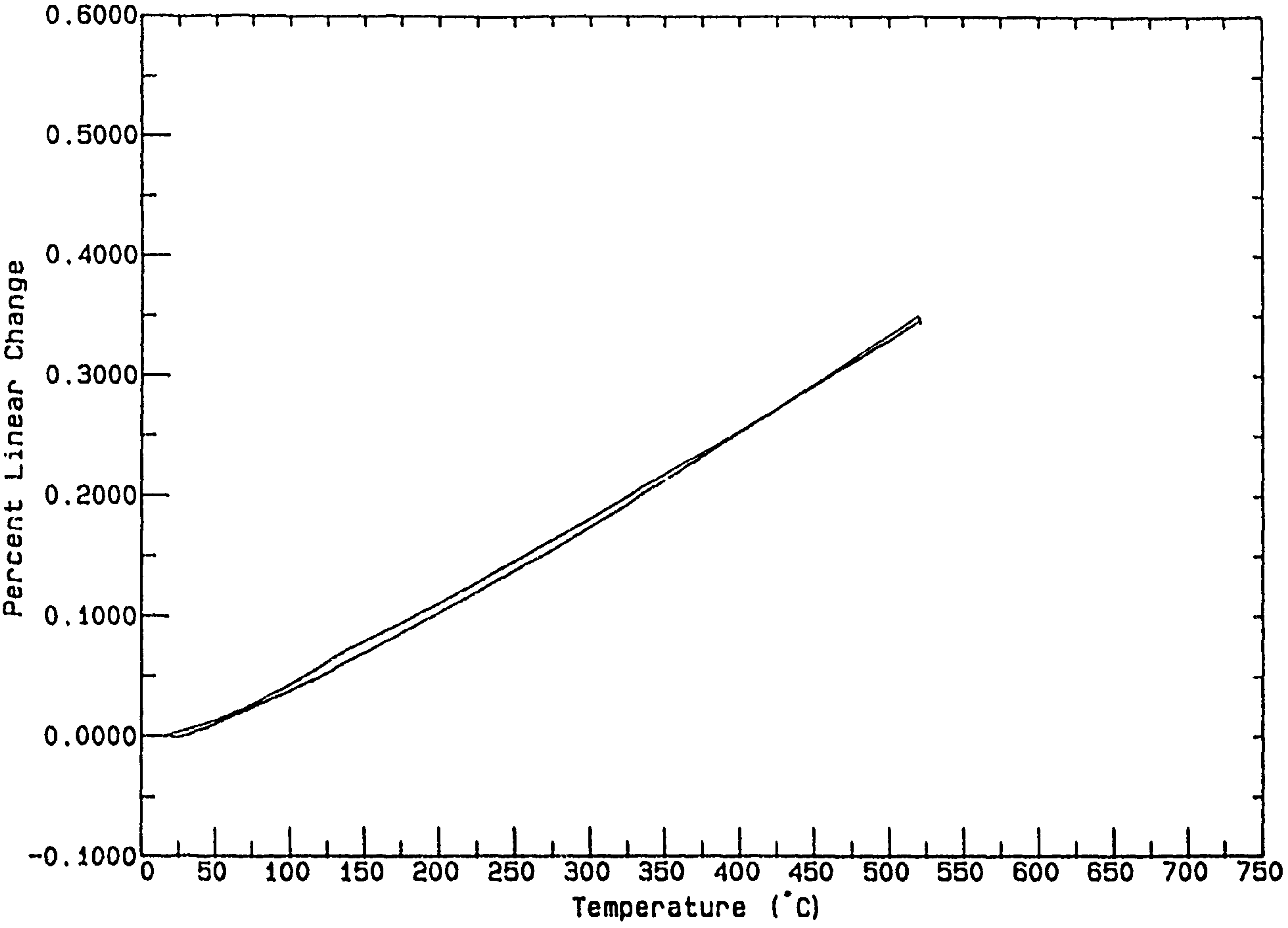

0.6000
0.5000
0.4000
0.3000
0.2000
0.1000
0.0000
-0.1000
Percent Linear Change
0
50
100
150
200
250
300
350
400
450
500
550
600
650
700
750
Temperature (˚C)

Figure 34 (a)

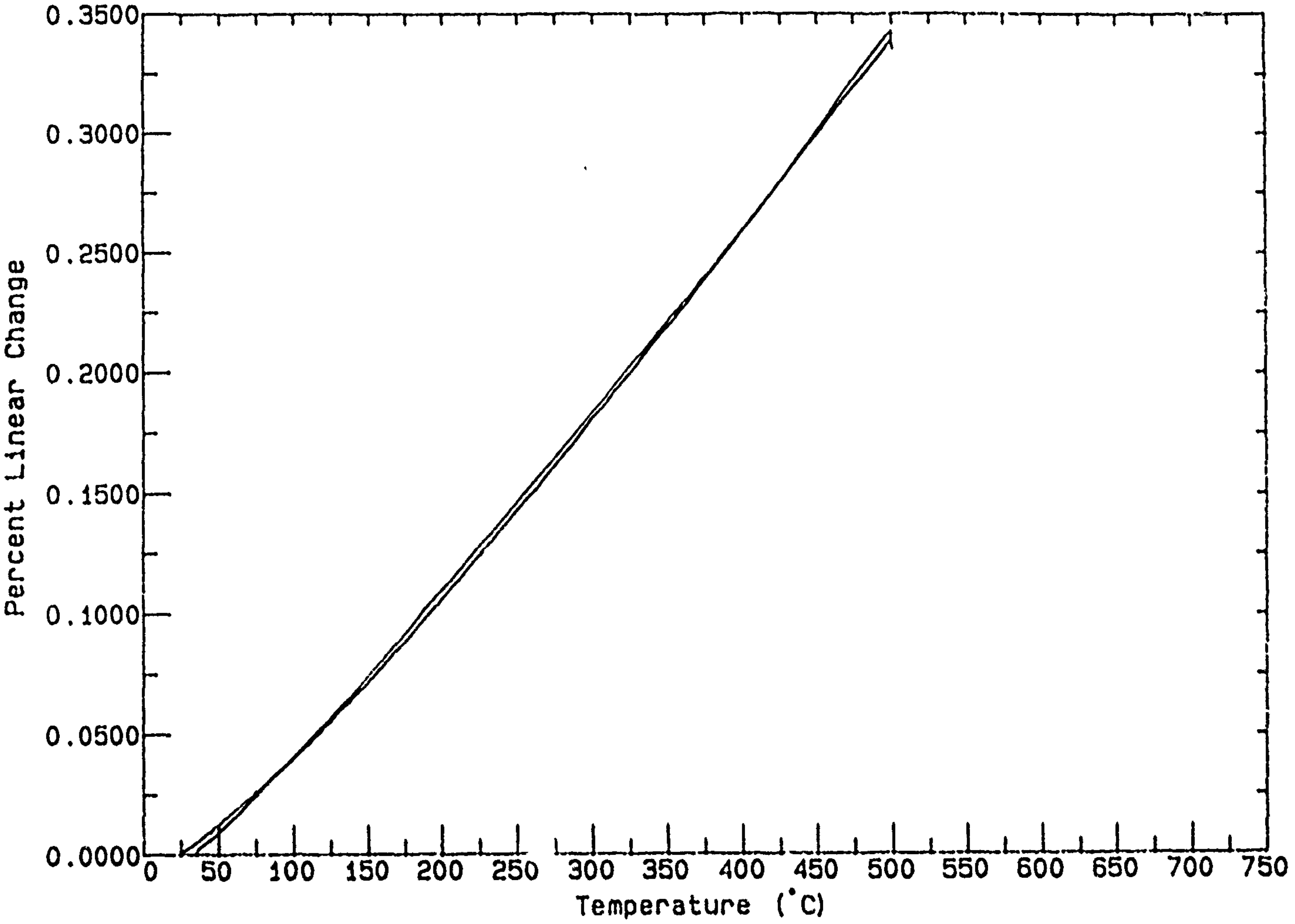
Percent Linear Change
0.3500
0.3000
0.2500
0.2000
0.1500
0.1000
0.0500
0.0000
0
50
100
150
200
250
300
350
400
450
500
550
600
650
700
750
Temperature (°C)

Figure 34 (b)

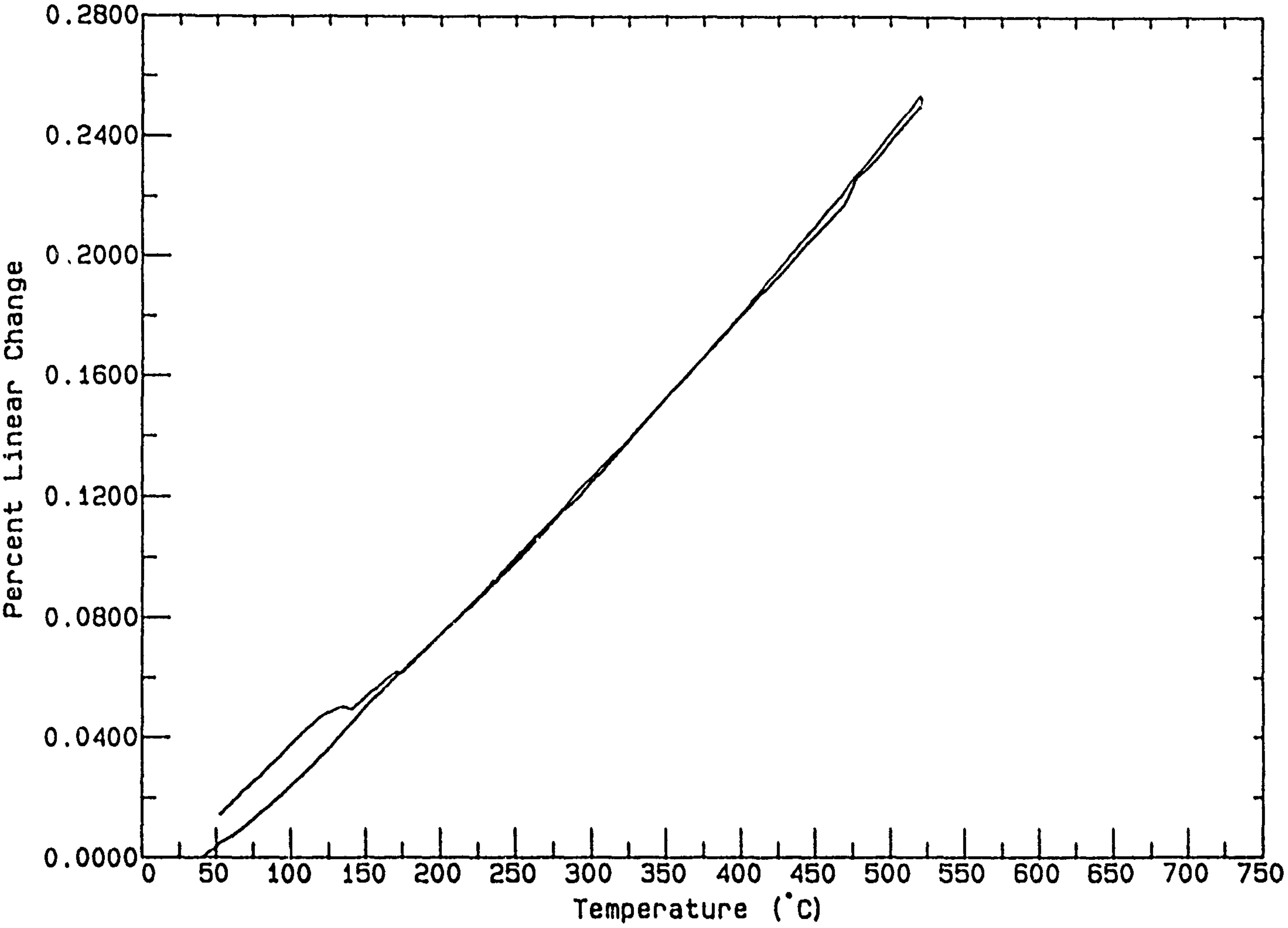
0.2800
0.2400
0.2000
0.1600
0.1200
0.0800
0.0400
0.0000
Percent Linear Change
0
50
100
150
200
250
300
350
400
450
500
550
600
650
700
750
Temperature (°C)

Figure 35 (a)

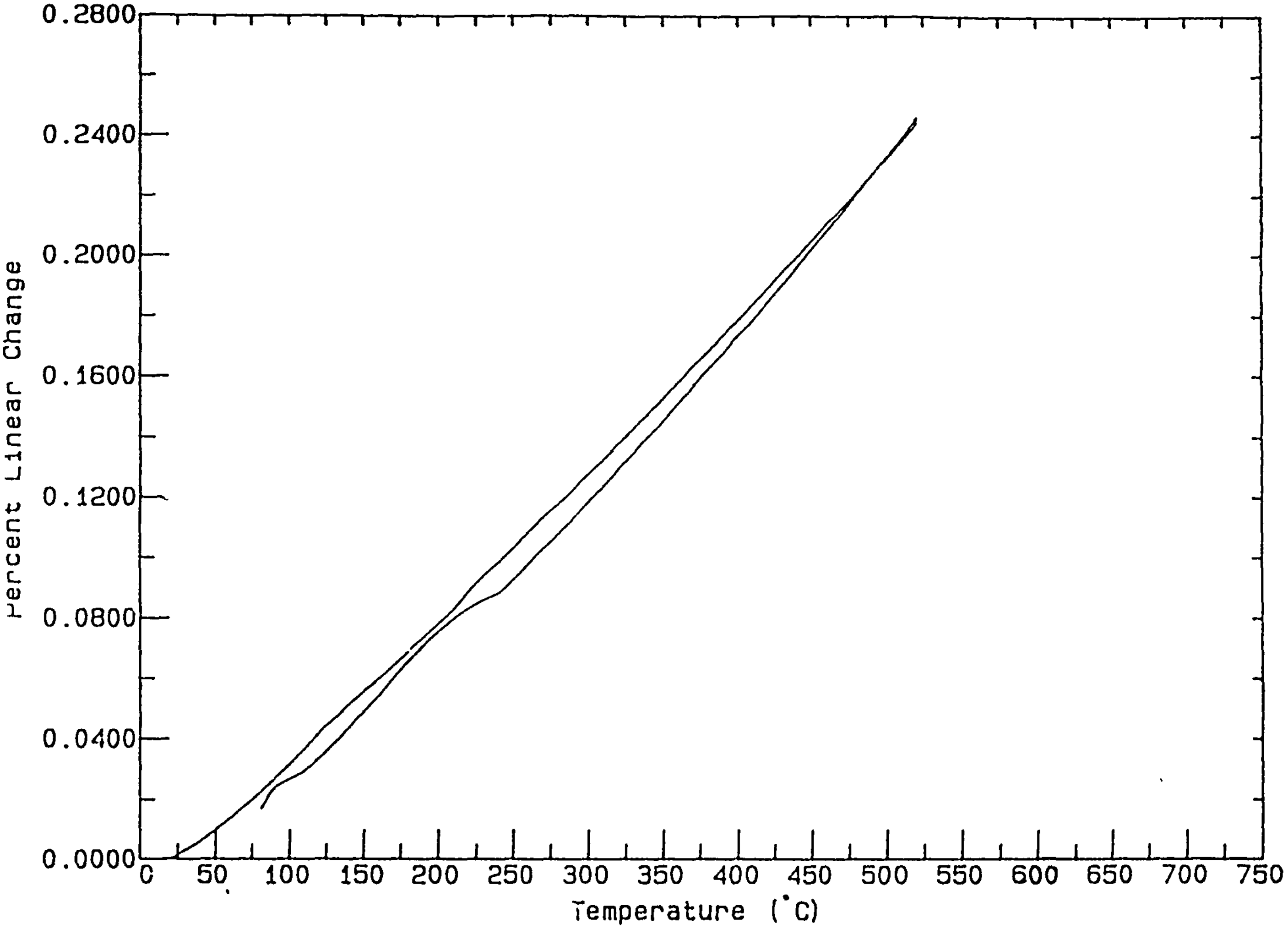
0.2800
0.2400
0.2000
0.1600
0.1200
0.0800
0.0400
0.0000
Percent Linear Change
0
50
100
150
200
250
300
350
400
450
500
550
600
650
700
750
Temperature (°C)

Figure 35 (b)

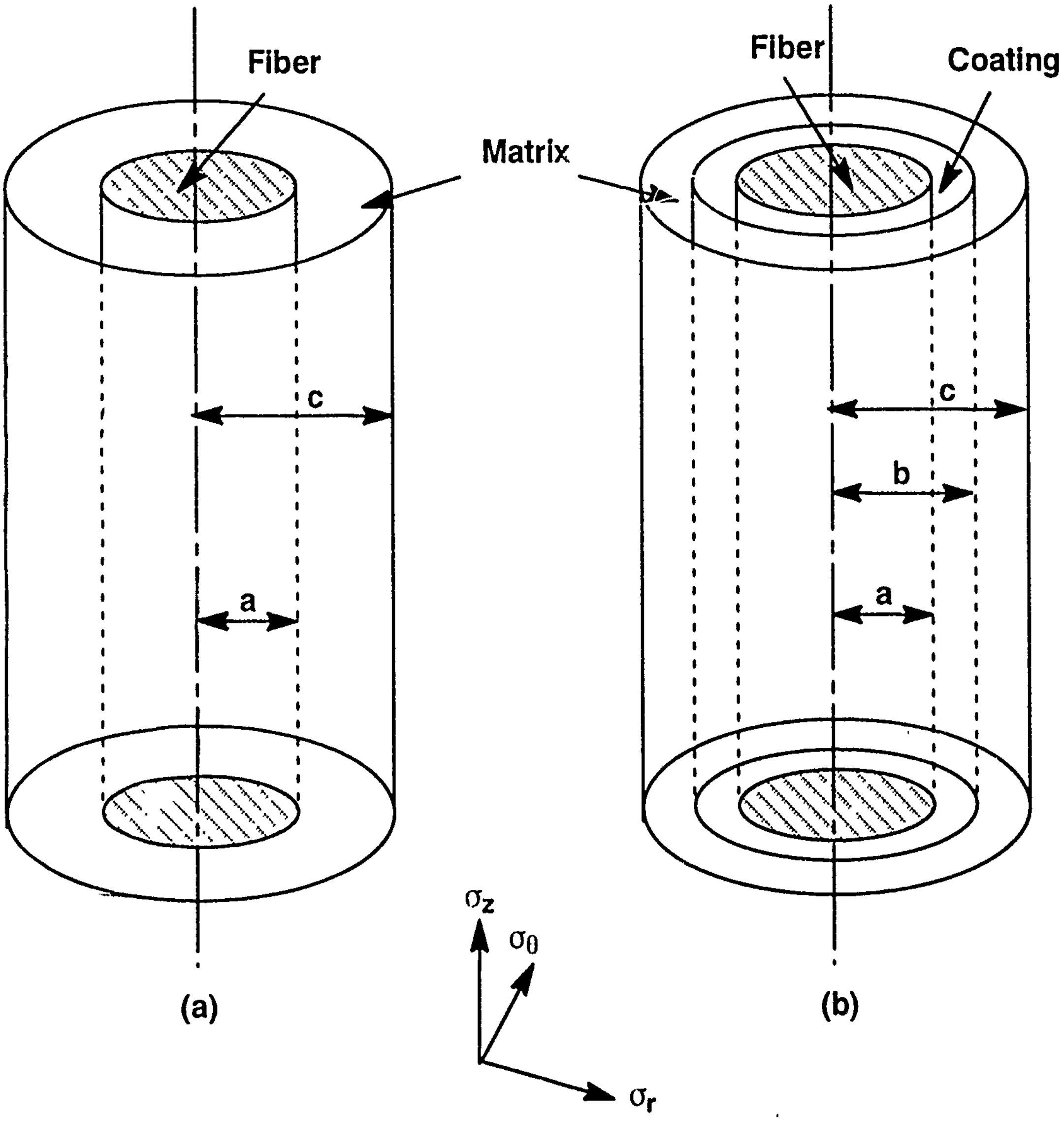
Fiber
Matrix
Fiber
Coating
c
a
c
b
a
σ_z
σ_θ
σ_r
(a)
(b)

Figure 36

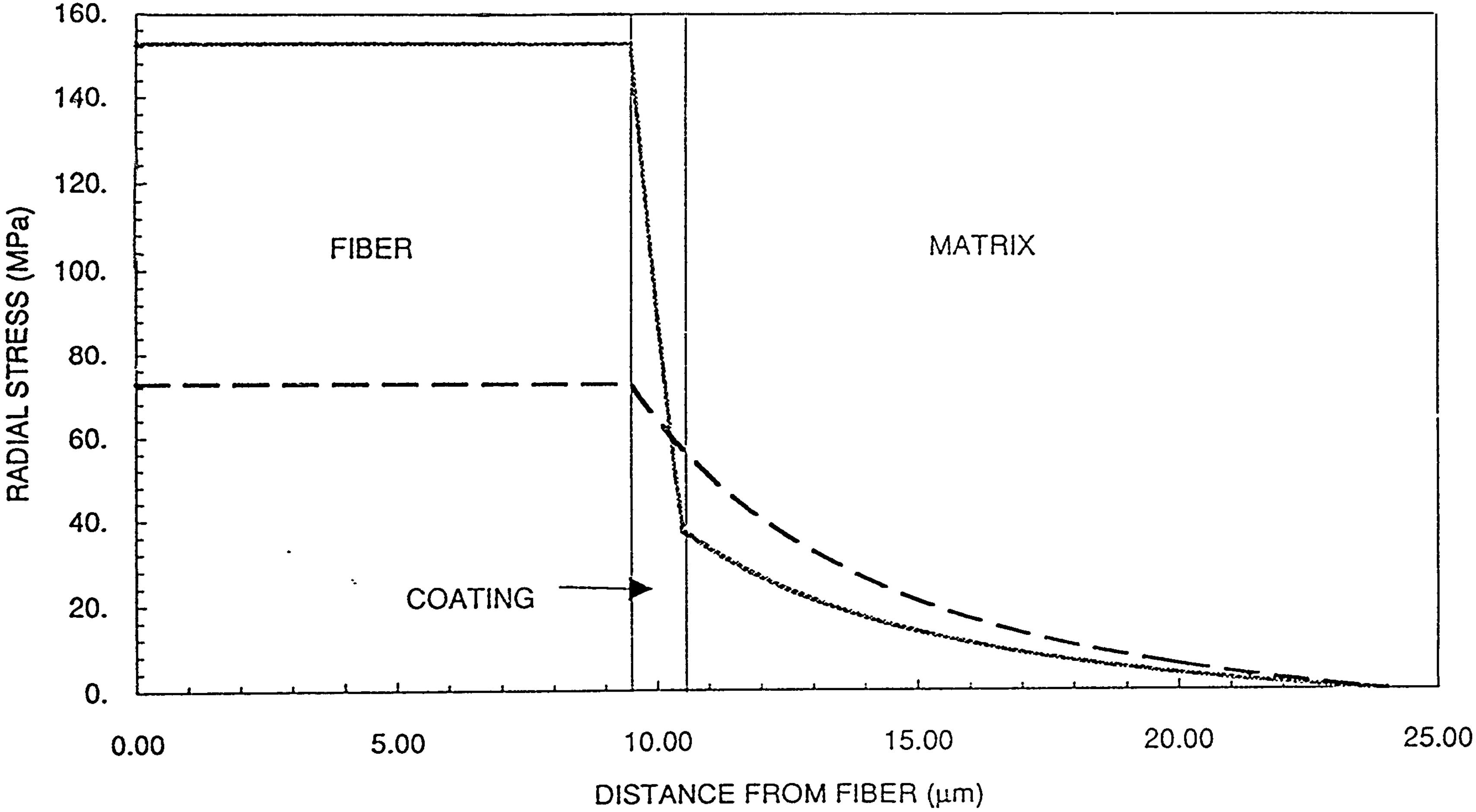
160.
140.
120.
100.
80.
60.
40.
20.
0.
RADIAL STRESS (MPa)
0.00
5.00
10.00
15.00
20.00
25.00
DISTANCE FROM FIBER (µm)
FIBER
MATRIX
COATING

Figure 37 (a)

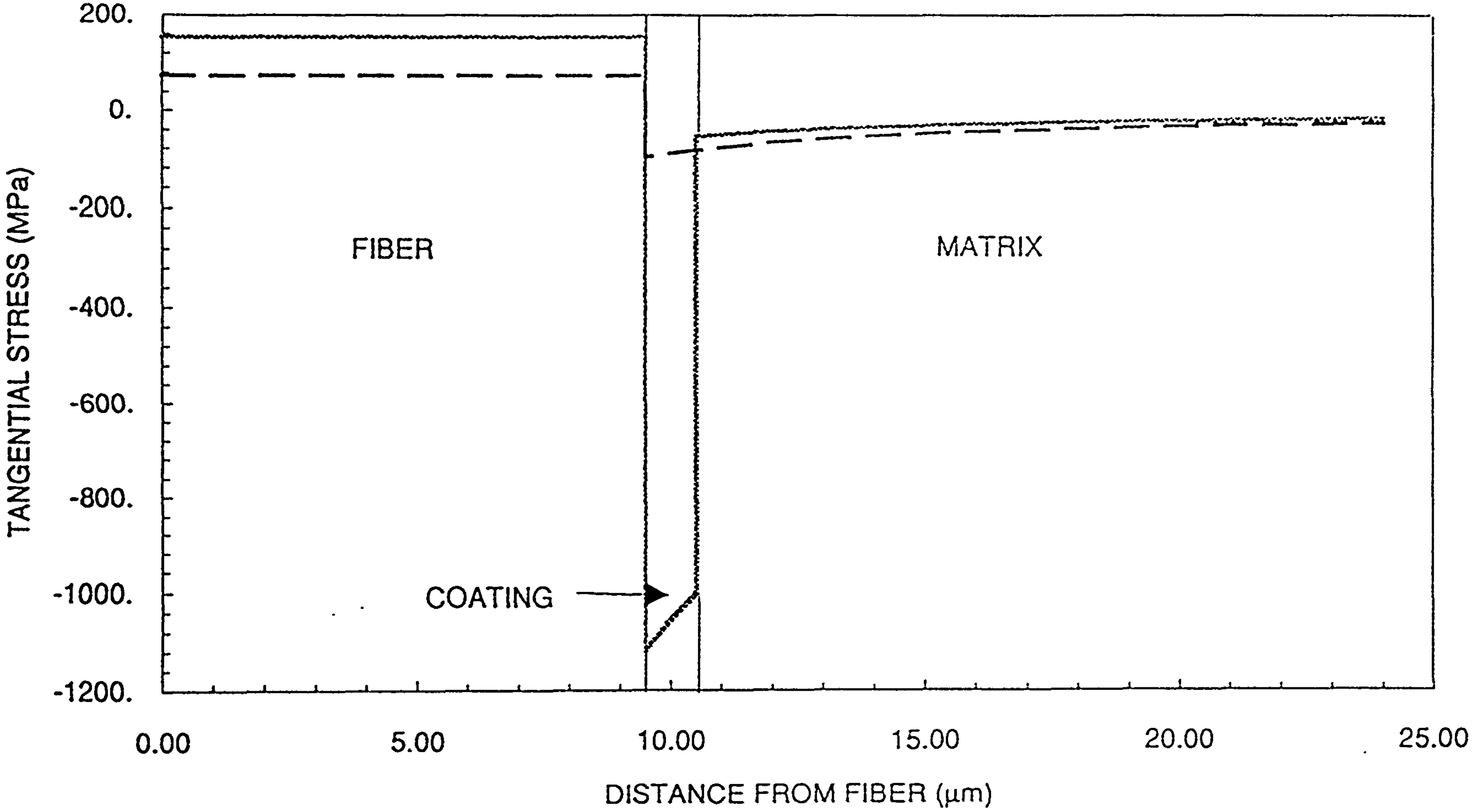
200.
0.
-200.
-400.
-600.
-800.
-1000.
-1200.
TANGENTIAL STRESS (MPa)
FIBER
MATRIX
COATING
0.00
5.00
10.00
15.00
20.00
25.00
DISTANCE FROM FIBER (μm)

Figure 37 (b)

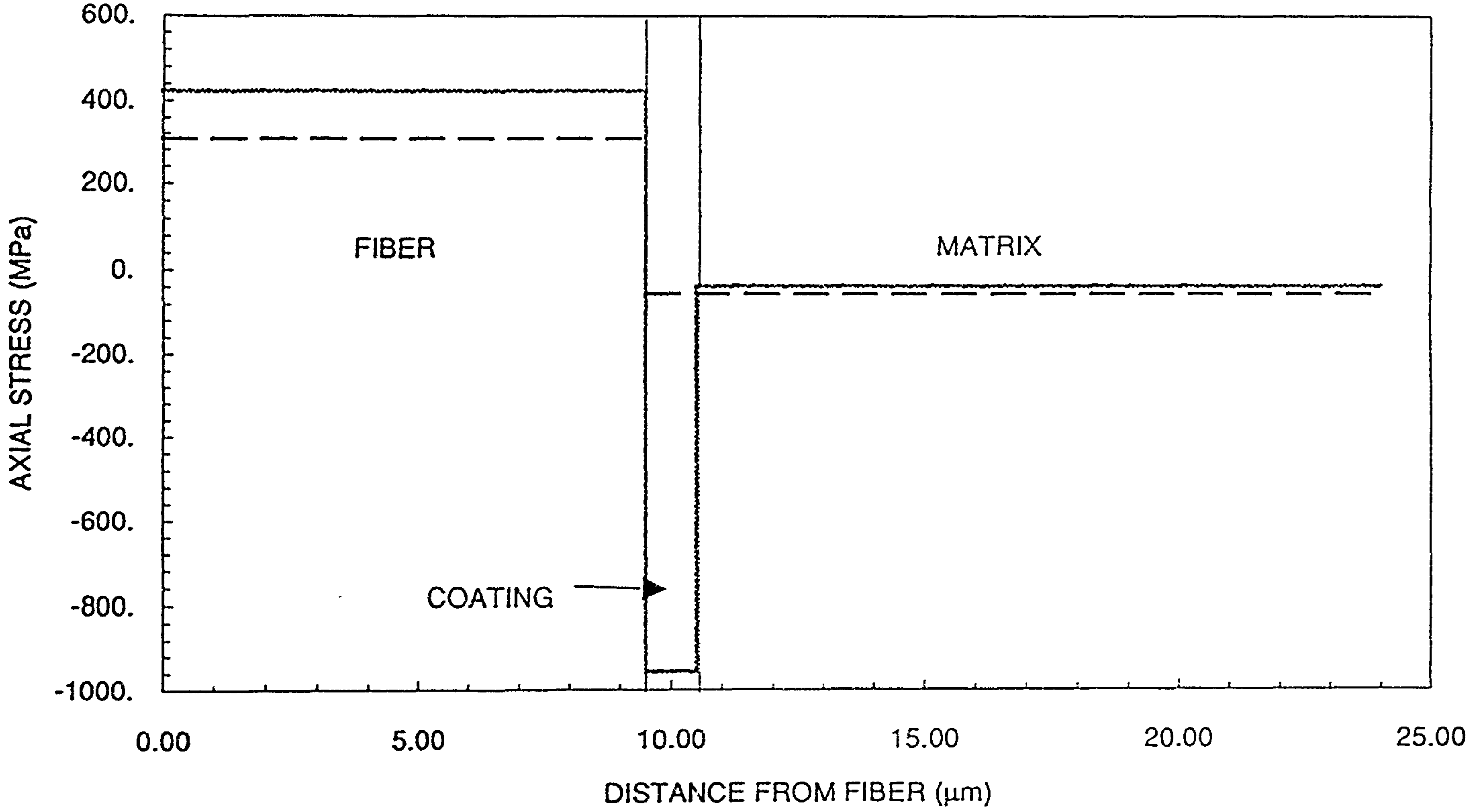
600.
400.
200.
0.
-200.
-400.
-600.
-800.
-1000.
AXIAL STRESS (MPa)
FIBER
MATRIX
COATING
0.00
5.00
10.00
15.00
20.00
25.00
DISTANCE FROM FIBER (µm)

Figure 37 (c)

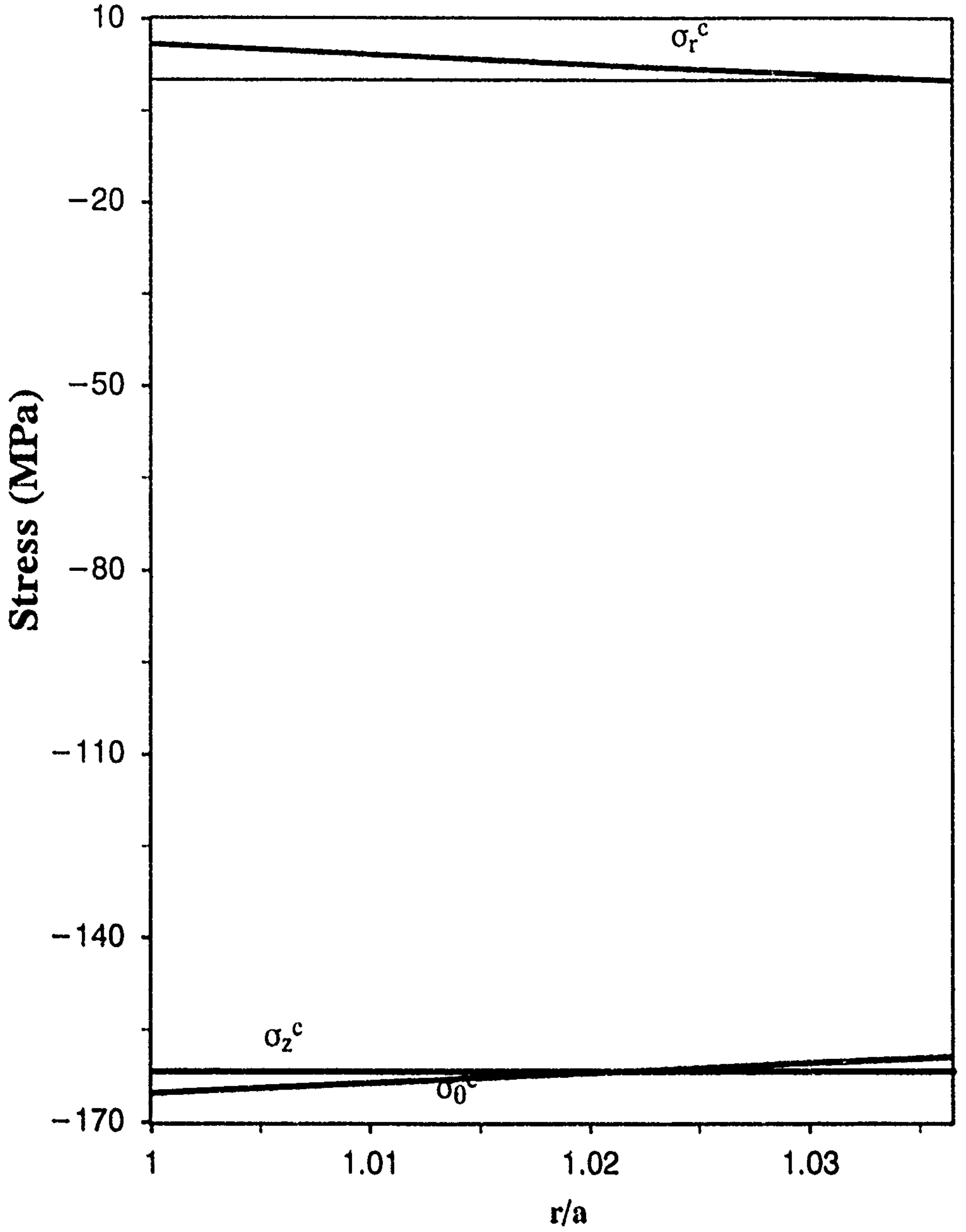
10
−20
−50
−80
−110
−140
−170
Stress (MPa)
1
1.01
1.02
1.03
r/a
σ_r^c
σ_z^c
σ_θ^c

Figure 38

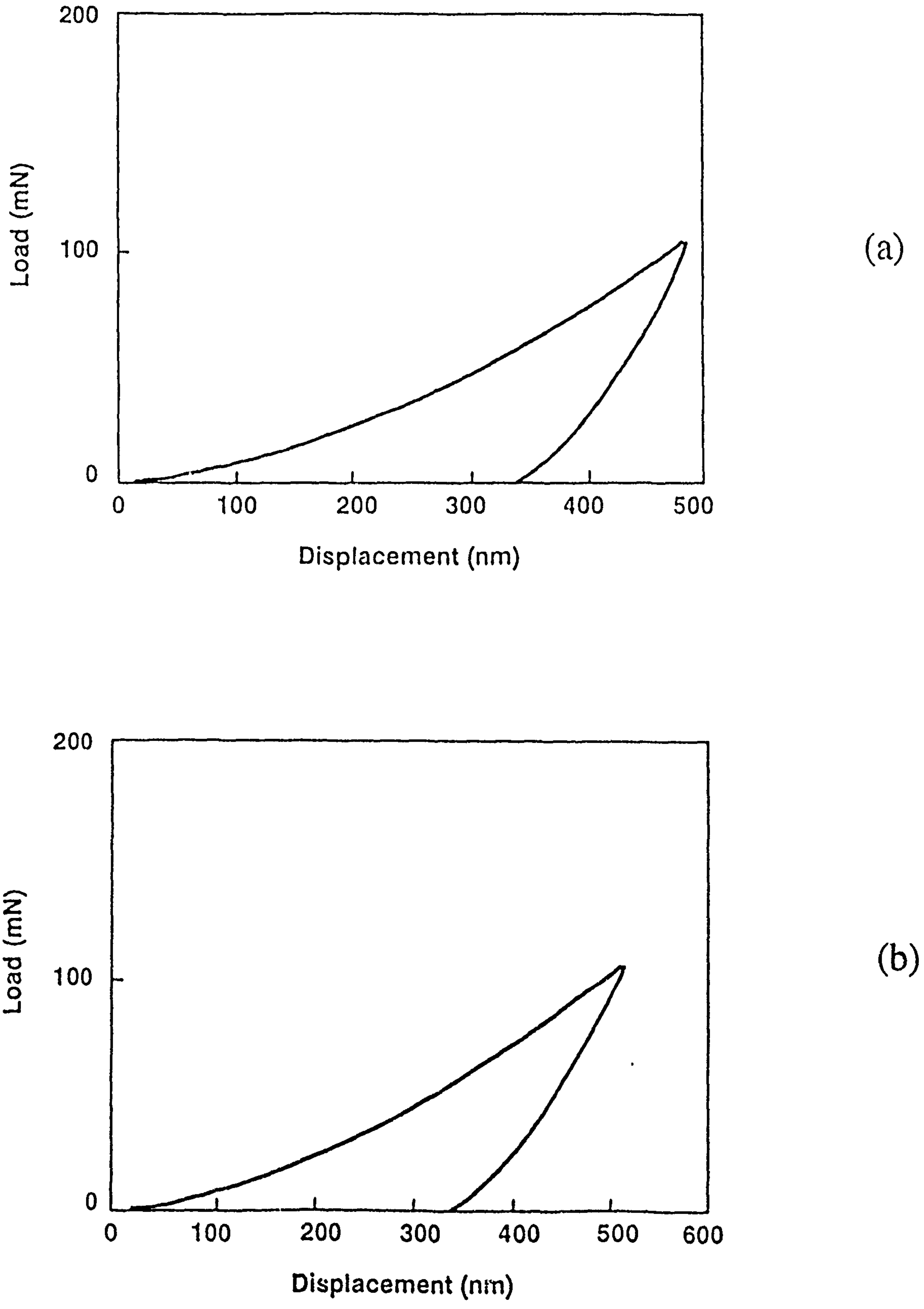
200
100
0
Load (mN)
0
100
200
300
400
500
Displacement (nm)
(a)
200
100
0
Load (mN)
0
100
200
300
400
500
600
Displacement (nm)
(b)

Figure 39

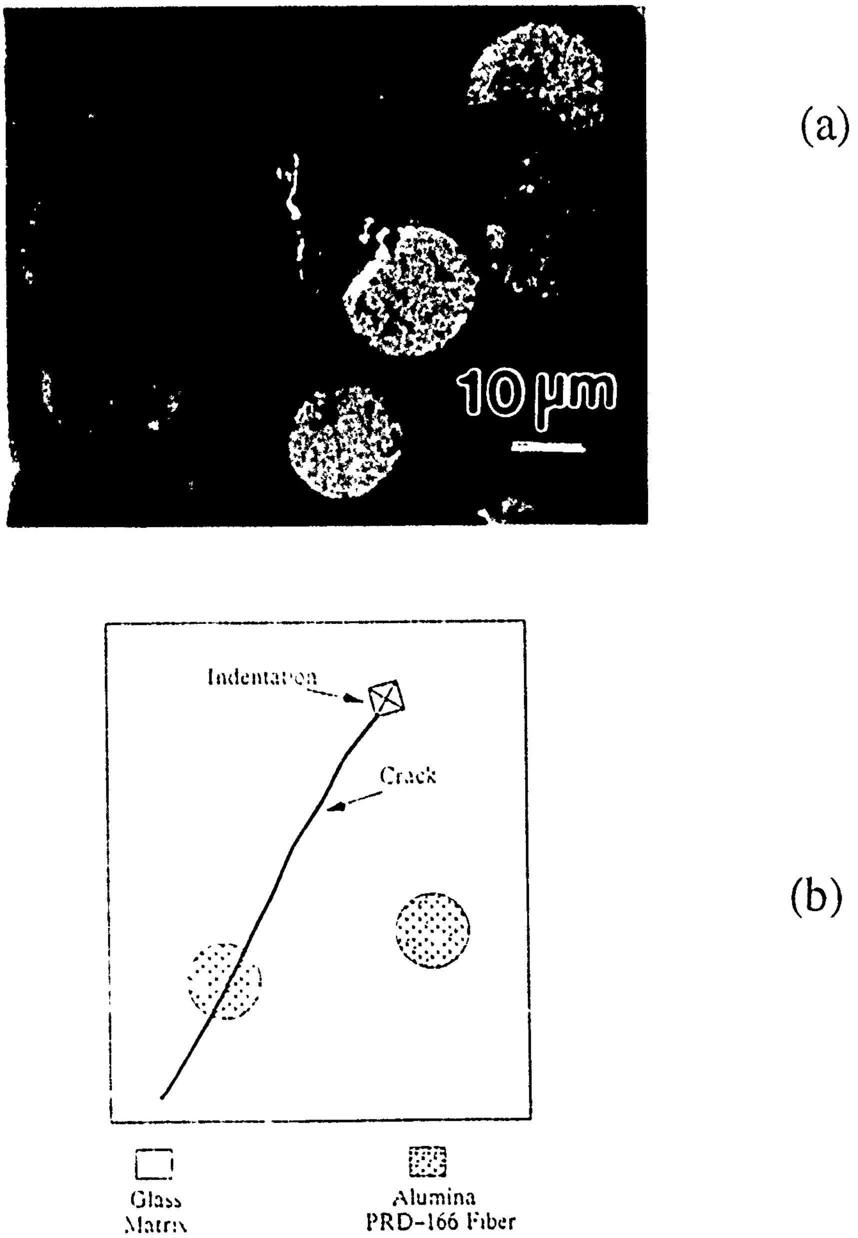
(a)
10 µm
Indentation
Crack
(b)
Glass Matrix
Alumina PRD-166 Fiber

Figure 40

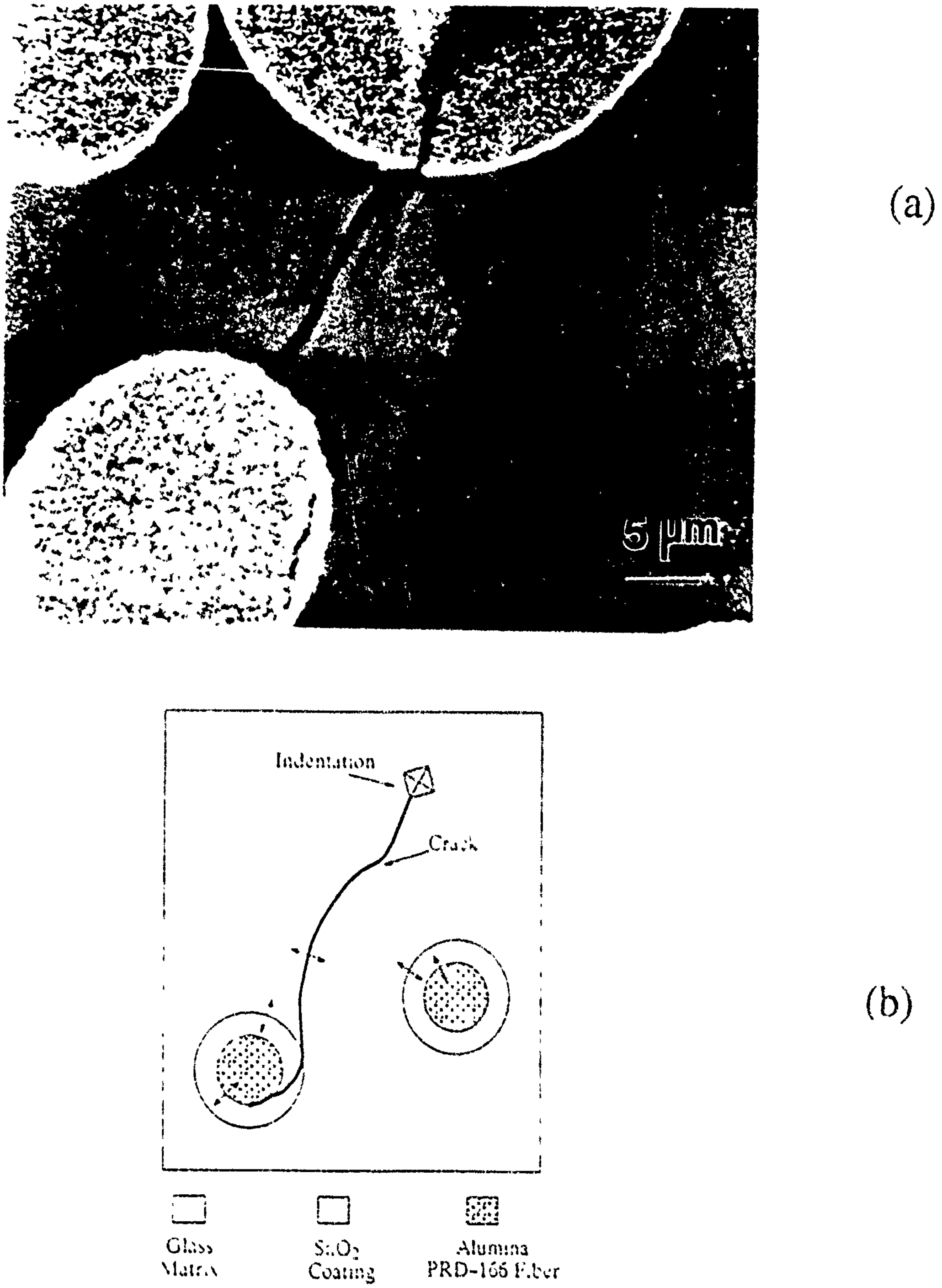
(a)
5 μm
Indentation
Crack
(b)
Glass Matrix
SnO$_2$ Coating
Alumina PRD-166 Fiber

Figure 41

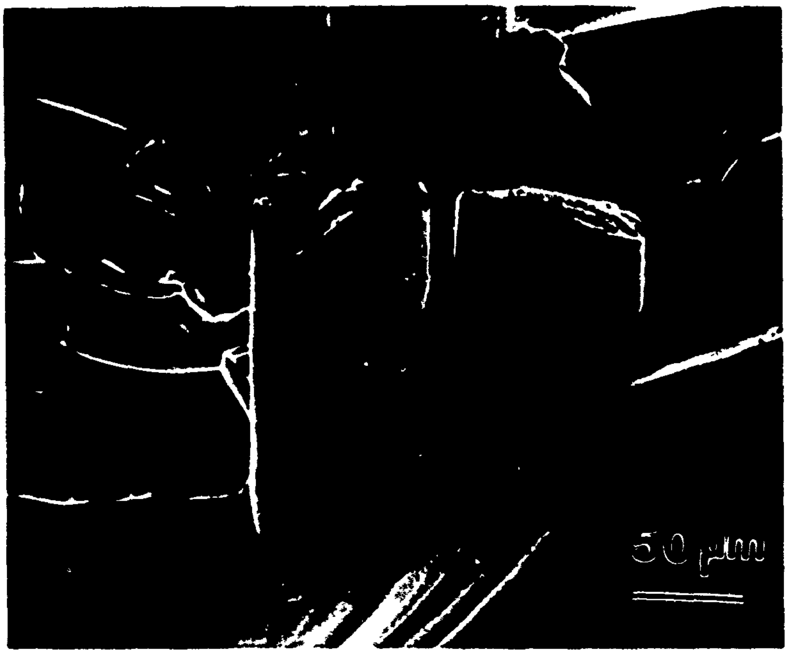

Figure 42

[illegible] Chemical composition of PRD−166 fiber

[illegible]	80−85
ZrO_2	15−20

Data of Du Pont Co.

Table 1b. Physical properties of the PRD−166 fiber

Fiber Diameter	20 μm
Tensile Modulus	380 GPa
Tensile Strength	2025 MPa
Coeff. of Thermal Exp.	9×10^{-6} / °C
Use Temperature	1200 °C

Table 2. (a) Chemical composition of Nextel 480 fiber.

Al_2O_3	70
SiO_2	28
B_2O_3	2

Data of 3M Co.

Tabl 2. (b) Physical properties of Nextel 480 fiber.

Filament Diameter: Major axis	10–13 μm
Minor axis	7–9 μm
Tensile Modulus	221 GPa [63]
Tensile Strength	2043 MPa [63]
Thermal Expansion Coeff:	
25–500 ^{o}C	$4.38 \times 10^{-6}/^{o}\mathrm{C}$
500–1000 ^{o}C	$4.99 \times 10^{-6}/^{o}\mathrm{C}$
Use Temperature	1371 ^{0}C
Filament Count	740–780
Crystal Size	<500 nm
Crystal Type	Mullite
Density	3.05 g/cc

Data of 3M Co.

Table 3a. Composition of N51A glass matrix

Manufacturer: Owens Illinois Inc.

	weight %		**atomic %**
SiO_2	72	Si	33.6
B_2O_3	12	B	3.8
Al_2O_3	7	Al	3.7
CaO	1	Ca	0.7
Na_2O	6	Na	4.5
K_2O	2	K	1.7
BaO	< 0.1	Ba	trace
		O_2	rest

Table 3b. Physical properties of the N51A glass matrix

E (GPa)	72
VHN (GPa)	0.63
K_c (MPa $m^{1/2}$)	0.7–0.8
ϱ (g/cm^3)	2.2
α ($^0C^{-1}$)	7×10^{-6}
melting point (^{0}C)	—
annealing point (^{0}C)	570
softening point (^{0}C)	785

Table 4. Properties of commercial mullite powder used as a matrix material

Chemical formula	$3Al_2O_3 \cdot 2SiO_2$
Purity	>99.2%
Surface area	2 m^2/g
Agglomerate size distribution	24 wt% for <1.0 μm
	34 wt% for <1.5 μm
	85 wt% for <3.0 μm
	100 wt% for <6.0 μm
Tap density	0.9 g/cm^3

Baikowski International Corp.

Table 5. Properties of SnO_2

E (GPa)	233
VHN (GPa)	1.13
K_{Ic} (MPa $m^{1/2}$)	—
ϱ (g/cm^3)	6.95
α ($^0C^{-1}$)	5.23×10^{-6}
melting point (^{0}C)	1630

Table 6. Conditions for deposition of SnO_2 by the CVD process

Temperature	500 °C
Time	5 minutes
Temp of $SnCl_4$	300 K
Temp of H_2O	343 K
p_{H_2O}	0.238 atm
p_{SnCl_4}	0.034 atm
Flow rate of N_2	1 liter / min
Flow rate of O_2	0.6 liter / min
n_{N_2}	4.46×10^{-2} moles/min
n_{O_2}	2.67×10^{-2} moles/min

Table 7. Characteristics of colloidal precursors

Precursor		Composition (wt%)	pH	Surface area (m^2/g)	Stabilizing alkali
Boehmite	Dispal 11N7[†]	80 Al_2O_3	7[§]	110	
	Catapal D[†]	70.7 Al_2O_3	2.5–5[§]	230	
Silica	Ludox AS[‡]	40 SiO_2	9.1	140	NH_3
	Ludox LS[‡]	30 SiO_2	8.1	220	Na_2O (0.1 wt%)
	SP-30[†]	30 SiO_2	9.9	340	Na_2O (0.5 wt%)

[†] Remet Chemical, Chadwicks, NY.

[‡] Dupont, Wilmington, DE.

[§] pH for dispersion.

Table 8. Weibull parameters of PRD−166 fiber.

Fiber condition	α (MPa)	β	*Weibull Mean Strength (MPa)*	*Standard Deviation (MPa)*	*Coeff. of Variation, %*	*Correlation Coeff., r^2*
As−received	$.21 \times 10^{-11}$	3.7	1375	418	30	0.99
SnO_2 Coated (0.4 μm)	$.12 \times 10^{-13}$	4.5	1060	265	25	0.98
SnO_2 Coated (0.5 μm)	$.98 \times 10^{-12}$	4.0	966	273	28	0.95
SnO_2 Coated (0.8 μm)	$.49 \times 10^{-11}$	3.8	851	279	33	0.99
SnO_2 Coated (2.0 μm)	$.45 \times 10^{-11}$	3.9	702	227	32	0.96
SnO_2 Coated (10 μm)	$.58 \times 10^{-7}$	3.2	166	56	34	0.96

Table 9. Weibull parameters of Nextel 480 fiber.

Fiber condition	α, MPa$^{-\beta}$	β	Weibull Mean Strength, $\bar{\sigma}$, MPa	Standard Deviation, s MPa	Coefficient of Variation,%
Uncoated	6.39×10^{-13}	3.75	1627.29	484.44	29.77
Boron Nitride Coated (0.1μm)	1.00×10^{-19}	5.69	2000.98	405.72	20.32
Boron Nitride Coated (0.2μm)	1.21×10^{-15}	4.34	2471.02	643.28	26.03
Boron Nitride Coated (0.3μm)	4.09×10^{-17}	4.97	1823.88	428.18	23.03

Table 10. Strength of Nextel/glass composites.

Sample	Average Strength (MPa)	Coefficient of Variation (%)
N51A Glass Matrix	64	14.5
Nextel 480/Glass	65.7	18.9
BN coated Nextel 480/Glass	76.3	5.1

Table 11. Static fracture toughness of Nextel/glass composites.

Sample	Average K_{Ic} (MPa $m^{1/2}$)	Coefficient of Variation (%)
Nextel 480/Glass	1.11	8.38
BN coated Nextel 480/Glass (0.2 μm coating)	2.12	10.68

Table 12. Fracture energy of Nextel/glass composites.

Sample	Average fracture energy per unit area of crack surface (J/m^2)
N51 A Glass matrix	6–8
Nextel 480/Glass	28.9
BN coated Nextel 480/Glass (50% max. load)	152.7

Table 13. Bend strength and work of fracture of mullite/mullite composites fabricated using a colloidal sol-gel processed mullite powder

	Nextel 480/mullite			Nextel 550/mullite	
	Uncoated	0.3 μm BN	1 μm BN	Uncoated	SiC/BN[†]
Phase					
As-HP[‡]	δ-alumina mullite	δ-alumina mullite	δ-alumina mullite	δ-alumina	δ-alumina
HT[§] (in air & N_2)	mullite	mullite	mullite	mullite	mullite
Bend strength (MPa)					
As-HP	114	190	324	84	158
HT (in air)	106	314	204	71	148
HT (in N_2)	–	–	246	–	201
Work of fracture (J/m^2)					
As-HP	230	358	2985	133	582
HT (in air)	156	908	600	76	237
HT (in N_2)	–	–	1103	–	518

[†] 0.2 μm of thickness for each coating.

[‡] As-hotpressed.

[§] Heat-treated at 1300°C for 1h.

Table 14. Comparison of experimental coeffecient of thermal expansion of PRD−166/glass and PRD−166/SnO_2/glass composites with values predicted by various theoretical models

Composite	V_f	Experimental (10^{-6}/°C)	Schapery (10^{-6}/°C)	Chamis (10^{-6}/°C)	Chamberlain (10^{-6}/°C)		Rosen and Hashin (10^{-6}/°C)
					F=0.9069	F=0.7854	
PRD−166 / glass (Longitudinal)	0.065	6.2	6.82	6.82	6.82	6.82	6.19
	0.2	6.81	7.7	7.7	7.7	7.7	6.6
	0.44	7.26	8.43	8.43	8.43	8.43	7.32
PRD−166 / glass (Transverse)	0.065	5.45	6.03	7.07	6.32	6.23	4.5
	0.2	6.65	6.32	7.81	6.86	6.72	4.7
	0.44	6.55	7.04	8.39	7.08	7.9	6.0
PRD−166 / SnO_2 /glass (Longitudinal)	0.2	7.09	7.42	7.42	7.42	7.42	6.45
	0.3	7.12	7.7	7.7	7.7	7.7	6.68
PRD−166 / SnO_2 /glass (Transverse)	0.2	6.19	6.2	7.6	6.8	6.55	3.4
	0.3	6.52	6.45	7.96	7.09	6.78	5.26

Table 15. Roughness Amplitude (A), Fiber Radius (r_f), and Ratio (A/r_f) for PRD–166 and Saphikon fibers.

	PRD--166	Sapphire
A, μm	0.64	0.43
r_f, μm	20	43.5
A/r_f	0.064	0.009

Appendix A : Effect of Tin Dioxide Coating on Tensile Strength of PRD–166 Fibers.

Scripta METALLURGICA
et MATERIALIA

Vol. 25, pp. 361-366, 1991
Printed in the U.S.A.

Pergamon Press plc
All rights reserved

EFFECT OF TIN DIOXIDE COATING ON TENSILE STRENGTH OF ALUMINA FIBERS

S. N. Patankar, R. Venkatesh, and K. K. Chawla
New Mexico Institute of Mining and Technology
Socorro, NM 87801

(Received August 20, 1990)
(Revised November 19, 1990)

Introduction

Incorporation of fibers in glass or ceramics is one of the most promising methods to improve the toughness. The increase in the toughness of fiber-reinforced ceramic or glass matrix composites is a consequence of a number of energy absorbing mechanisms such as fiber/matrix debonding, crack deflection and fiber pullout that are brought into play by the weak fiber matrix interface (1-2). Many fibers can potentially be used as reinforcement for a ceramic or glass matrix. Alumina fiber, because it is an oxide fiber, is thermally more stable than most of the other nonoxide fibers and hence would appear to be an ideal reinforcement for glass and ceramic matrix composites. PRD - 166 is a relatively new fiber from Du Pont which contains about 20 wt. % of partially stabilized zirconia in alpha alumina. The dispersion of zirconia in PRD - 166 impedes the grain growth in alumina and consequently imparts high strength to the fiber (3). Because of the chemical reaction between glass and alumina, reinforcement of glass with alumina fibers is expected to offer a low level of toughness (4-8). One way of controlling the chemical interaction at the alumina fiber glass matrix interface is to use SnO_2 as a barrier layer between alumina and glass (4). SnO_2, by virtue of its low solubility in glass and because it has little or no solubility in alumina, serves as a diffusion barrier between alumina and glass. Diffusion studies have indicated absence of diffused tin in alumina and a small amount of tin diffusion in glass (4). Before studying in detail the behavior of SnO_2 coated fibers in a glass matrix, it would be useful to evaluate the effect of SnO_2 coating on the strength of alumina fibers. Also, since no information of a statistical nature on PRD-166 is available, the aim of this work was to study the effect of tin dioxide coating on the tensile strength alumina (PRD-166) fibers using a two parameter Weibull distribution.

Experimental Procedure

Alumina fibers (PRD 166) manufactured by Du Pont were used in the present work. These fibers were coated with SnO_2 by a chemical vapor deposition technique (4). Moisture required for chemical vapor deposition (CVD) was introduced into the reaction chamber by bubbling oxygen through water, while nitrogen gas was used as carrier gas for $SnCl_4$ during the CVD process. The flow rate of the nitrogen gas was maintained at 0.6 liters per minute and that of oxygen at 1.0 liter per minute during the coating process. The deposition temperature was 500°C. The single fiber tensile testing of the as-received and SnO_2 coated Al_2O_3 fibers with a gauge length of 17 mm was done on individual fibers by mounting them on a paper frame. The sides of the each frame were carefully slashed while it was gripped in the tensile testing machine. An Instron tensile testing machine with a 5 N load cell was used for testing the fibers at a crosshead speed of 0.1 mm/s. About eighty fibers were tested in as-received and coated condition. Prior to the tensile testing, the diameter of the individual mounted fiber was measured by viewing it in a longitudinal direction in an optical microscope. The tensile strength data obtained for the coated as well as as-received Al_2O_3 fibers were analyzed using a two parameter Weibull distribution. According to Weibull distribution (9), which is based on weakest link theory, the probability of failure of fiber at stress σ is given by

$$F(\sigma) = 1 - \exp(-\alpha\sigma^{\beta}) \qquad (1)$$

where β, the Weibull modulus, is the measure of the scatter in the tensile strength data and α is a scale parameter (10). Eq. 1 we can be rearranged as

$$\ln [\ln (1/1-F(\sigma))] = \beta \ln\sigma + \ln\alpha \qquad (2)$$

From Eq. 2, we can obtain α and β graphically. Tensile strength values of the number of fibers obtained were arranged in an increasing order and each strength value was assigned a probability of failure using an estimator. The estimator $F(\sigma_i) = i / (1 + N)$ was used in the present study as it gives a conservative failure probability ($F(\sigma_i)$ is the probability of failure corresponding to the ith strength value) and, from a

0036-9748/91 $3.00 + .00

Scripta METALLURGICA
et MATERIALIA

Vol. 25, pp. 361-366, 1991
Printed in the U.S.A.

Pergamon Press plc
All rights reserved

EFFECT OF TIN DIOXIDE COATING ON TENSILE STRENGTH OF ALUMINA FIBERS

S. N. Patankar, R. Venkatesh, and K. K. Chawla
New Mexico Institute of Mining and Technology
Socorro, NM 87801

(Received August 20, 1990)
(Revised November 19, 1990)

Introduction

Incorporation of fibers in glass or ceramics is one of the most promising methods to improve the toughness. The increase in the toughness of fiber-reinforced ceramic or glass matrix composites is a consequence of a number of energy absorbing mechanisms such as fiber/matrix debonding, crack deflection and fiber pullout that are brought into play by the weak fiber matrix interface (1-2). Many fibers can potentially be used as reinforcement for a ceramic or glass matrix. Alumina fiber, because it is an oxide fiber, is thermally more stable than most of the other nonoxide fibers and hence would appear to be an ideal reinforcement for glass and ceramic matrix composites. PRD - 166 is a relatively new fiber from Du Pont which contains about 20 wt. % of partially stabilized zirconia in alpha alumina. The dispersion of zirconia in PRD - 166 impedes the grain growth in alumina and consequently imparts high strength to the fiber (3). Because of the chemical reaction between glass and alumina, reinforcement of glass with alumina fibers is expected to offer a low level of toughness (4-8). One way of controlling the chemical interaction at the alumina fiber glass matrix interface is to use SnO_2 as a barrier layer between alumina and glass (4). SnO_2, by virtue of its low solubility in glass and because it has little or no solubility in alumina, serves as a diffusion barrier between alumina and glass. Diffusion studies have indicated absence of diffused tin in alumina and a small amount of tin diffusion in glass (4). Before studying in detail the behavior of SnO_2 coated fibers in a glass matrix, it would be useful to evaluate the effect of SnO_2 coating on the strength of alumina fibers. Also, since no information of a statistical nature on PRD-166 is available, the aim of this work was to study the effect of tin dioxide coating on the tensile strength alumina (PRD-166) fibers using a two parameter Weibull distribution.

Experimental Procedure

Alumina fibers (PRD 166) manufactured by Du Pont were used in the present work. These fibers were coated with SnO_2 by a chemical vapor deposition technique (4). Moisture required for chemical vapor deposition (CVD) was introduced into the reaction chamber by bubbling oxygen through water, while nitrogen gas was used as carrier gas for $SnCl_4$ during the CVD process. The flow rate of the nitrogen gas was maintained at 0.6 liters per minute and that of oxygen at 1.0 liter per minute during the coating process. The deposition temperature was 500°C. The single fiber tensile testing of the as-received and SnO_2 coated Al_2O_3 fibers with a gauge length of 17 mm was done on individual fibers by mounting them on a paper frame. The sides of the each frame were carefully slashed while it was gripped in the tensile testing machine. An Instron tensile testing machine with a 5 N load cell was used for testing the fibers at a crosshead speed of 0.1 mm/s. About eighty fibers were tested in as-received and coated condition. Prior to the tensile testing, the diameter of the individual mounted fiber was measured by viewing it in a longitudinal direction in an optical microscope. The tensile strength data obtained for the coated as well as as-received Al_2O_3 fibers were analyzed using a two parameter Weibull distribution. According to Weibul distribution (9), which is based on weakest link theory, the probability of failure of fiber at stress σ is given by

$$F(\sigma) = 1 - exp(-\alpha\sigma^{\beta}) \qquad (1)$$

where β, the Weibull modulus, is the measure of the scatter in the tensile strength data and α is a scale parameter (10). Eq. 1 we can be rearranged as

$$ln\ [\ ln\ (1/1-F(\sigma))\ ] = \beta ln\sigma + ln\alpha \qquad (2)$$

From Eq. 2, we can obtain α and β graphically. Tensile strength values of the number of fibers obtained were arranged in an increasing order and each strength value was assigned a probability of failure using an estimator. The estimator $F(\sigma_i) = i\ /\ (1 + N)$ was used in the present study as it gives a conservative failure probability ($F(\sigma_i)$ is the probability of failure corresponding to the i^{th} strength value) and, from a

0036-9748/91 $3.00 + .00

reliability point of view, is the probably the best choice (10-13). Substituting the estimator $F(\sigma_i) = i/(1+N)$ in Eq. 2, we have

$$\ln[\ln (N+1) / (N+1-i)] = \beta \ln\sigma_i + \ln\alpha \qquad (3)$$

According to Eq. 3, a plot of $\ln((N+1)/(N+1-i))$ against σ_i on a log-log graph will be a straight line if the tensile strength data follow Weibull distribution. The slope of the line then will give β and the intercept that the line makes with the Y-axis will give α. Knowing α and β, the Weibull mean tensile strength, $\bar{\sigma}$, standard deviation, s, and coefficient of variation, C.V., are given by the following expressions :

$$\bar{\sigma} = \alpha^{-1/\beta}\,\Gamma(1+1/\beta), \quad s = \alpha^{-1/\beta}[\Gamma(1+2/\beta) - \{\Gamma^2(1+1/\beta)\}]^{1/2}, \text{ and C.V.} = 100\,(s/\bar{\sigma})$$

Results and Discussion

A plot of the natural log of tensile strength σ_i and $\ln(N+1/N+1-i)$ for the as-received alumina (PRD-166) fibers is shown in Fig. 1a. The straight line plot implies that the tensile strength data for the as-received alumina fibers follow Weibull distribution. The correlation coefficient (r^2) value was 0.99. The different Weibull parameters of the as-received alumina fibers are listed in Table I. The Weibull mean strength of as-received alumina fibers obtained in the present work was 1375 MPa, which is low compared to the value of 2070 MPa reported by Romine (3). This could be partly due to the smaller gauge length used by Romine, 6.4 mm as against 17 mm used in the present study, and partly due to any processing-induced defects in the as-received fiber spool. Figure 2 shows an example of such a defect in the form of a huge void in the fiber interior. Similar processing-induced defects have been reported by Pysher et al. (14) in this newly developed fiber.

Tensile strength data of tin dioxide coated alumina fibers, similar to that of the as-received alumina fibers, followed Weibull distribution, Fig. 1b. The Weibull parameters of the tin dioxide coated alumina fiber are given in Table I. The tin dioxide coated alumina fibers exhibited Weibull mean strength lower than that of the as-received fiber, and the decrease in the strength of the coated fiber increased with the increase in the coating thickness. Some loss in strength of the coated fibers could be due to the high temperature exposure of alumina fiber during tin dioxide deposition. This fact becomes apparent from Table II, which shows the effect of high temperature on the tensile strength of the uncoated alumina fibers. Another source of strength loss in the coated fibers could be the thermal stresses generated during the deposition. In order to understand the effect of thermal stresses in the present case, we considered the thermoelastic analysis of the composite fiber: a cylinder of alumina fiber having a sleeve of tin dioxide. Assuming plane strain conditions, the three stress components: axial stress, σ_z, radial stress, σ_r and circumferential stress, σ_θ for the fiber (component 1) and the coating (component 2) are given by the following set of equations [15,16]:

$$\sigma_{r1} = \sigma_{\theta 1} = [1-b^2/a^2]\Sigma_{r\theta}, \quad \sigma_{z1} = [1-b^2/a^2]\sigma_{z2}, \quad \sigma_{r2} = [1-b^2/r^2]\Sigma_{r\theta}, \text{ and } \sigma_{\theta 2} = [1+b^2/r^2]\Sigma_{r\theta}$$

$$\sigma_{z2} = E_1E_2\,(\Delta\epsilon_f/D)\,[E_1(1+\nu)\,(1+b^2/a^2) + E_2(1+\nu)\,(b^2/a^2-1)]$$

$$\Sigma_{r\theta} = E_1E_2\,(\Delta\epsilon_f/D)\,[E_1(1+\nu) + E_2(1+\nu)\,(b^2/a^2-1)]$$

$$D = \begin{vmatrix} 2[E_1\nu + E_2\nu\,(b^2/a^2-1)] & E_1 + E_2\,(b^2/a^2-1)] \\ \{E_1\,[1-\nu+(1+\nu)\,(b^2/a^2)] & E_1\nu + E_2\nu\,(b^2/a^2-1) \\ +\,E_2\,(1-\nu)\,(b^2/a^2-1)\} & \end{vmatrix}$$

where 'a' and 'b' are the radii of the as received and tin dioxide coated fibers, respectively, 'E' is the young's modulus, and 'ν' is the Poisson's ratio. The thermal strain is given by

$$\epsilon_f = \int_{T_i}^{T_f} (\alpha_1 - \alpha_2)\, dT = (\alpha_1 - \alpha_2)\,(T_f - T_i)$$

where 'α' is the thermal expansion coefficient and 'T_i' and 'T_f' are the initial and final temperature, respectively. The thermal expansion coefficient and elastic modulus data used to compute the thermal stresses reliability point of view, is the probably the best choice (10-13). Substituting the estimator $F(\sigma_i) = i/(1 + N)$ in Eq. 2, we have

$$\ln[\ln (N+1) / (N+1-i)] = \beta \ln\sigma_i + \ln\alpha \qquad (3)$$

According to Eq. 3, a plot of $\ln((N+1)/(N+1-i))$ against σ_i on a log-log graph will be a straight line if the tensile strength data follow Weibull distribution. The slope of the line then will give β and the intercept that the line makes with the Y-axis will give α. Knowing α and β, the Weibull mean tensile strength, $\bar{\sigma}$, standard deviation, s, and coefficient of variation, C.V., are given by the following expressions :

$$\bar{\sigma} = \alpha^{-1/\beta}\,\Gamma(1+1/\beta),\quad s = \alpha^{-1/\beta}[\Gamma(1+2/\beta) - (\Gamma^2(1+1/\beta))]^{1/2},\ \text{and C.V.} = 100\ (s/\bar{\sigma})$$

Results and Discussion

A plot of the natural log of tensile strength σ_i and $\ln(N+1/N+1-i)$ for the as-received alumina (PRD-166) fibers is shown in Fig. 1a. The straight line plot implies that the tensile strength data for the as-received alumina fibers follow Weibull distribution. The correlation coefficient (r^2) value was 0.99. The different Weibull parameters of the as-received alumina fibers are listed in Table I. The Weibull mean strength of as-received alumina fibers obtained in the present work was 1375 MPa, which is low compared to the value of 2070 MPa reported by Romine (3). This could be partly due to the smaller gauge length used by Romine, 6.4 mm as against 17 mm used in the present study, and partly due to any processing-induced defects in the as-received fiber spool. Figure 2 shows an example of such a defect in the form of a huge void in the fiber interior. Similar processing-induced defects have been reported by Pysher et al. (14) in this newly developed fiber.

Tensile strength data of tin dioxide coated alumina fibers, similar to that of the as-received alumina fibers, followed Weibull distribution, Fig. 1b. The Weibull parameters of the tin dioxide coated alumina fiber are given in Table I. The tin dioxide coated alumina fibers exhibited Weibull mean strength lower than that of the as-received fiber, and the decrease in the strength of the coated fiber increased with the increase in the coating thickness. Some loss in strength of the coated fibers could be due to the high temperature exposure of alumina fiber during tin dioxide deposition. This fact becomes apparent from Table II, which shows the effect of high temperature on the tensile strength of the uncoated alumina fibers. Another source of strength loss in the coated fibers could be the thermal stresses generated during the deposition. In order to understand the effect of thermal stresses in the present case, we considered the thermoelastic analysis of the composite fiber: a cylinder of alumina fiber having a sleeve of tin dioxide. Assuming plane strain conditions, the three stress components: axial stress, σ_z, radial stress, σ_r and circumferential stress, σ_θ for the fiber (component 1) and the coating (component 2) are given by the following set of equations [15,16]:

$$\sigma_{r1} = \sigma_{\theta 1} = [1-b^2/a^2]\Sigma_{r\theta},\quad \sigma_{z1} = [1-b^2/a^2]\sigma_{z2},\quad \sigma_{r2} = [1-b^2/r^2]\Sigma_{r\theta},\ \text{and}\ \sigma_{\theta 2} = [1+b^2/r^2]\Sigma_{r\theta}$$

$$\sigma_{z2} = E_1E_2\ (\Delta\epsilon_t /D)\ [E_1(1+\nu)\ (1+b^2/a^2) + E_2(1+\nu)\ (b^2/a^2-1)]$$

$$\Sigma_{r\theta} = E_1E_2\ (\Delta\epsilon_t /D)\ [E_1(1+\nu) + E_2(1+\nu)\ (b^2/a^2-1)]$$

$$D = \begin{vmatrix} 2[E_1\nu + E_2\nu\,(b^2/a^2-1)] & E_1 + E_2\,(b^2/a^2-1)] \\ (E_1\,[1-\nu+(1+\nu)\,(b^2/a^2)] & E_1\nu + E_2\nu\,(b^2/a^2-1) \\ +\,E_2\,(1-\nu)\,(b^2/a^2-1)) & \end{vmatrix}$$

where 'a' and 'b' are the radii of the as received and tin dioxide coated fibers, respectively, 'E' is the young's modulus, and 'ν' is the Poisson's ratio. The thermal strain is given by

$$\Delta\epsilon_t = \int_{T_i}^{T_f} (\alpha_1 - \alpha_2)\,dT = (\alpha_1 - \alpha_2)\,(T_f - T_i)$$

where 'α' is the thermal expansion coefficient and 'T_i' and 'T_f' are the initial and final temperature, respectively. The thermal expansion coefficient and elastic modulus data used to compute the thermal stresses are given in Table III. Because of the unavailability of the Poisson's ratio, we assumed $\nu_1 = \nu_2 = \nu = 0.25$. The thermal stress distribution in the fiber and the tin dioxide coating is shown in Fig. 3.

The drop in strength of the coated fibers can be explained by considering the effects of the thermal stresses developed during the deposition of tin dioxide. First, the axial thermal stress in the fiber may lower the strength of the fiber by an amount equal to the thermal stress. Alternatively, the tensile radial stress at the interface can damage the alumina/SnO_2 interface. Figure 4 shows the cross-section of a coated alumina fiber. Note the notches in the coating, which could have come about during a chemical vapor deposition process or because of the radial tensile stress at the interface. Under an axial load, a notch in the coating would lead to failure of the coated alumina fiber. An example of such an occurrence is shown in Fig. 5. One of these notches in the coating becomes the flaw that leads to the failure of the alumina fiber. Thus, we can treat the coating thickness as a rough indicator of the initial flaw size, i.e., a single edge notch type flaw. Taking the toughness of the coated fiber with a single notch to be given by $K_{IC} = 1.12\,\sigma\,(\Pi a)^{1/2}$, the toughness values are given in Table IV. Here, we have taken the flaw size to be equal to the coating thickness. We have neglected the 10 µm thick coating specimen because it corresponds to 76% volume fraction of tin dioxide and 24% of alumina. Clearly, compared to the size of the possible interfacial flaws, this coating thickness is too large. In this case, one may not assume that coating thickness is a measure of the flaw size; i.e., an interfacial flaw in such a case will not constitute a single edge notch. Other values of toughness, given in Table IV, are in the range of toughness of alumina.

Conclusions

The effect of the tin dioxide coating on the tensile strength of alumina (PRD-166) fibers was studied by subjecting the fibers to single fiber tensile testing. The as-received alumina fibers showed a Weibull mean tensile strength of 1375 MPa, while alumina fibers coated with SnO_2 exhibited a decreasing tensile strength with increasing coating thickness. The loss in the strength of tin dioxide coated (PRD-166) alumina fibers is attributed to two causes i) the exposure of the fibers to high temperature during deposition process and ii) due to the thermal stresses generated during the deposition of tin dioxide.

Acknowledgements

This work was supported by the Office of Naval Research, Contract No. N0014-89-J-1459. We thank the reviewer for his constructive comments.

References

1. K.K. Chawla, Composite Materials: Science and Engineering, p. 134, Springer-Verlag, New York(1987).
2. J. Cook and J.E. Gordon, Proc. Royal Soc. London, A282, 508(1964).
3. J.C. Romine, Ceramic Enginering and Science Proc., American Ceramic Society, Ohio, 8, 755(1987).
4. A. Maheshwari, K.K. Chawla, and T.A. Michalske, Mater. Sci. and Eng., A10, 269(1989).
5. J.L. Keddie and T.A. Michalske, Sandia report SAND 87-1984, UC-25(1988).
6. V.J. Barczak and R.H. Insey, J. Am. Ceram. Soc., 45, 144(1962).
7. L.J. Manfredo and R.N. Mcnally, J. Amer. Ceram Soc., 67, C-155(1984).
8. R.H. Taylor, J. Robertson, S.B. Morris, J. Williamson, and A. Atkinson, J. Mater. Sci., 15, 670(1980).
9. W. Weibull, J. Appl. Mech., 18, 293(1951).
10. B. Bergman, J. Mater. Sci. Letters, 4, 1143(1985).
11. K. Trustrum and A.D. Jayatilaka, J. Mater. Sci., 14, 1080(1979).
12. J.D. Sullivan and P.H. Lauzon, J. Mater. Sci. Letters, 5, 1245(1986).
13. B. Bergman, J. Mater. Sci. Letters, 3, 689(1984).
14. D.J. Pysher, K.C. Goretta, R.S. Hodder, and R.E. Tressler, J. Am. Ceram. Soc., 72, 284(1989).
15. H. Poritsky, Physics, 5, 406(1934).
16. A.W. Hull and E.E. Burger, Physics, 5, 384(1934).
17. K.M. Merz, W.R. Brown, and H.P. Kirchner, J. Am. Ceram. Soc., 45, 531(1962).
18. J. Quirk and C.G. Harman, J. Am. Ceram. Soc., 37, 24(1954).

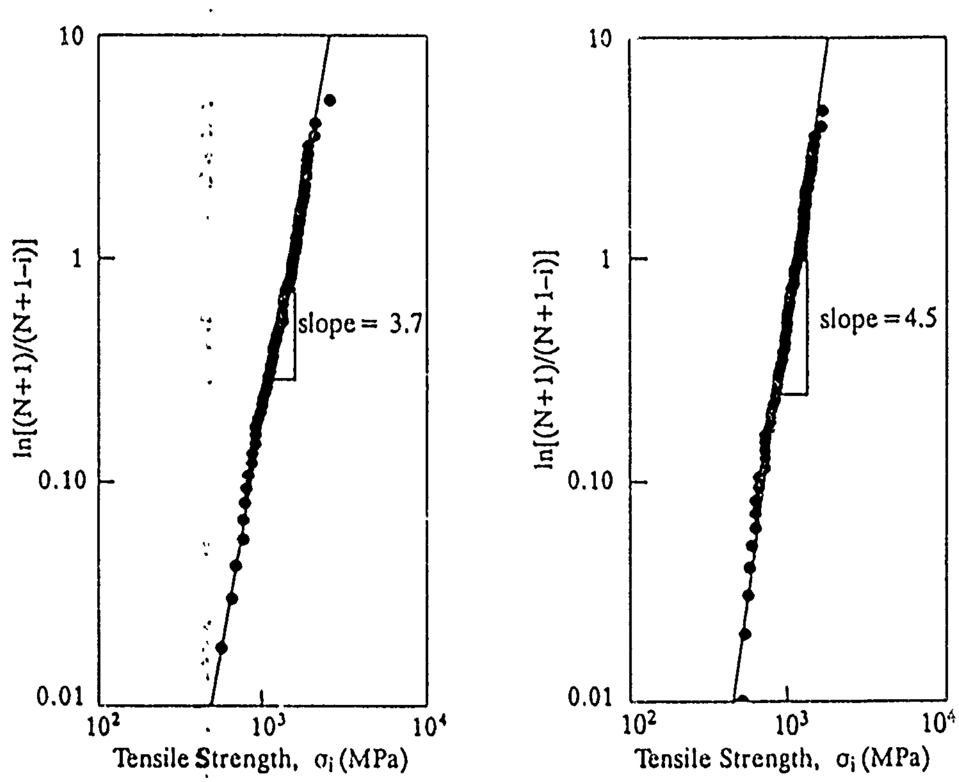

Fig. 1. Weibull plot for a) as-received and b) SnO_2 coated alumina (PRD-166) fibers.

Table I. Weibull Parameters of As-received and Tin dioxide coated Alumina Fibers

Fiber condition	α, MPa	β	Weibull Mean Strength, $\bar{\sigma}$, MPa	Standard Deviation, s, MPa	Coeff. of Variation, %	Correlation Coeff, r^2
As-received	$.21 \times 10^{-11}$	3.7	1375	418	30	0.99
SnO_2 Coated (0.4 μm thick)	$.12 \times 10^{-13}$	4.5	1060	265	25	0.98
SnO_2 Coated (0.5 μm thick)	$.98 \times 10^{-12}$	4.0	966	273	28	0.95
SnO_2 Coated (0.8 μm thick)	$.49 \times 10^{-11}$	3.8	851	279	33	0.99
SnO_2 Coated (2.0 μm thick)	$.45 \times 10^{-11}$	3.9	702	227	32	0.96
SnO_2 Coated (10 μm thick)	$.58 \times 10^{-7}$	3.2	166	56	34	0.96

Table II. Effect of Temperature on the Tensile Strength of Alumina Fiber.

Fiber	α, MPa	β	Mean Strength, $\bar{\sigma}$, MPa	Standard Deviation, s MPa	Coefficient of Variation, %
As - Received	$.21879 \times 10^{-11}$	3.66279	1375.7	417.9	30.3
Exposed at 500 °C for 90 Minutes	$.10241 \times 10^{-11}$	3.79126	1313.6	386.8	29.4
Exposed at 600 °C for 90 Minutes	$.77594 \times 10^{-10}$	3.20340	1283.0	439.6	34.2
Exposed at 900 °C for 90 Minutes	$.23288 \times 10^{-11}$	3.77834	1083.3	319.9	29.5

Table III. Thermo-Mechanical Properties of PRD -166 and SnO_2 *

	Elastic Modulus, GPa	Thermal Expansion Coefficient $10^{-6}\ K^{-1}$
PRD - 166	380 (3)	9.0 (3)
SnO_2	233 (17)	5.3 (18)

* The source of the data is given in parenthesis.

Table IV. Fracture Toughness of Coated Fibers (as given by $K_{IC} = 1.12\ \sigma\ (\Pi a)^{1/2}$).

Coating Thickness a, µm	Tensile Mean Strength $\bar{\sigma}$, MPa	Fracture Toughness MPa $m^{1/2}$
0.4	1060	1.33
0.5	966	1.35
0.8	851	1.51
2.0	702	1.97

Fig. 2. Fracture surface of alumina(PRD-166) fiber showing flaw-induced during processing. SEM.

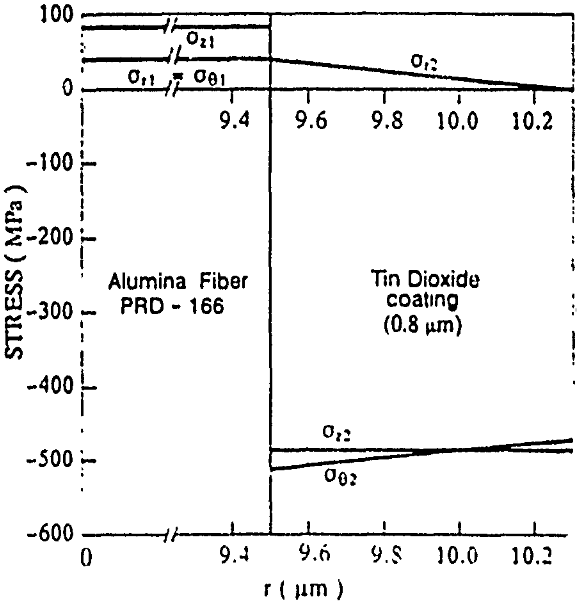

Fig. 3 Thermal Stress Distribution in Tin Dioxide Coated PRD-166 Fiber.

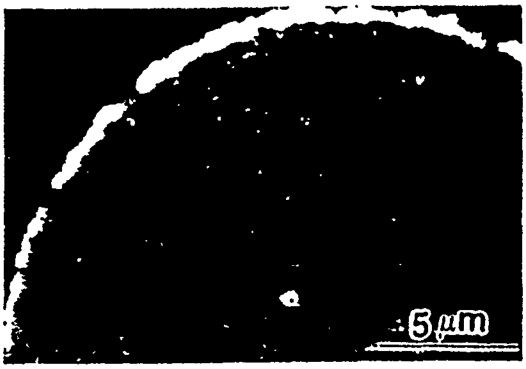

Fig. 4. Tin dioxide coated alumina (PRD-166) fiber showing notches in the coating. SEM

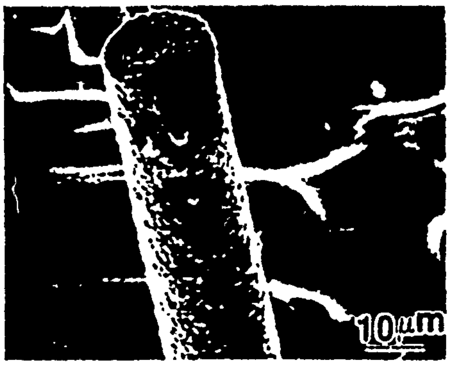

Fig. 5. Fracture surface of tin dioxide coated alumina (PRD-166) fiber showing partial peeling of the coating. SEM.

Appendix B : Role of the SnO_2 Interphase in an Alumina/Glass Composite : A Fractographic Study.

NAL OF MATERIALS SCIENCE 26 (1991) 2743–2749

The role of the SnO$_2$ interphase in an alumina/glass composite: a fractographic study

M. H. SIADATI, K. K. CHAWLA
Department of Materials and Metallurgical Engineering, New Mexico Institute of Mining and Technology, Socorro, NM 87801, USA

M. FERBER
High Temperature Materials Laboratory, Oak Ridge National Laboratories, Oak Ridge, TN 37831, USA

The role of tin dioxide (SnO$_2$) interphase for the alumina/glass composite system was investigated using fractography. Alumina (Al$_2$O$_3$) and glass form a strong chemical bond which is undesirable for toughness in a ceramic matrix composite. SnO$_2$ interphase was incorporated to prevent this strong bond between alumina and glass. SnO$_2$ was deposited on Al$_2$O$_3$ substrates via chemical vapour deposition and bonded with glass. The role of the interphase was then studied by characterizing the fracture surfaces of the bend test and special composite disc samples loaded in diametral compression. Bend tests results showed that the SnO$_2$ interphase and/or the SnO$_2$/Al$_2$O$_3$ interface acted as a plane of weakness. Secondary cracking at 90° to the major crack direction was observed along this plane of weakness, which appears to be in accord with the Cook and Gordon model. Crack deflection and secondary cracking were also observed in the SnO$_2$ region of the compression samples. These results indicate the suitability of SnO$_2$ interphase for the alumina/glass composite system.

1. Introduction

The high thermal stability and elastic modulus of ceramic materials coupled with their low density and corrosion resistance make them very attractive for high-temperature applications [1]. Ceramic materials, however, lack toughness. Currently, a considerable amount of research is being directed at improving their toughness. One of the major efforts in this regard has been devoted to fibre-reinforced composites, particularly those reinforced with carbon, SiC, and alumina fibres [2]. Carbon fibre-reinforced glass matrix composites [3] have shown a wide range of attributes which include high strength, high stiffness, excellent toughness, and low density. SiC fibre-reinforced glasses and glass-ceramics have also shown a good combination of strength and toughness [2]. The toughness improvement in both carbon [4] and SiC [2, 5] fibre-reinforced composites has been attributed to the weak bonding between the fibre and matrix leading to fibre pullout before fracture. Studies of thermal stability of these composites have shown oxidation of carbon fibres in air [6] and gradual strength degradation of the SiC fibre in almost any environment when exposed to temperature as high as 1200 °C or more [7]. Thus, it would appear that the application of ceramic composites reinforced with either carbon or SiC fibres is [illegible] as far as high-temperature use is concerned.

Alumina fibre-reinforced glass was shown to be unaffected by exposure to temperatures up to 1000 °C; however, the overall levels of toughness and strength obtained were less than those achieved through the use of carbon fibre-reinforcement [2]. The low toughness and strength mainly result from the dissolution of alumina fibres into the glass matrix producing a very strong chemical bonding between the two components [8–10]. An approach to overcome this problem involves interface engineering. The basic idea is to incorporate an interphase layer between fibre and matrix that would act as a diffusion barrier between the two components and limit the interface bond strength so that debonding can occur during passage of a crack. Bender *et al.* [11] showed the effect of fibre coating on the toughness improvement of silicon carbide fibre-reinforced zirconia composite. The thin boron nitride (BN) coating used in their investigation (1–2 μm thick) prevented any dissolution of fibre into the matrix. Other investigators employed BN coating on silicon carbide fibre in various matrices [12, 13] and obtained lower interfacial shear stress which resulted in a more extensive fibre pullout during the composite fracture. For alumina/glass composite, Maheshwari *et al.* [10] studied the effect of SnO$_2$ coating. The Al$_2$O$_3$–SnO$_2$ phase diagram predicts no mutual solid solubility at temperatures as high as

2461/91 $03.00 + .12

1620 °C [14]. Maheshwari *et al.* obtained elemental concentrations at intervals of 2 μm across the two interfaces. They investigated diffusion of Sn, Si, and Al across the Al_2O_3/SnO_2 and SnO_2/glass interfaces using electron microprobe. Diffusion profiles for Sn, Si and Al showed, as expected, little evidence of diffusion across the alumina/SnO_2 interface at high temperatures. However, small amounts of Sn, Si, and Al diffused across the SnO_2/glass interface. Therefore, they concluded that the lack of solid solubility of SnO_2 in Al_2O_3 and very low solubility in glass at high temperatures coupled with its refractoriness make SnO_2 an ideal candidate for producing an interphase for the alumina/glass composite system. They also obtained some preliminary results from indentation cracking technique showing the ability of SnO_2 to cause crack deflection at the Al_2O_3/SnO_2 interface. A suitable interphase must provide a weak enough interface/ interphase to allow crack deflection and fibre pullout. If the Al_2O_3/SnO_2 interface and/or the SnO_2 interphase itself are weak enough, then either one of them or both can provide planes of weakness in front of an oncoming crack to cause crack deflection and/or secondary cracking [15]. The objective of this fractographic study was to examine this phenomenon in detail.

2. Materials and experimental procedure

The materials used for this experiment were polycrystalline α-alumina (99.5%) and a borosilicate type glass (N51A). The nominal composition of the glass is given in Table I. Stannic chloride ($SnCl_4$) was used to chemically vapour deposit (CVD) tin dioxide (SnO_2) on to alumina substrates. Table II gives some physical and mechanical properties of tin dioxide along with those of alumina and glass.

TABLE I Nominal composition of N51A glass [17]

	wt %		wt %
SiO_2	72	Si	33.6
B_2O_3	12	B	3.8
Al_2O_3	7	Al	3.7
CaO	1	Ca	0.7
Na_2O	6	Na	4.5
K_2O	2	K	1.7
BaO	< 0.1	Ba	trace
		O_2	balance.

TABLE II Important mechanical and physical properties of alumina, tin dioxide and glass

	Alumina	SnO_2	Glass
E (GPa)	360–400 [18]	233 [19]	72 [17]
VHN (GPa)	1.73 [20]	1.13 [20]	0.63 [20]
K_{Ic} (MPa $m^{1/2}$)	2.6 ± 0.1 [9]	?	0.7-0.8 [9]
ρ (g cm^{-3})	3.9–4.0 [18]	6.95 [21]	2.3 [17]
α (10^{-6} °C^{-1})	7.4 [22]	3.77 [19]	7 [17]
Melting point (°C)	2015–2050 [23]	1630 [21]	-
Annealing point (°C)	-	-	570 [17]
Softening point (°C)	-	-	785 [17]

For bend tests, alumina substrates were surface finished to 600 grit paper. SnO_2 interphase was obtained by CVD at 750 °C for 20 min. Oxygen was used as a carrier gas for both water vapour (0.5 l min^{-1}) and $SnCl_4$ (1 l min^{-1}) in separate reactors and then fed into the ceramic tube reactor where the deposition of SnO_2 took place. By altering the oxygen flow, one could optimize the humidity level of the system to obtain reproducible coatings. SnO_2-coated and uncoated alumina substrates were bonded to glass at 900 °C for 1 h. Fig. 1 shows schematically a coated composite sample. A straight notch was introduced at the centre of the component on the tension side to control the crack initiation. Straight notches were made with a diamond wafer blade to a depth of about 1 mm. Bend tests were conducted in an Instron machine using a crosshead speed of 0.005 cm min^{-1}.

The same procedure was followed to coat Al_2O_3 ring samples and subsequently bond them with the glass, Fig. 2. The resulting composite discs were

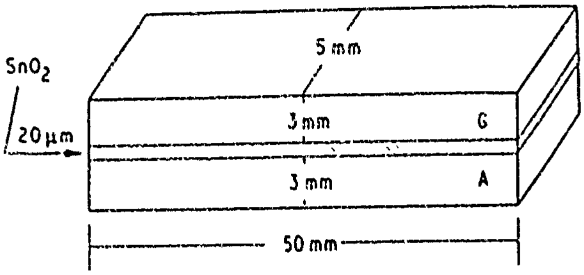

Figure 1 Schematic drawing of a coated composite sample showing the various components. A and G indicate alumina and glass, respectively.

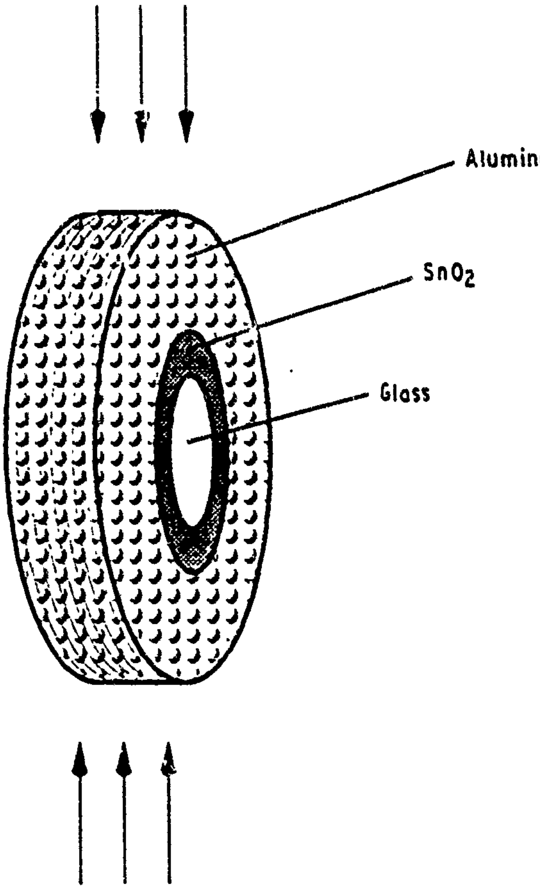

Figure 2 Schematic drawing of a composite disc sample.

loaded in diametral compression [16]. This geometry provides a simple method for obtaining a tensile stress normal to the interface/interphase. The compression tests were interrupted periodically and the composite discs were observed with a metallograph and SEM for any possible cracking or debonding at the interface/interphase. Fracture surfaces were examined by SEM.

3. Results and discussion

3.1. Bend test

Some features of the fracture surfaces of several notched alumina/glass bars broken in bend tests are described below.

Figs 3 and 4 show the relatively flat fracture surfaces of uncoated and coated samples, respectively. Figs 3b and 4b show the interface/interphase regions of Figs 3a and 4a at higher magnification (arrows indicate crack propagation direction). The uncoated sample (Fig. 3) showed a very intact and solid interface. The coated sample, however, showed secondary cracking, e.g. in the region marked by a rectangle in Fig. 4b. At still higher magnification, secondary cracks along the Al_2O_3/SnO_2 interface (Fig. 5a) and in the SnO_2 interphase (Figs 5b and 6) were clearly observable.

Careful observation and comparison of Figs 5 and 6 reveal that the features, in the plane of the picture (the primary crack), on the fracture surface of Fig. 5, are all discontinuous across the secondary crack. That discontinuity indicates that the secondary crack passed through the plane of the micrograph before the primary crack arrived. In Fig. 6, the fracture surface features are continuous. The occurrence of secondary cracks with discontinuous fracture surface features may be explained by considering the state of stress at the crack tip as analysed by Cook and Gordon [15]. Their analysis gives the stress distribution near the crack tip for various applied stress systems, e.g. uniaxial tension or wedge opening. It turns out that the stress distribution near the crack tip is about the same for different stress systems. Along the main crack direction (i.e. x-axis) σ_y is initially very high, but it falls sharply, Fig. 7. However, σ_x increases from zero at the crack tip and at a small distance (roughly equal to one crack tip radius as per Cook and Gordon model) reaches a maximum, the value of which is about one-fifth of the maximum value of σ_y (i.e. $\sigma_{x\,\max} \simeq \frac{1}{5}\,\sigma_{y\,\max}$). As one moves along the x-axis away from the crack tip and past the maximum value of σ_x, the two stresses σ_y and σ_x soon become roughly equal to each other and fall off together roughly as the inverse square root of

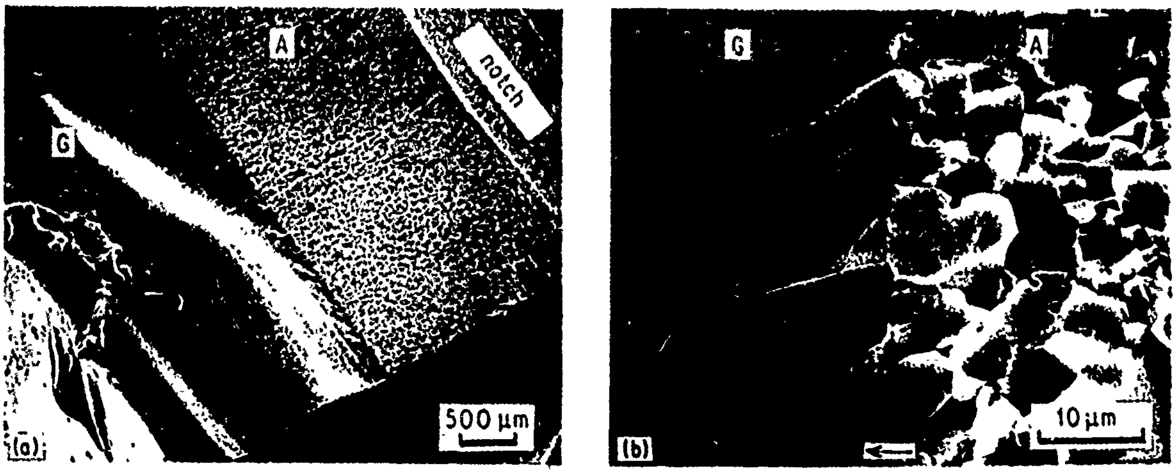

Figure 3 (a) Fracture surface of an uncoated Al_2O_3/glass composite at low magnification. (b) As (a), the arrow indicates the crack propagation direction. Note the integrity of the alumina/glass interface.

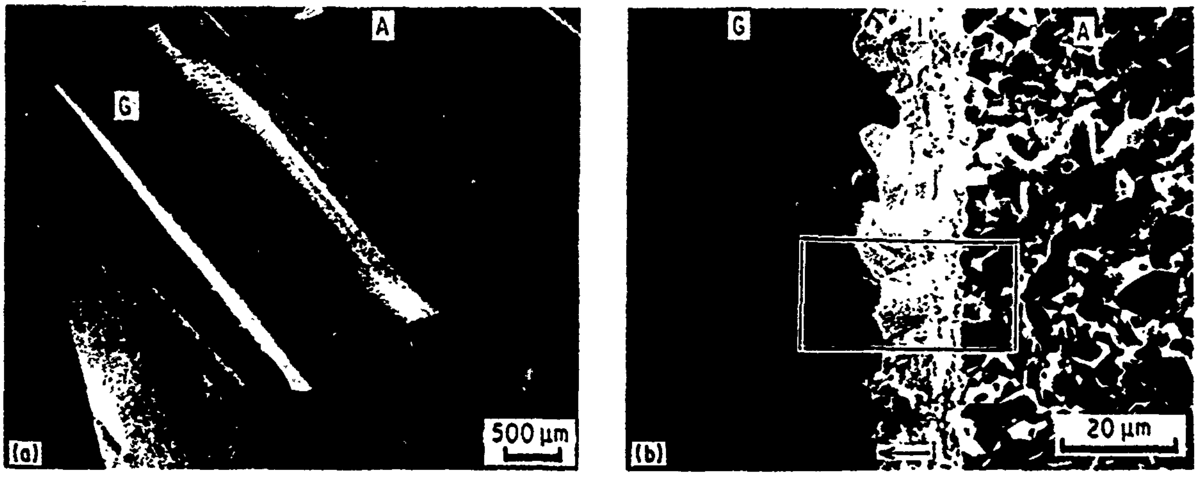

Figure 4 (a) Fracture surface of a coated Al_2O_3/glass composite at low magnification. (b) As (a); the area in the rectangle contains secondary cracks. The arrow indicates the crack propagation direction.

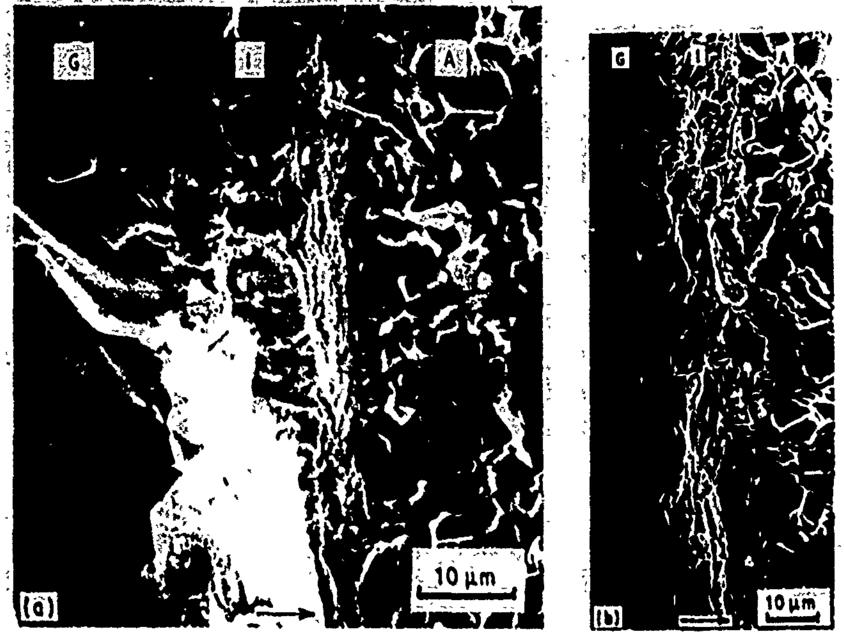

Figure 5 (a) Secondary crack at the SnO_2 Al_2O_3 interface. (b) Secondary crack in the SnO_2 interphase. The fracture surface features are not continuous across the crack.

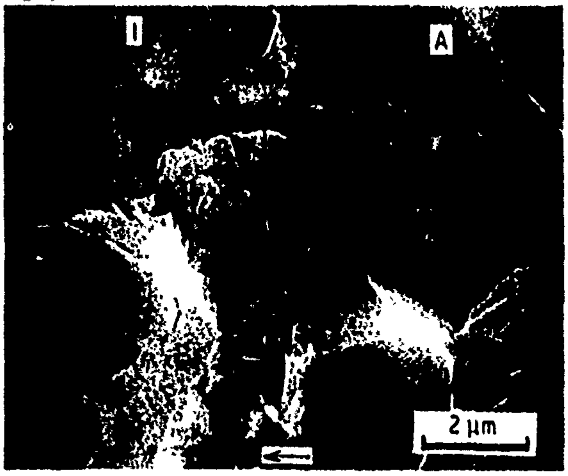

Figure 6 Secondary crack in the SnO_2 interphase near the SnO_2/Al_2O_3 interface. The fracture surface features are continuous across the crack.

the distance from the crack tip. Fig. 8 shows a schematic drawing of a three-point bend laminate composite sample after the application of load. Analogous to the stress analysis of Cook and Gordon [15], a triaxial state of stress prevails at the crack tip under load. σ_y and σ_x are indicated in Fig. 8. σ_z if present (plane strain) will act perpendicular to the plane of the figure. Also shown in Fig. 8 are the secondary cracks as observed in the present work. Fig. 9 shows the long transverse side of a four-point bend sample broken at 500 C. Note the debonding along the Al_2O_3/SnO_2 interface caused by formation of secondary cracking. It would appear that these secondary cracks at Al_2O_3 SnO_2 interface or in SnO_2 would have formed as per the mechanism suggested by Cook and Gordon. This mechanism indicates that if the interface is weak enough, it will crack open some distance ahead of the primary crack forming a secondary crack as shown in Fig. 10.

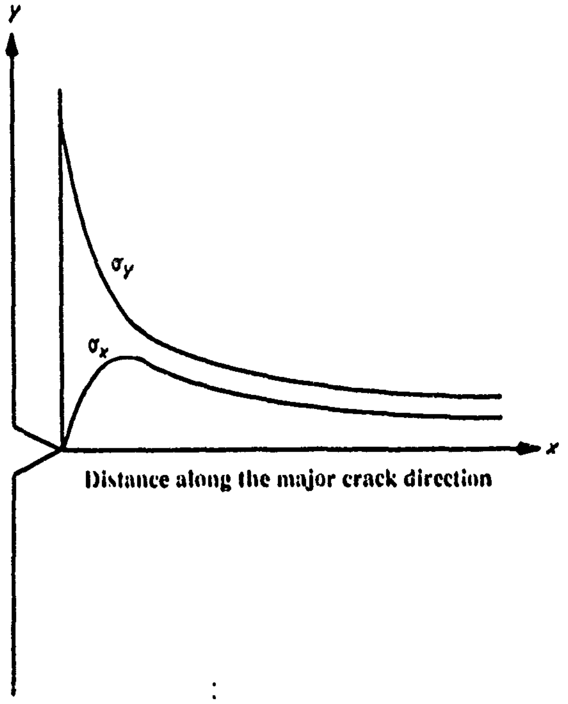

Figure 7 State of stress at a crack tip. Along the x-axis, σ_y, although initially high, falls sharply. However, σ_x increases from zero at the crack tip and, at a distance roughly equal to one crack tip radius, reaches a maximum value which is about one-fifth of the maximum value of σ_y [15].

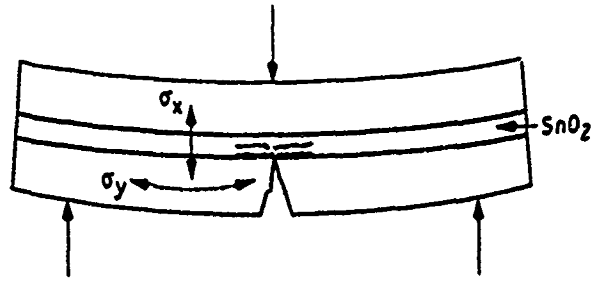

Figure 8 Bend test specimen after the application of load showing secondary cracking in the interphase layer.

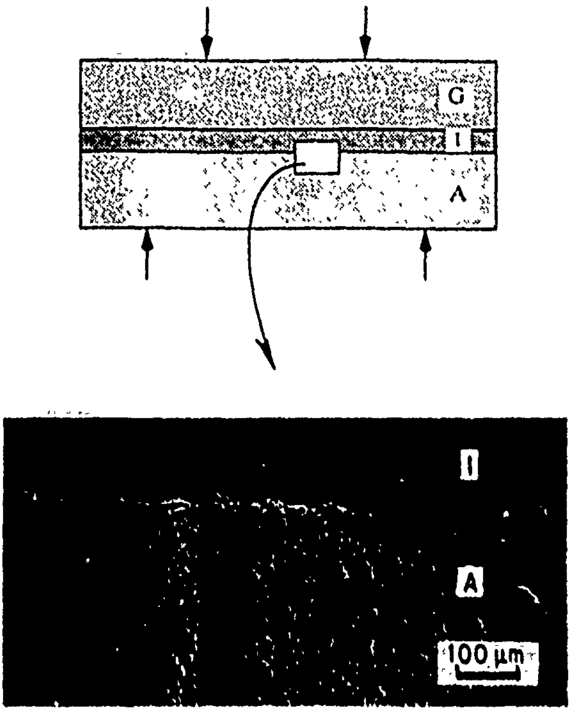

Figure 9 Long transverse view of a four-point bend test specimen after fracture at 500 C. Note the debonding along the Al_2O_3/SnO_2 interface caused by formation of secondary cracking.

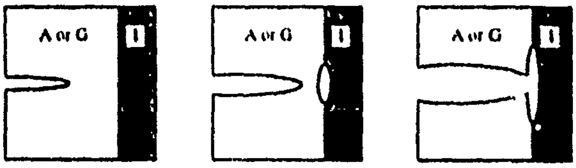

Figure 10 Fracture of the interface some distance ahead of the primary crack [15].

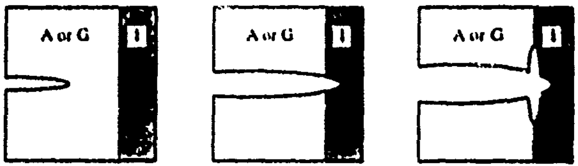

Figure 11 Penetration of the primary crack through the interface which may crack immediately behind the primary crack tip [15].

In cases where there exists a continuity of features on the primary fracture surface across the secondary crack (Fig. 6), Cook and Gordon considered the case of primary crack penetration through the interface which may crack open afterwards. According to this model which is schematically shown in Fig. 11, the interface opens up behind the primary crack tip to yield a cruciform-shaped crack. What is important to emphasize at this point is that this later secondary crack formation also represents an energy-consuming feature of the overall fracture process, and hence a contribution to toughness.

In both cases, the occurrence of secondary cracking or crack deflection provides an energy-dissipating mechanism in the alumina/glass composite system.

3.2. Compression test

The main reason for using this special test was to exploit the difference between the Poisson's ratios of alumina and glass (0.27 and 0.21, respectively). This difference was expected to cause debonding at the alumina/glass interface under compression. This debonding could occur if the transverse elastic stress generated due to the difference in Poisson's ratios was larger than the strength of the alumina/glass interface. Compression tests performed on uncoated samples revealed no debonding at the interface. The absence of debonding along the alumina/glass interface is a good indication that the elastic stress generated due to the difference in Poisson's ratios is smaller than the strength of the alumina/glass interface.

The coated disc sample broke into two halves just as the uncoated one did. Fig. 12 shows schematically a broken half of the coated sample. The fracture surface was observed in the SEM and, not unexpectedly, secondary cracks were observed at various locations within the SnO_2 interphase. Fig. 13 shows one such secondary crack. This crack may have initiated at the alumina/SnO_2 interface, then entered the SnO_2 interphase, extending almost parallel to the interface and

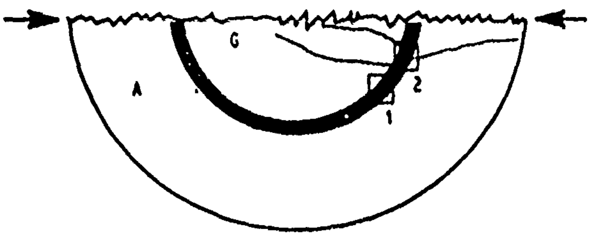

Figure 12 Schematic drawing of a composite disc sample broken under compression. The arrows indicate the compression direction.

Figure 13 Fracture surface of a coated composite disc sample. Arrows show a secondary crack in the SnO_2 region. Note the surface features are continuous.

terminating there. On the face normal to the fracture surface, extensive cracking also occurred at various locations of the SnO_2 interphase. Fig. 14, high magnification view of rectangle 1 in Fig. 12, shows the cracking in the SnO_2 interphase very clearly. The phenomenon of crack deflection at the location marked by rectangle 2 is shown in Fig. 15. Three deflected cracks marked A, B, and C are shown at higher magnification in Fig. 15. The other end of each of the three is portrayed in the schematic drawing in Fig. 12; b and c end in glass and d in alumina. The crack pattern in this figure does have the proper general character of fracture as per the Cook and Gordon mechanism.

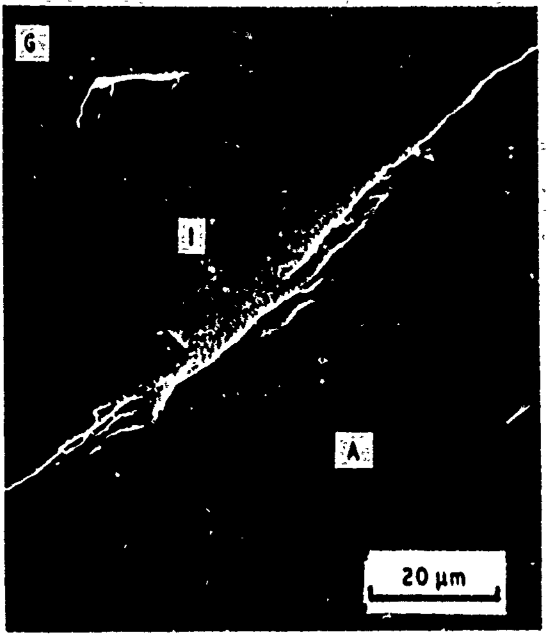

Figure 14 Magnified view of rectangle 1 marked in Fig. 12, illustrating cracking of SnO_2 at this location.

4. Conclusions

From this fractographic study on the role of SnO_2 in alumina/glass composites, we can draw the following conclusions.

1. Observation of secondary cracking at the Al_2O_3/SnO_2 interface and/or within the SnO_2 region on the fracture surfaces of the bend samples confirmed the weakness of both the Al_2O_3/SnO_2 interface and the SnO_2 interphase. This secondary cracking appears to be in accord with the Cook and Gordon model.

2. Crack deflection in the SnO_2 region of the disc-shaped composites, and the absence of such a phenomenon in the uncoated samples, also proved the eventual toughening capability of the SnO_2 interphase.

Acknowledgements

This work was supported by Sandia National Laboratories (contract 05-1773) and Office of Naval Research (contract N00014-89-J-1459). Helpful discussions with Dr E. K. Beauchamp are greatly appreciated. Research was also sponsored in part by the US Department of Energy, Assistant Secretary for Conservation and Renewable Energy, Office of Transportation Systems, as part of the High Temperature

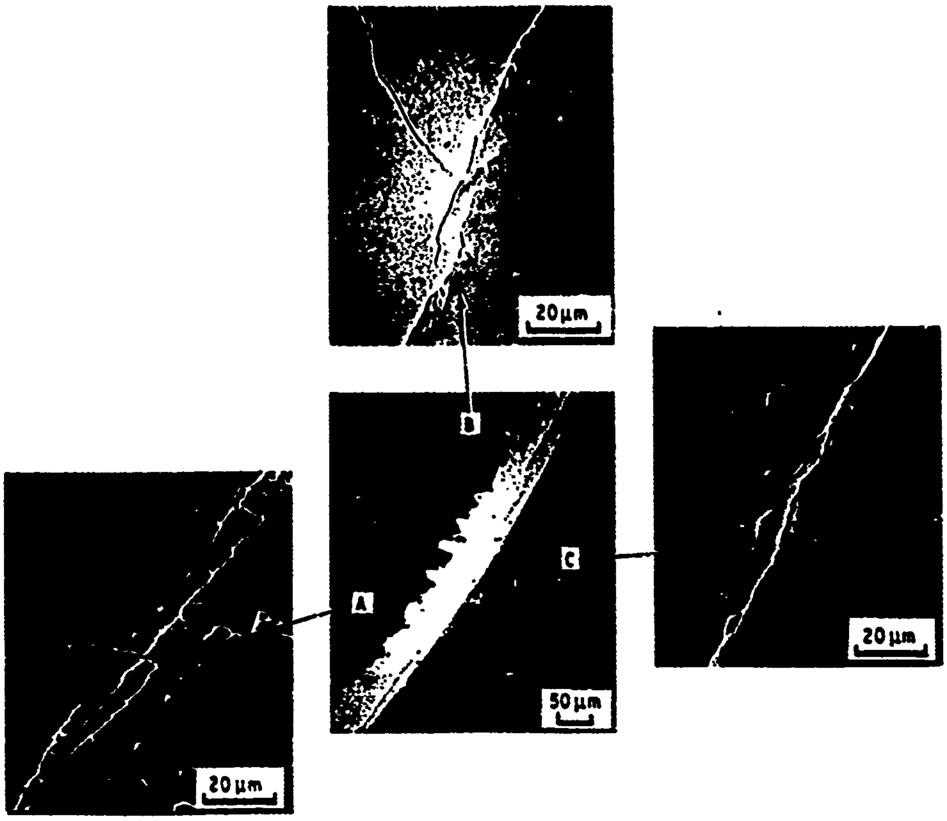

Figure 15 Magnified views of rectangle 2 marked in Fig. 12, showing extensive cracking of SnO_2 together with deflection of three cracks marked A, B, and C. The crack pattern in this figure has the proper general character of fracture as per the Cook and Gordon mechanism.

DE-AC05-840R21400 with Martin Marietta Energy Systems, Inc.

References

1. K. K. CHAWLA, "Composite Materials: Science and Engineering" (Springer-Verlag, New York, 1987) p. 134.
2. K. M. PREWO, J. J. BRENNAN and G. K. LAYDEN, *Ceram. Bull.* 65 (1986) 305.
3. K. M. PREWO and J. F. BACON, "Glass Matrix Composites-I, Graphite Fibre Reinforced Glass", in "Proceedings of the Second International Conference on Composites", edited by B. R. Norton (TMS-AIME, New York, 1974) p. 64.
4. R. LEVITT, *J. Mater. Sci.* 8 (1974) 1847.
5. J. J. BRENNAN and K. M. PREWO, *ibid. J. Mater. Sci.* 17 (1982) 2371.
6. K. M. PREWO and J. A. BATT, *ibid.* 24 (1988) 523.
7. T. MAH, N. L. HECHT, D. E. McCULLUM, J. R. HOENIGMAN, H. M. KIM, A. P. KATZ and H. A. LIPSITT, *ibid.* 19 (1984) 1191.
8. J. L. KEDDIE and T. A. MICHALSKE, "Interface structure and Properties of Alumina/glass ceramic composite", Sandia Report SAND 87-1884, UC-25, January 1988.
9. T. A. MICHALSKE and J. HELLMANN, *J. Amer. Ceram. Soc.* 71 (1988) 725.
10. A. MAHESHWARI, K. K. CHAWLA and T. A. MICHALSKE, *Mater. Sci. Engng* A107 (1989) 269.
11. B. BENDER, D. SHADWELL, C. BULIK, L. INCORVATI and D. LEWIS III, *Amer. Ceram. Soc. Bull.* 65 (1986) 363.
12. M. K. BRUN and R. N. SINGH, *Adv. Ceram. Mater.* 3 (1988) 506.
13. R. N. SINGH, *J. Amer. Ceram. Soc.* 72 (1989) 1764.
14. V. J. BARCZAK and R. H. INSLEY, *ibid.* 45 (1962) 144.
15. J. COOK and J. E. GORDON, *Proc. R. Soc. Lond.* A282 (1964) 508.
16. A. RUDNICK, C. W. MARSHALL, W. H. DUCKWORTH and B. R. EMRICH, "Evaluation and Interpretation of Mechanical Properties of Brittle Materials", Battell Memorial Institute, Columbus, Ohio, Air Force Materials Laboratory Contract AF33(615)-2335, Tech. Report. AFML-TR-67-316, DCIC68-3 (1967) pp. 191.
17. Owens-Illinois Inc, Personal communication (1987).
18. K. K. CHAWLA, "Composite Materials: Science and Engineering" (Springer-Verlag, New York, 1987) p. 77.
19. J. QUIRK and C. G. HARMAN, *J. Amer. Ceram. Soc.* 37 (1954) 24.
20. A. MAHESHWARI, MS thesis, New Mexico Institute of Mining and Technology, Socorro, NM (1988).
21. R. C. WEAST (ed.), "CRC Handbook of Chemistry and Physics", 67th Edn (CRC Press, Boca Raton, FL, 1986) p. B-140.
22. R. N. KLEINER, in "Handbook of Materials Science", edited by C. T. Lynch (CRC Press, Cleveland, OH, 1975) p. 335.
23. I. W. DONALD and P. W. McMILLAN, *J. Mater. Sci.* 11 (1976) 949.

Received 19 April
and accepted 2 August 1990

Appendix C : Characterization of Tin Dioxide Interphase Coating in an Alumina/Glass Composite.

Characterization of Tin Dioxide Interphase Coating in Alumina/Glass Composite

M. H. Siadati and K. K. Chawla
Department of Materials and Metallurgical Engineering, New Mexico Institute of Mining and Technology, Socorro, NM 87801

The purpose of this investigation was to study the microstructure of tin dioxide (SnO_2) coating formed by chemical vapor deposition (CVD) as an interphase between alumina and glass. Different temperatures and times were used to obtain coatings of this material by CVD. Hydrogen iodide (57% concentration) was used to etch the samples. Low temperature (500°C) CVD resulted in a uniform columnar growth, while the high-temperature (750°C) CVD showed an irregular, lateral growth of the SnO_2 grains. At 500°C, a longer CVD time resulted in much more extended columnar growth. Uniformity in thickness and low surface roughness obtained in the SnO_2 deposit at 500°C and 5 min would appear to offer an ideal interphase for the alumina/glass composite system. The effects of the deposition time and temperature on the growth rate of the SnO_2 grains are discussed.

INTRODUCTION

Tin dioxide is a very interesting material. It is an n-type, wide-band gap semiconductor, and a considerable amount of work has been done to characterize it for its electrical and optical properties [1–6]. More recently, however, we have discovered [7, 8] the use of SnO_2 as an interphase in the alumina/glass composite system, i.e., a structural application of tin dioxide. In the field of ceramic matrix composites (CMCs), a considerable amount of research is being focused on interface engineering with the aim of enhancing the toughness of these materials. In the case of the alumina/glass composite system, the idea is to incorporate an SnO_2 thin film as an interphase layer and a diffusion barrier between the two components to inhibit a strong chemical bond between alumina and glass and, thus, achieve higher toughness in the composite system. In this article we wish to report some microstructural observations on SnO_2 in order to improve our understanding of its structure and properties for the alumina/glass composite system.

PROCEDURE

SAMPLE PREPARATION

Materials used for this study were polycrystalline α-alumina (99.5%) from Coors Porcelain Co. and a borosilicate type glass (N51A) from Owens Illinois, Inc. Stannic chloride ($SnCl_4$) was used to chemically vapor deposit tin dioxide (SnO_2) onto alumina and glass substrates. The experimental setup is shown in Fig. 1. Oxygen and nitrogen were used as carrier gases to carry water vapor (0.75 L/min) and $SnCl_4$ (1 L/min)–, respectively, into the ceramic tube where the deposition of SnO_2 on the substrates took place. The nozzle of the

655 Avenue of the Americas, New York, NY 10010

1044-5803/91/$3.50

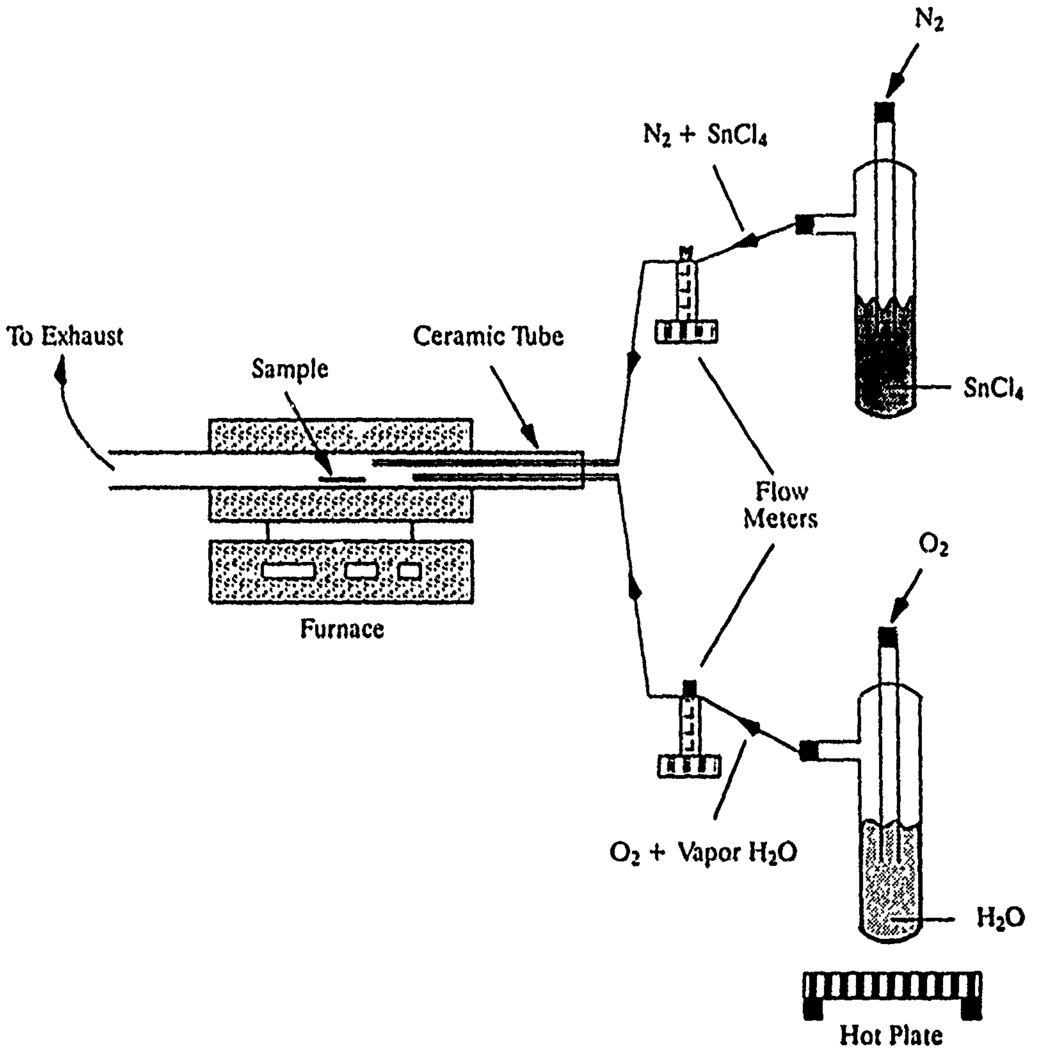

Fig. 1. The experimental setup used to chemically vapor deposit SnO_2.

tube conducting $SnCl_4$ vapor was stationed 2 cm above the substrate, while the other nozzle conducting water vapor was 10 cm away in the horizontal direction. The water for water vapor supply was maintained at 50°C. The SnO_2-coated substrates were then bonded to glass at 900°C for 1 h. Table 1 presents the various parameters of time and temperature used and the thicknesses obtained in the preparation of the three samples 1, 2, and 3.

ETCHING PROCESS

Hydrogen iodide (HI) at 57% concentration was used to etch the polished cross-sectional surfaces of the three samples 1, 2, and 3. The samples were dipped in an HI acid bath maintained at 55–60°C during etching. The samples were then characterized by SEM to obtain the best etching conditions (Table 1).

RESULTS AND DISCUSSION

The SnO_2 coating obtained is a result of the following chemical reaction as demonstrated by Goshtagore [9]:

$$SnCl_4 + 2H_2O \rightarrow SnO_2 + 4HCl,$$

and our x-ray analysis showed that the

Table 1 CVD Parameters Used to Obtain the Samples 1, 2, and 3, and the Etch Time

Sample	*Temperature (°C)*	*Time (min)*	*Thickness (μm)*	*Substrate material*	*Etch time (min)*
1	750	20	5–15	Alumina	15
2	500	5	0.8	Alumina	13
3	500	150	40–45	Glass	15

coatings obtained in this study are truly SnO_2. Ghoshtagore [9] has also elaborated on the mechanism of this reaction. Ruling out the Langmuir–Hinshelwood mechanism of surface reaction by two adjacently absorbed species, he has pointed out that this reaction appears to be a case of Rideal–Eley mechanism where gaseous $SnCl_4$ reacts at the substrate surface with adsorbed H_2O molecules. The SnO_2 coating forms by a nucleation and growth mechanism. The classical nucleation theory gives the critical radius as [10]:

$$r^* = \frac{-2\sigma_{cv}}{\Delta G_v} = \frac{2\sigma_{cv}V}{kT\ln(P/P_e)},$$

where r^* is the critical radius, i.e., only clusters larger than r^* will be stable. The other parameters in this equation are:

σ_{cv} = condensate-vapor interfacial free energy
ΔG_v = Gibbs free-energy difference per unit volume
V = molecular volume
P = supersaturated vapor pressure
P_e = equilibrium pressure
T = temperature
k = Boltzmann's constant

This expression, although for homogeneous nucleation, shows the importance and effect of temperature on nucleation of a CVD product. For a unit volume of the phase of molecular volume V condensed from the supersaturated vapor of pressure P to the equilibrium pressure P_e, increasing the deposition temperature will result in a smaller number of larger-sized stable nuclei. The calculated value of r^* for most cases is of atomic dimensions [10]. The heterogeneous nucleation, which is the case in the present work, can be considered as a geometrically modified case of homogeneous nucleation with regard to r^*. An additional contact angle term enters the expression, but the dependence of r^* on temperature remains the same [11, 12]. Growth is very much temperature dependent too. Although a higher temperature results in a smaller number of stable nuclei, diffusion processes [5] and recrystallization/coalescence [13] are greatly enhanced by high temperatures. The growth rate increases more rapidly with temperature than nucleation rate. At higher temperatures, one gets large grain sizes and the films deposited may also have a patchy appearance [5]. Thus, we see that temperature is the main controlling parameter for nucleation and growth in CVD. This temperature effect on CVD of SnO_2 was investigated in this study. Other parameters such as nozzle-to-substrate distance, carrier gas flow rates, water temperature, etc. were all maintained constant.

There exists a complex plasma process [14] for SnO_2 etching. We were, however, successful in using a simple chemical etching method involving HI acid to etch the SnO_2 coating. The letters A, S, and G in the figures to follow indicate alumina, SnO_2, and glass, respectively. The arrow at the bottom indicates the direction of SnO_2 growth. Figure 2 shows an etched microstructure of sample 1:a 20-min, 750°C CVD coating of SnO_2 on an alumina substrate. The SnO_2 grains are large and irregular, and the grain growth was more lateral than columnar, because of the high deposition temperature. Because the nucleation rate is low at high temperatures, only a few nuclei will be expected. The few

Fig. 2. Etched microstructure of sample 1 (750°C, 20 min). The coating thickness varies between 5 and 15 μm. Note the irregular and lateral growth of SnO_2 grains along with twins in some grains. Some pores at the alumina/SnO_2 interface can also be seen. The arrow at the bottom of the figure indicates the direction of SnO_2 growth.

starting grains of SnO_2 can be observed at the alumina substrate. The fact that pores are observed in this figure may also be attributed to the low nucleation and high growth rate at this high temperature. Another interesting feature shown in this figure is the presence of twins. The twins are mostly incomplete twins of parallel sides. The parallel sides of the twins are likely to be coherent boundaries with an incoherent (or semicoherent) twin boundary joining the parallel faces [15].

Figure 3 shows a higher-magnification picture of an etched microstructure of sample 1 in the vicinity of SnO_2/Al_2O_3 interface. This figure shows more clearly the very small grains that initially grew on the alumina substrate. The growth of a thin film can take place by one of three modes [13]: (1) layer-by-layer, which occurs if either on one extreme the adatoms have little mobility (as in amorphous deposits), or under the extreme conditions of very low supersaturation, single-crystal substrate, and ultrahigh vacuum deposition: (2) Stranski- Kaitchev mode, in which case the film grows just as in the layer-by-layer mode and then converts itself into three-

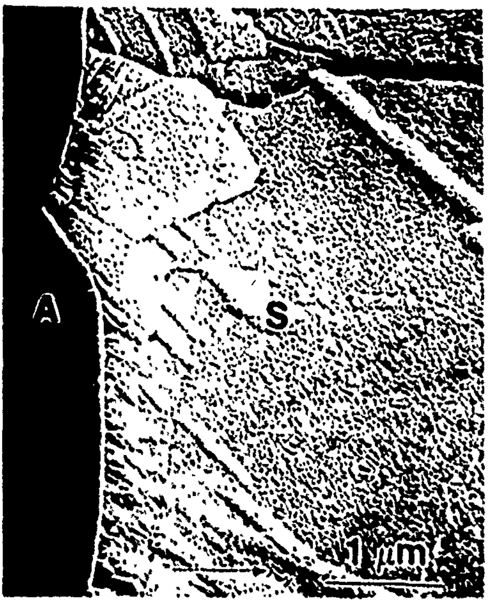

Fig. 3. Etched microstructure of sample 1 (750°C, 20 min). In the vicinity of SnO_2/Al_2O_3 interface, we can observe extremely small grains that formed before excessive growth occurred

Fig. 4. A top view of the multifaceted crystals of SnO_2 on alumina substrate before bonding to glass. Sample 1:750°C, 20 min. The large crystals have resulted in a very rough surface.

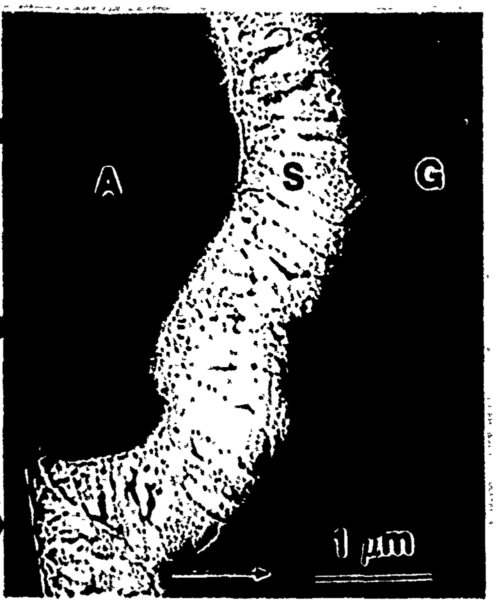

FIG. 5. Etched microstructure of sample 2 (500°C, 5 min). The coating thickness is about 1 μm. SnO_2 grains are very columnar and there are no pores at the SnO_2/Al_2O_3 interface.

dimensional nuclei; and (3) three-dimensional growth of the discrete nuclei. It is apparent from Figs. 2 and 3 that the growth mode in this study is of the third kind.

A top view of the multifaceted crystals of sample 1 is shown in Fig. 4. Note that the alumina substrate is completely covered with the SnO_2 coating. It is important to mention here that a 5-min coating at 750°C did not cover the alumina substrate completely. It is clear from this figure that the surface roughness of sample 1, shown transversely in Fig. 2, is a result of lateral growth and large octahedral grains of SnO_2. This microstructure, consisting of well-developed octahedral crystals, indicates preferential crystal growth along the octahedral faces, and leads to a common occurrence of bicrystals, twins, and stacking faults [6].

Figure 5 shows an etched microstructure of sample 2 (5 min, 500°C), SnO_2 coating on alumina substrate. Note that the alumina substrate surface is very jagged. There are numerous small grains in the vicinity of the alumina substrate and no pores. This is an indication of high nucleation rate. It is clear from Fig. 5 that the submicrometer size grains grew in a very columnar fashion. Figure 6 shows another etched microstructure of sample 2, but at a different location, and slightly over etched to delineate the grain boundaries more clearly. Again, the columnar growth and surface roughness are apparent. This columnar growth is in sharp contrast to the irregular and lateral growth observed in sample 1; compare Fig. 5 with Fig. 2. Another point of contrast is the surface roughness of the SnO_2 coating. The lower temperature used to obtain this sample yielded higher nucleation and lower growth rate (cf. Figs. 2, 5, 6).

The multifaceted crystals of sample 2 as seen from the top are shown in Fig. 7. At higher magnification [Fig. 7(b)], we can see that the crack, produced by indentation, runs in SnO_2 in an *intergranular* manner indicating brittle fracture mode in SnO_2. Note that the alumina substrate is completely covered with the SnO_2 coating. Compare this with the top view of the multifaceted crystals of sample 1, Fig. 4. This surface is much smoother than that of sample 1 (Fig. 7 vs. Fig. 4). It is again emphasized that a lower deposition temperature yielded smaller and, thus, less faceted grains. This temperature effect on surface

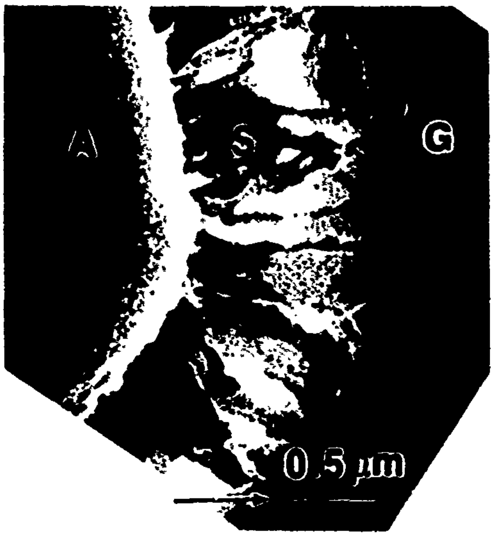

FIG. 6. Same sample (500°C, 5 min) as in Fig. 5 but at a different location. This slightly overetched area clearly shows the columnar nature of the SnO_2 grains.

FIG. 7. A top view of multifaceted crystals of SnO_2 in sample 2 before glass bonding. The crack, produced by indentation, runs in SnO_2 in an intergranular manner. The crystals are small and consequently the surface is less rough than that in sample 1 (see Fig. 4).

roughness can be further confirmed by comparing the etched transverse section of samples 1 and 2 (Fig. 2 vs. Figs. 5 and 6). This phenomenon has also been observed by others [2, 5].

The fracture surface of sample 2 broken in three-point bend test is shown in Fig. 8. Note that the CVD SnO_2 fully covered the fagged alumina substrate. It is also of interest to observe that grains grew in the interior of the hole from both sides until they met face to face. This intergranular fracture surface also shows the columnar nature of the SnO_2 growth. As mentioned earlier, the role of SnO_2 coating in our work is to inhibit a strong chemical bond between alumina and glass components. If the bond between SnO_2 and alumina is weak, debonding may occur between SnO_2 and alumina, which enhances its role as an interphase in this composite system. This debonding between SnO_2 and alumina, which has been reported elsewhere in detail [8], is also shown in Fig. 8 as indicated by an arrow. We also note that the grains grew larger as the CVD proceeded toward completion. Thus, at the SnO_2/glass interface, the SnO_2 grains would be larger than those at the SnO_2/alumina interface. We know that the larger the grains, the weaker is the material [16]. Consequently, although there is some chemical bonding [7] between SnO_2 and glass, the large SnO_2 grains in the vicinity of SnO_2/glass interface may provide a weak layer, which may help further debonding and fiber pullout in a fibrous composite system.

An etched microstructure of sample 3 (150 min, 500°C), coating of SnO_2 on glass substrate, is shown in Fig. 9. Note the rather extensive and elongated growth of the columnar grains of the SnO_2 coating.

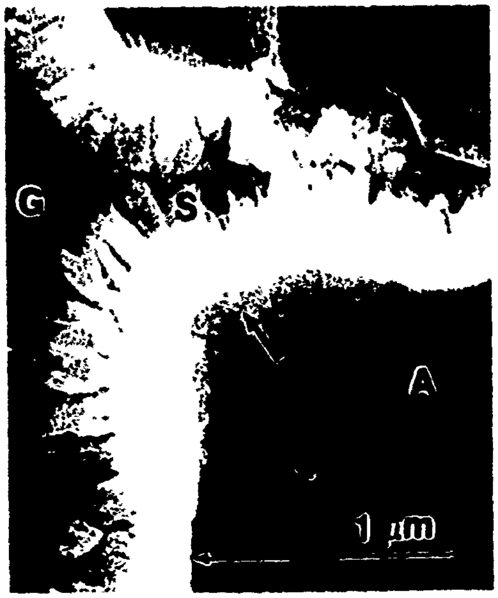

FIG. 8. Fracture surface of sample 2 (500°C, 5 min) broken in a three-point bend test. Columnar nature of the SnO_2 grains is apparent on this SnO_2 fracture surface. Note that although the alumina substrate was very jagged, the SnO_2 coating covered it completely. Arrow indicates the site of debonding between alumina and SnO_2.

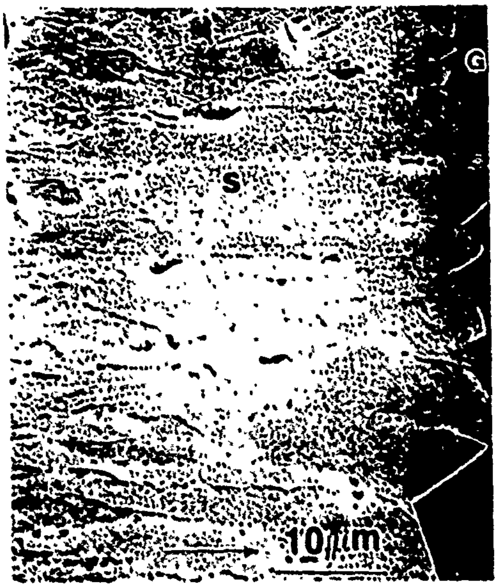

FIG. 9. Etched microstructure of sample 3 (500°C, 150 min). The coating thickness is between 40–45 μm. The columnar SnO_2 grains are extensively elongated.

The coating thickness is 40–45 μm. Figure 10(a) shows a different area of sample 3 while Fig. 10(b), a magnified picture of the box shown in Fig. 10(a), illustrates the small but columnar starting grains onto which large and extensively columnar grains grew. At this point, it is important to mention why two different lengths of time were used to obtain the two samples 2 and 3. Murty et al. [2] have reported that the relation between coating thickness and coating time is linear. Sample 3 is a much thicker coating than sample 2. Therefore, this is as a direct result of much longer length of coating. Although the driving force for nucleation is the same for both samples 2 and 3, the longer length of time in sample 3 caused the larger grain growth. This growth in a direction perpendicular to the substrate takes place in a columnar fashion and is anisotropic with a grain size perpendicular to the substrate determined by the film thickness and by recrystallization/coalescence processes [13].

FIG. 10. Same sample (500°C, 150 min) as in Fig. 9 but at a different location: (a) SEM; (b) Magnified of box in (a). Note the very small grains near the substrate and their columnar growth.

CONCLUSIONS

Based upon the results and discussions given above, we can make the following conclusions:

1. Hydrogen iodide (HI) at 57% concentration was effective in delineating the microstructure of the SnO_2 coating.
2. Higher CVD temperature and/or longer CVD time resulted in higher growth of the SnO_2 grains.
3. Low-temperature CVD resulted uniform columnar growth, while the high-temperature CVD showed an irregular lateral growth of the SnO_2 grains.
4. At a given temperature, longer CVD time resulted in much more extended columnar growth.
5. Uniformity in thickness and low surface roughness obtained at 500°C and 5 min would appear to offer an ideal interphase for the alumina/glass composite system.

This work was supported by Office of Naval Research under contrast #N00014-89-J-1459. Dr. S. G. Fishman was the Project Technical Monitor.

References

1. J. C. Lou, M. S. Lin, J. I. Chyi, and J. H. Shieh, Process study of chemically vapourdeposited $SnO_x(x \sim 2)$ films, *Thin Solid Films* 106:163–173 (1983).
2. N. S. Murty, G. K. Bhagavat, and S. R. Jawalekar, Physical properties of tin oxide films deposited by oxidation of $SnCl_2$, *Thin Solid Films* 92:347–354 (1982).
3. D. Das and R. Banerjee, Properties of electron-beam-evaporated tin oxide films, *Thin Film Solids* 147:321–331 (1987).
4. E. Shanthi, V. Dutta, A. Benerjee, and K. L. Chopra, Electrical and optical properties of undoped and antimony-doped tin oxide films, *J. Appl. Phys.* 51:6243–6251 (1981).
5. G. N. Advani, A. G. Jordan, C. H. P. Lupis, and R. L. Longini, A thermodynamic analysis of the deposition of SnO_2 thin film from the vapor phase, *Thin Solid Films* 62:361–368 (1979).
6. A. Mani, N. Karuppiah, and R. Mahalingam, Microstructure of CVD-SnO_2 films, *Mat. Res. Bull.* 25:799–806 (1990).
7. A. Maheshwari, K. K. Chawla, and T. A. Michalske, Behavior of interface in alumina/glass composite, *Mater. Sci. Eng.* A107:269–176 (1989).
8. M. H. Siadati, K. K. Chawla, and M. Ferber, The role of SnO_2 interphase in an alumina/glass composite: A fractographic study, *J. Mat. Sci.* 26:2743–2749 (1991).
9. R. N. Ghoshtagore, Mechanism of CVD thin film SnO_2 formation, *J. Electrochem. Soc.* 125:110–117 (1978).
10. K. L. Chopra, *Thin Film Phenomena*, McGraw-Hill, New York (1969), p. 143.
11. J. P. Hirth and G. M. Pound, Condensation and Evaporation, *Prog. Mater. Sci.* 11:41–43 (1963).
12. L. E. Murr, *Interfacial Phenomena in Metals and Alloys*, Addison-Wesley, Reading, MA (1975), pp. 276–280.
13. K. L. Chopra and S. R. Das, *Thin Film Solar Cells*, Plenum Press, New York (1983), p. 9.
14. J. Hynecek, Process for etching tin oxide, U. S. Patent 4,750,980 (1988).
15. M. A. Meyers and K. K. Chawla, *Mechanical Metallurgy, Principles and Applications*, Princeton-Hall, Inc., New Jersey (1984), p. 290.
16. W. D. Kingery, H. K. Bowen, and D. R. Uhlmann, *Introduction to Ceramics*, 2nd ed., John Wiley & Sons, New York (1976), p. 794.

Received December 1990; accepted March 1991.

Appendix D : Effect of Interfacial Roughness and Thermal Stresses in Alumina/Glass and Alumina/Tin Dioxide/Glass Composites.

EFFECT OF INTERFACIAL ROUGHNESS AND THERMAL STRESSES IN ALUMINA/GLASS AND ALUMINA/TIN DIOXIDE/GLASS COMPOSITES

K.K. Chawla[1], M.K. Ferber[2], and R. Venkatesh[1]

ABSTRACT

Effects of fiber/matrix processing induced thermal stresses and interface roughness in PRD-166 (alumina-zirconia) fiber/glass matrix and PRD-166 (alumina-zirconia) fiber/tin dioxide/glass matrix composites were evaluated. Thermal stress analysis showed radial tensile stress components at the fiber/coating and coating/matrix interfaces. A study of indentation cracks showed that the interfacial radial tensile stress combined with the weak mechanical bonding between alumina and tin dioxide provided conditions propitious for crack deflection, a desirable feature from a toughness point of view. However, in a nanoindenter pushout test, the tin dioxide coated PRD-166 fiber in the glass matrix did not slide up to a load of 110 mN. This was attributed to the fiber surface roughness induced compressive radial stress which was an order of magnitude larger than the thermal tensile radial stress.

[1] Department of Materials & Met. Eng., New Mexico Tech, Socorro, NM 87801
[2] High Temperature Materials Lab., Oak Ridge National Lab., Oak Ridge, TN 37830

distribution in a two-element and in a three-element cylindrical composite and then show the beneficial effect of the tin dioxide coating in the alumina/glass system.

EXPERIMENTAL PROCEDURE AND MATERIALS

The tin dioxide coating was produced by chemical vapor deposition, by reacting $SnCl_4$ with water vapor at 500°C for 5 min. The details of the coating process as well as the coating microstructure are given in ref. 5. The composites with coated and uncoated alumina fibers in a glass matrix were fabricated by a slurry impregnation method (6). Fiber tows were infiltrated with the glass frit by passing them through a glass slurry containing an organic binder and laid out on mylar sheets to make prepreg tapes. The unidirectional prepreg tapes were cut, stacked, and subjected to binder burnout at 500°C, followed by hot pressing in a graphite lined die in an argon atmosphere at 925°C and 3 MPa pressure.

The chemical compositions of the glass matrix and the the PRD-166 fiber are given in Table 1. The mean diameter of PRD-166 fiber was 19 µm while the thickness of the tin dioxide coating was 1 µm. The fiber volume fraction was about 20%. The relevant thermomechanical parameters for thermal stress evaluation in these unidriectional composites are given in Table 2 (7-9).

Cracks were produced by means of a Vickers indenter (load = 12 N) and their interaction with the fiber was observed by means of optical and scanning electron microscopes.

shows the basic fiber/matrix unit consisting of a central fiber (radius, a) surrounded by its sleeve of matrix (radius, b). The matrix radius, b, will depend on the volume fraction of the matrix. Figure 3b shows the three-element unit consisting of the central fiber surrounded by two concentric sleeves of the coating and the matrix material. Such a simple axi-symmetric model can be used to estimate the three dimensional state of thermal stress up to a moderate fiber volume fraction. The limit of fiber volume fraction depends on when the stresses from one unit composite shown in Fig. 3 start to overlap with the stresses emanating from other such units. Hsueh (11) has used a three cylinder model for very low (< 5%) fiber volume fractions. If we assume that the stress fields of various units do not overlap as long as the interfiber spacing is more than one fiber diameter, then the following thermal analysis will be valid for fiber volume percent between 20 and 25 (12).

The axial symmetry means that we can treat the problem in terms of the principal stresses that are independent of θ. We shall derive expressions for a three-element cylindrical composite. The two-element, uncoated fiber composite will then be a special case, wherein the coating is the same material as the matrix. For the axi-symmetric case under consideration, the radial and circumferential stresses will have expressions of the following form (13-15):

not support a normal stress. Using this boundary condition, we can write

$$at\ r = c \qquad \sigma_{mr} = 0 = A_m - \frac{B_m}{c^2}$$

$$A_m = \frac{B_m}{c^2}$$

$$\sigma_{m\theta} = B_m\left[\frac{1}{c^2} + \frac{1}{r^2}\right] \qquad \sigma_{mr} = B_m\left[\frac{1}{c^2} - \frac{1}{r^2}\right]$$

$$\sigma_{m\theta} = \left[A_m + \frac{A_m}{r^2}c^2\right]$$

$$\sigma_{m\theta} = A_m\left[1 + \frac{c^2}{r^2}\right]$$

Additional relationships between A_i and B_i parameters can be obtained by applying the interfacial boundary conditions.

At r = a, the stress continuity at the interface requires that

$$\sigma_{ir} = \sigma_{(i+1)r}$$

This gives

$$A_f = A_c - \frac{B_c}{a^2}$$

$$(\alpha_m-\alpha_c)\,\Delta T = \frac{A_c+B_c/b^2}{E_c} - \frac{\nu_c}{E_c}(A_c-B_c/b^2) - \frac{B_m}{E_m}\left[\frac{c^2+b^2}{c^2b^2}\right]$$

$$- \frac{\nu_c}{E_c}\sigma_{cz} + \frac{\sigma_{mz}\nu_m}{E_m} + \frac{\nu_m}{E_m}\left[-B_m\left(\frac{c^2-b^2}{c^2b^2}\right)\right]$$

$$= \frac{A_c+B_c/b^2}{E_c} - (A_c-B_c/b^2)\left[\frac{\nu_c}{E_c} - \frac{b^2c^2}{c^2-b^2}\left[\frac{c^2+b^2}{c^2b^2}\frac{1}{E_m} + \frac{\nu_m}{E_m}\frac{(c^2-b^2)}{(c^2b^2)}\right]\right]$$

$$- \frac{\nu_c}{E_c}\sigma_{cz} + \frac{\sigma_{mz}\nu_m}{E_m}$$

and for the axial strain, we obtain

$$\frac{1}{E_c}[\sigma_{cz}-\nu_c 2A_c] + \alpha_c\Delta T = \frac{1}{E_m}\left[\sigma_{mz}-\nu_m 2\frac{B_m}{c^2}\right] + \alpha_m\Delta T$$

$$(\alpha_m-\alpha_c)\,\Delta T = \frac{\sigma_{cz}}{E_c} - \frac{\sigma_{mz}}{E_m} - \frac{\nu_c 2A_c}{E_c} - \left(A_c-\frac{B_c}{b^2}\right)\frac{2\nu_m}{E_m}\,\frac{(c^2b^2)}{(c^2-b^2)}$$

We now have the following unknowns:

A_c, B_c, σ_{cz}, σ_{mz}, σ_{fz}

We also note that a force balance in the axial direction gives

$$\sigma_{cz}(b^2-a^2) + \sigma_{fz}a^2 + \sigma_{mz}(c^2-b^2) = 0$$

After combining the equations obtained from the application of the boundary conditions, we can write

$$W_1 = A_cK_1 + B_cK_2 + \sigma_{cz}K_3 + \sigma_{fz}K_4 \qquad 1$$

$$K_7 = \frac{1}{E_c}$$

$$K_8 = -\frac{1}{E_f}$$

$$K_9 = \left[\frac{1}{E_c}(1-\nu_c) + \frac{1}{E_m}\left(\frac{c^2+b^2}{c^2-b^2} + \nu_m\right)\right]$$

$$K_{10} = \frac{1}{b^2}\left[\frac{1}{E_c}(1+\nu_c) - \frac{1}{E_m}\left(\frac{c^2+b^2}{c^2-b^2} + \nu_m\right)\right]$$

$$K_{11} = -\frac{\nu_c}{E_c}$$

$$K_{12} = \frac{\nu_m}{E_m}$$

$$K_{13} = 2\left[-\frac{\nu_c}{E_c} - \frac{\nu_m}{E_m}\left(\frac{b^2}{c^2-b^2}\right)\right]$$

$$K_{14} = \frac{2}{b^3}\left[\frac{\nu_m}{E_m}\left(\frac{b^2}{c^2-b^2}\right)\right]$$

$$K_{15} = \frac{1}{E_c}$$

$$K_{16} = -\frac{1}{E_m}$$

Equations 1 - 4 can be solved for A_c, B_c, σ_{fz}, σ_{mz}, and σ_{cz}. The distribution of the radial, tangential, and axial stresses in alumina (PRD-166) fiber/glass matrix and alumina

166/SnO_2/glass is explained by the overwhelming contribution of the roughness compared to the tensile radial thermal stress at the interface. However, the interfacial roughness effect will not be very significant when we study the interaction of cracks produced by indentation.

the circumference. Such a crack deflection will make an additional contribution to the work of fracture and, hence, to the fracture toughness of the composite.

CONCLUSIONS

An analysis of the processing induced thermal stresses in uncoated PRD-166 (alumina-zirconia) fiber/glass matrix composite and PRD-166 (alumina-zirconia) fiber coated with tin dioxide/glass matrix composite showed radial tensile stress components at the fiber/coating and coating/matrix interfaces. In the strongly bonded alumina/glass composite, crack traveled unimpeded from glass to the fiber. In composites with a tin dioxide barrier coating, the crack was deflected and went along the coating/fiber circumferential interface. It would appear that the combination of interfacial radial tensile stress and a weak mechanical bonding between alumina and tin dioxide provided conditions propitious for crack deflection, a very desirable feature from a toughness point of view. Further improvements in fiber pullout should also be realized by reducing the surface roughness of the fibers.

ACKNOWLEDGMENTS

This work was supported by the Office of Naval Research (contract N00014-89-J-1459), Dr. S.G. Fishman, Program Manager. This research also received support in part by the US Department of Energy, Assistant Secretary for Conservation and Renewable Energy, Office of Transportation Systems, as part of the High temperature Materials User Program, under contract DE-AC05-840R21400 with Martin Marietta Energy Systems, Inc.

FIGURE CAPTIONS

Fig. 1. A longitudinal section of the composite showing the rough nature of the two interfaces, fiber/SnO_2 and SnO_2/glass. SEM.

Fig. 2. A schematic of the interface roughness (periodic) with an amplitude A. f and m denote the fiber and the matrix, respectively.

Fig. 3. (a) A two-element and (b) a three-element composite.

Fig. 4. Distribution of thermal stresses in alumina (PRD-166) fiber/glass matrix and alumina (PRD-166) fiber/SnO_2/glass matrix composites, for a $\Delta T = -450°C$. (a) Radial stresses (b) Tangential stresses (c) Axial stresses.

Fig. 5 (a) An optical micrograph of an indentation crack propagating unimpeded through the PRD-166 fiber/glass interface.

(b) a schematic depiction of Fig. 6a.

Fig. 6 (a) Crack interaction with the interface in the case of a tin dioxide coated fiber, an optical micrograph, and (b) a schematic of Fig. 6a. The arrows indicate the stress acting at the tip of the crack and at the interface. A crack proceeding from the glass matrix toward the PRD-166 fiber is deflected slightly by the presence of a tensile radial stress at a nearby fiber. This is followed by a more drastic deflection at the fiber/tin dioxide interface into a circumferential direction.

Table 1. Nominal composition (wt. %)

N51A Glass *	
SiO_2	72
B_2O_3	12
Al_2O_3	7
CaO	1
Na_2O	6
K_2O	2
BaO	< 0.1
PRD-166 fiber **	
Al_2O_3	80-85
ZrO_2	15-20

* Owens-Illinois Co.

** Du Pont Co.

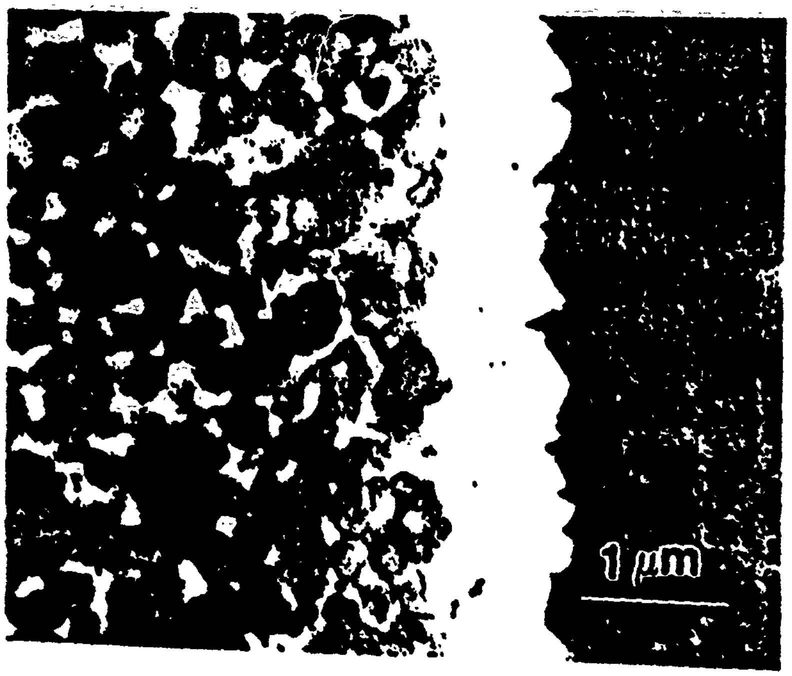

Fig. 1

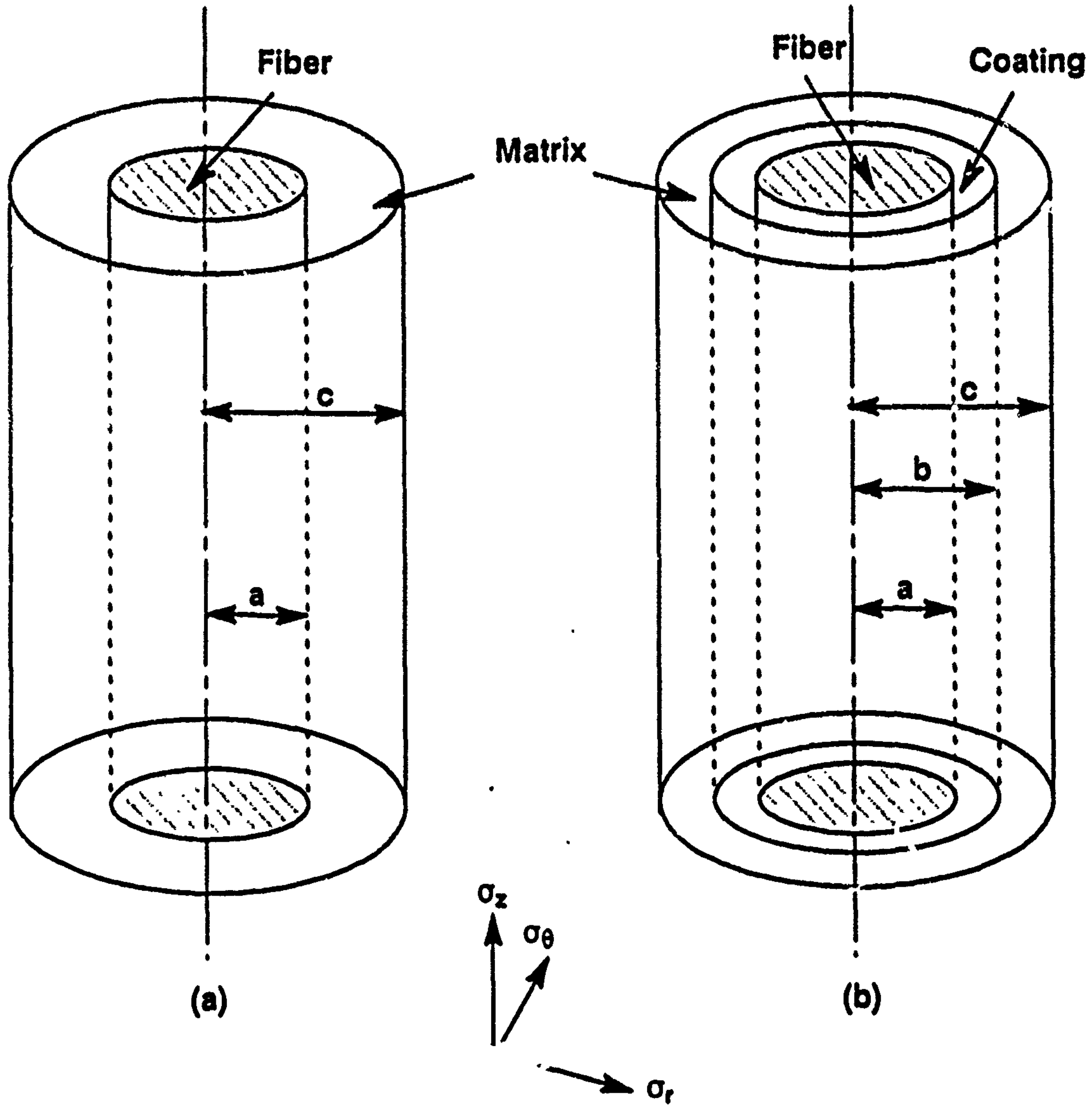
Fiber
Matrix
Fiber
Coating
c
a
c
b
a
σ_z
σ_θ
σ_r

(a)

(b)

Fig 5

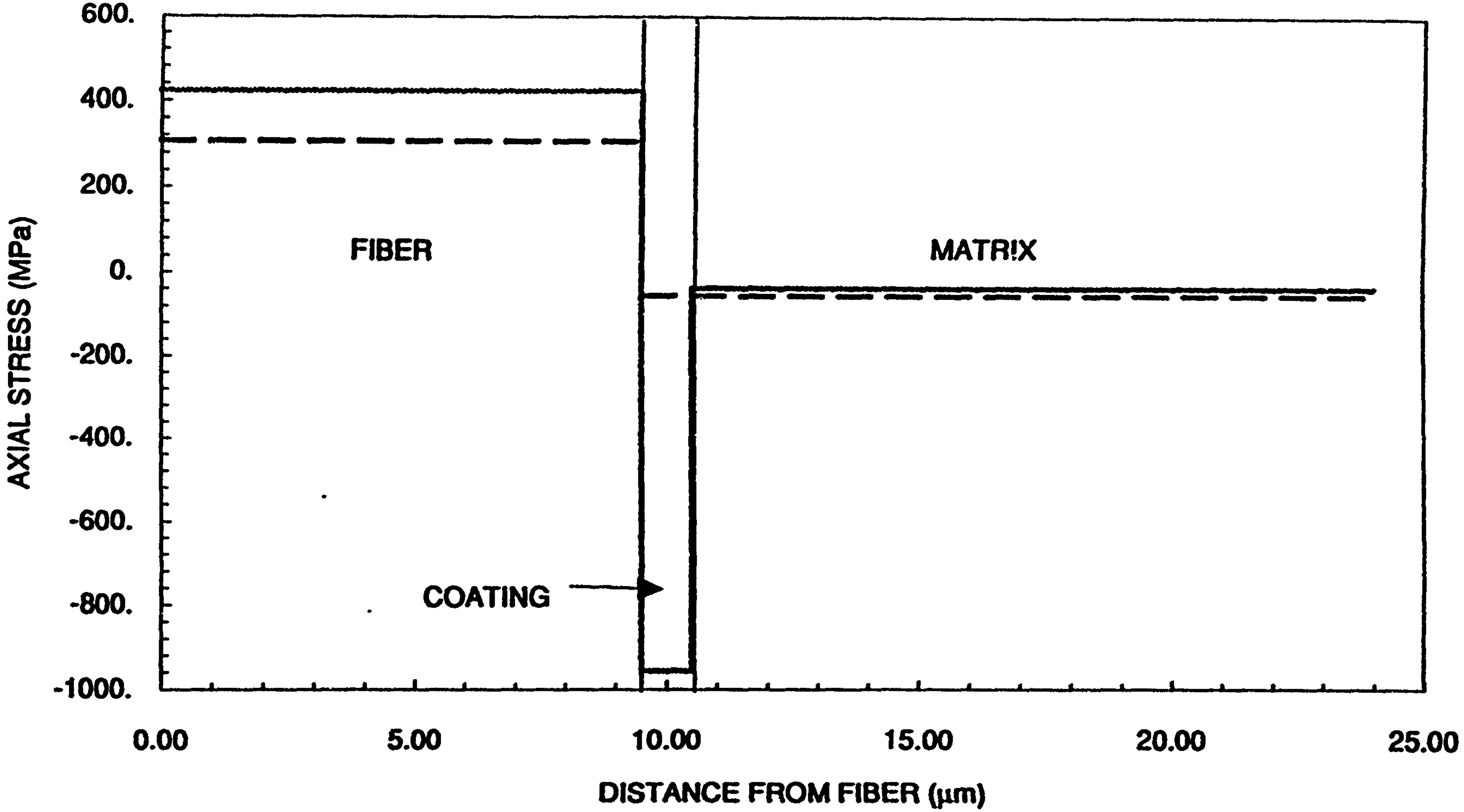
600.
400.
200.
0.
-200.
-400.
-600.
-800.
-1000.
AXIAL STRESS (MPa)
FIBER
MATRIX
COATING
0.00
5.00
10.00
15.00
20.00
25.00
DISTANCE FROM FIBER (µm)

Fig. 4(c)

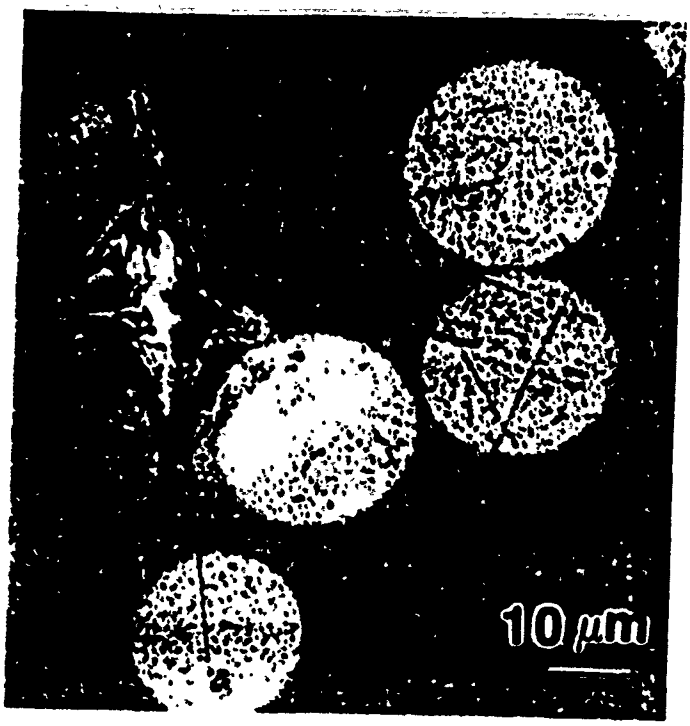
10 µm

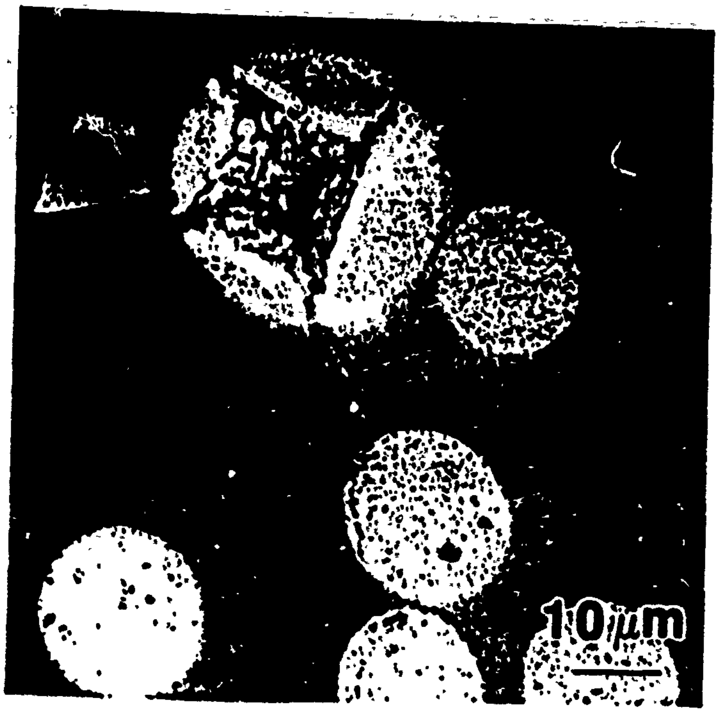
10µm

Appendix E : Effect of Fiber Coating on the Mechanical Properties of a Nextel 480 Fiber Reinforced Glass Matrix Composite.

within 48 hours of receipt: only typographical corrections will be accepted at this stage	Mayfield House 256 Banbury Road Oxford OX2 7DH U.K.	QUERIES	MARKED SET	MSE 5956
		EDITOR	..........PAGES	

Materials Science and Engineering, A151 (1992) 000-000

Effect of fiber coating on the mechanical properties of a Nextel-480-fiber-reinforced glass matrix composite

Rajendra U. Vaidya[a], Joseph Fernando[a], K. K. Chawla[a] and M. K. Ferber[b]

[a]*Department of Materials and Metallurgical Engineering, New Mexico Institute of Mining and Technology, Socorro, NM 87801 (USA)*

[b]*High Temperature Materials Laboratory, Oak Ridge National Laboratories, Oak Ridge, TN 37830 (USA)*

(Received June 10, 1991; in revised form August 19, 1991)

Abstract

The effect of fiber coatings on the mechanical properties of glass matrix composites reinforced with Nextel 480 fiber was investigated. Two different fiber coatings, namely tin dioxide and boron nitride, were investigated. The presence of the coatings on the fiber led to an improvement in mechanical behavior. In particular, the boron nitride coating improved the total work of fracture of the composite without reducing the strength. A marked difference was observed in the fractographic features between the uncoated and tin-dioxide-coated samples as compared to the boron-nitride-coated samples. The uncoated and tin-dioxide-coated fiber composites failed in a brittle fashion, without any fiber pull-out, whereas the boron-nitride-coated fiber samples exhibited extensive fiber pull-out. This improvement in the toughness or energy absorbed during the fracture process was attributed to the relatively weak bonding between the fiber and matrix, induced as a result of the coating.

1. Introduction

Ceramics have a number of advantages over metals and polymers as structural materials. They possess high strength and modulus, and are generally lighter as compared to metallic materials. They also retain their strength to relatively higher temperatures, and are less susceptible to oxidation and corrosion at these temperatures. Their major drawbacks, however, are their lack of ductility and tendency to fail catastrophically. Fiber reinforcement, and in particular ceramic fiber reinforcement of ceramics, offers a potential for significant improvements in strength and toughness. A number of studies have been conducted on incorporating carbon and silicon carbide reinforcements into ceramic matrices [1–8]. These studies indicate that processes such as crack deflection, fiber–matrix debonding and fiber pull-out are necessary, in order to achieve toughening in ceramic matrix composites. These processes are primarily controlled by the nature of the interface between the matrix and reinforcement.

It is known that a relatively strong interface is beneficial for load transfer from the matrix to the fiber, but leads to catastrophic failure in the case of ceramic matrix composites [9]. On the other hand, a relatively weak fiber–matrix interface has been shown to lead to a more "graceful" non-catastrophic failure mode, by promoting processes such as fiber–matrix debonding and pull-out. Hence, the interface more or less controls the mechanical properties of the composite system.

Different methods have been employed for reducing the interfacial strength in ceramic matrix composites. Of all these methods, the use of fiber coatings is the most popular and effective [10–15]. In addition to controlling the fiber–matrix interface, the fiber coating can also protect the fibers from mechanical, chemical and oxidative damage.

The present study is the first successful attempt of incorporation of oxide fibers (Nextel 480) in an oxide (glass) matrix. Nextel 480 is essentially a mullite fiber, and has been shown to exhibit relatively good strength and stability to temperatures as high as 1000 °C [16]. However, the main aim of this study was to investigate the effect of fiber coatings on the mechanical properties and fracture behavior of the composite. Two different fiber coatings, tin dioxide and boron nitride, were employed. Tin dioxide was chosen merely to verify experimentally its ineffectiveness as a coating material in the present case where silica is a major component in the fiber and the matrix. Although tin dioxide seems to work as a diffusion barrier between alumina and glass because of its low solubility in alumina [10], the same cannot be expected in this system because it is soluble to some extent in silica.

Boron nitride finds widespread use in a number of elevated temperature applications, and has also been investigated as a fiber coating [11–15].

2. Experimental procedure

2.1. Materials used

Borosilicate glass, N51A, was used as the matrix material and was obtained from Owens Illinois as a powder. The chemical composition and mechanical and physical properties of the glass matrix used are given in Table 1. The Nextel 480 fibers (coated and uncoated) were obtained from 3M Corporation. Nextel 480 fiber is essentially a mullite fiber having an oval cross-section. The fiber coatings were applied by chemical vapor deposition. Both the tin dioxide (crystalline) and boron nitride (amorphous) coatings had thicknesses of about 0.2 μm. Other details of the coating process are proprietary and were not provided by the manufacturer. The properties of the fiber as supplied by the manufacturer are given in Table 2.

TABLE 1. Properties and composition of the N51A glass matrix

Property	Value
Young's modulus E^{a} (GPa)	72
Vickers hardness^{b} (GPa)	5.5
Fracture toughness K_{Ic}^{b} (MPa m$^{1/2}$)	0.7–0.8
Density ρ^{b} (g cm^{-3})	2.3
Coefficient of thermal expansion^{b,c} (°C^{-1})	5.5×10^{-6}
Softening point^{a} (°C)	785
Chemical composition^{a} (wt.%)	
SiO_2	72
B_2O_3	12
Al_2O_3	7
Na_2O	6
K_2O	2
CaO	1
BaO	<0.1

^{a}Owens Illinois.
^{b}Experimentally determined.
^{c}20–550 °C.

TABLE 2. Properties of the Nextel 480 fiber^{a}

Property	Value
Fiber axes (elliptical)	
Major (μm)	10–13
Minor (μm)	7–9
Young's modulus (GPa)	221
Tensile strength (MPa)	2043
Coefficient of thermal expansion (°C^{-1})	
25–500 °C	4.38×10^{-6}
500–1000 °C	4.99×10^{-6}
Use temperature (°C)	1371
Thickness of the BN and SnO_2 coatings (μm)	0.2
Chemical composition (wt.%)	
Al_2O_3	70
SiO_2	28
B_2O_3	2

^{a}Data of 3M Corporation.

2.2 Specimen fabrication

The composites were fabricated by a slurry impregnation technique (Fig. 1) [17, 18]. The continuous Nextel fiber tows were infiltrated with the glass powder by running them through a glass slurry. The infiltrated fibers were then cut into 6 cm lengths, and laid out on mylar tapes. The prepreg tapes containing unidirectionally aligned fibers were then heated to 500 °C for binder burn-out. The tapes were cut, stacked and hot pressed in a graphite-lined die in an argon atmosphere at 925 °C and 3 MPa pressure. A plot of the hot pressing schedule used in shown in Fig. 2. The volume fraction of the fibers as determined by using an image analyser was 28% ± 4% in all of the specimens.

2.3. Mechanical testing

Rectangular bars ($4\times0.6\times0.32$ cm^3) for strength and toughness measurements were cut from the unidirectional composites. The surfaces of the specimens were polished, with 0.5 μm alumina powder, to minimize surface flaw effects. Strength measurements were conducted in three-point bending in an Instron machine using a cross-head speed of 0.005 cm min^{-1}, according to ASTM standard C-203/85. A minimum span-to-depth ratio of 8 was maintained in all tests.

Static fracture toughness and fracture energy measurements were made using single-edge-notched beam specimens in three-point bending according to ref. 19. The notches in the samples were cut using a high speed diamond saw. A span-to-depth ratio of 10 was used for all the samples. The test was performed at a cross-head speed of 0.005 cm min^{-1}. The critical stress intensity factor was calculated by using the relationship

$$K_I = Y\sigma a^{1/2} \tag{1}$$

where K_I is the stress intensity factor in mode I, σ is the maximum far-field stress, a is the crack length (depth of the introduced notch), and Y is a geometrical factor given by ref. 19 as

$$Y = 1.96 - 2.75(a/h) + 13.66(a/h)^2 - 23.98(a/h)^3 + 25.22(a/h)^4$$

The critical stress intensity factor K_{Ic} is obtained by using eqn. (1) corresponding to the maximum load. This K_{Ic} has been called the "static fracture toughness"

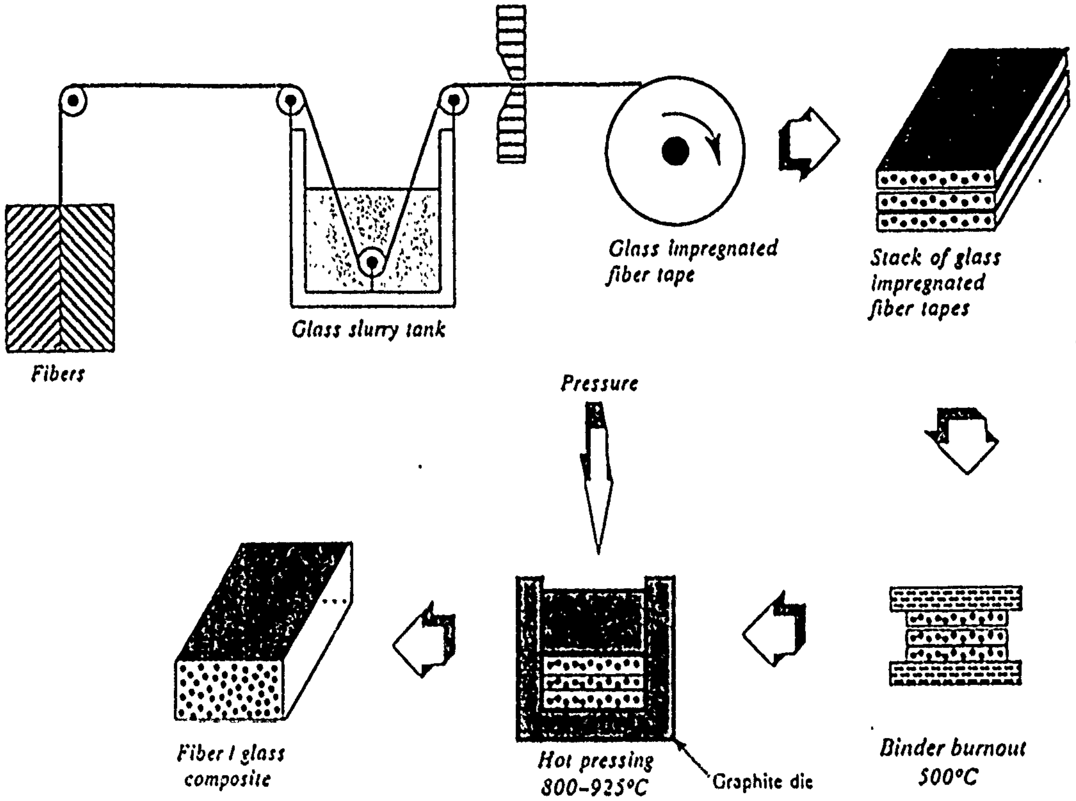

Fig. 1. Schematic of the fabrication process of the glass matrix composites reinforced with coated and uncoated Nextel 480 fiber.

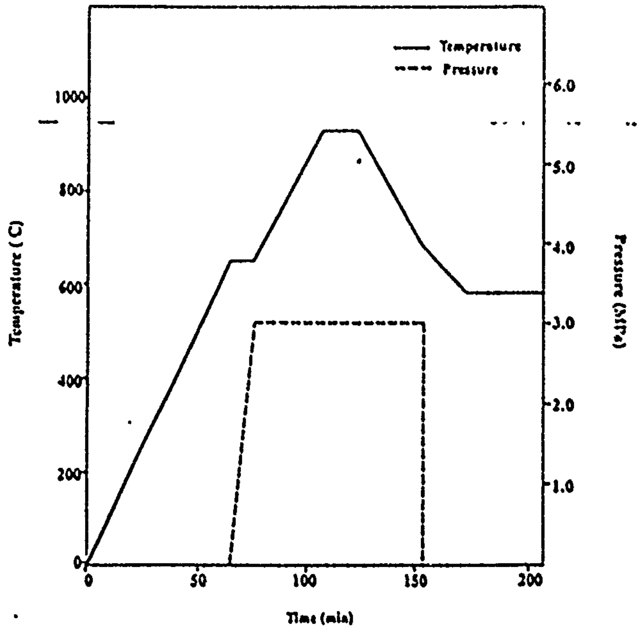

Fig. 2. Hot-pressing schedule for the fabrication of the glass matrix composites reinforced with coated and uncoated Nextel fiber: ——, temperature; – – –, pressure.

or the initiation fracture toughness [20]. The use of this "static toughness formula" was justified because no multiple matrix cracking was observed in any of the composite samples (see Section 3 below).

The fracture surfaces of the samples were coated with an Au–Pd alloy, in order to avoid charging, and examined in a scanning electron microscope (Hitachi S-800 field emission) in the secondary-electron mode.

3. Results and discussion

3.1. Microstructure

Optical and scanning micrographs of a polished cross-section of an as-fabricated composite sample are shown in Fig. 3. The low magnification optical micrograph (Fig. 3(a)) of an uncoated fiber composite is representative of the fiber distribution observed in all of the specimens. Note the excellent consolidation as well as a fairly uniform distribution of fibers. The maximum porosity, detected by an image analyser, in all of the samples was 6%. The scanning micrograph in Fig. 3(b) shows the cross-section of a boron-nitride-coated fiber–glass matrix composite. The thin boron nitride layer does not give any contrast in the scanning electron microscope. The delineation observed around the fibers was obtained by chemical etching in 3% HF, which allowed the fibers to be observed clearly. An electron microprobe analysis was ineffective because the fiber, the coating and the matrix all contain boron. The presence and effect of the boron nitride coating will be evaluated indirectly in the next section.

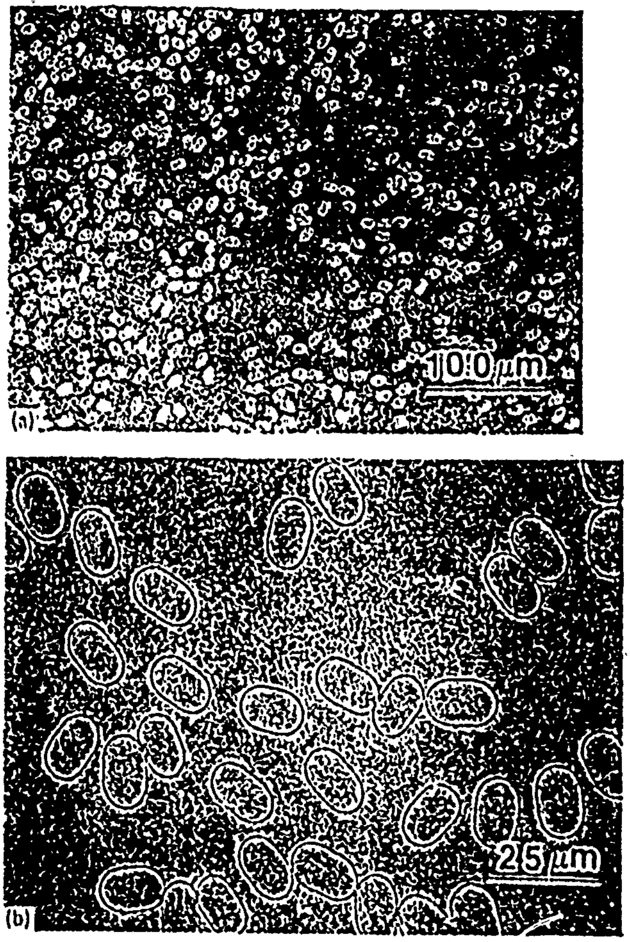

Fig. 3. (a) Optical micrograph of an uncoated fiber composite illustrating the uniform distribution of fibers and low porosity in the matrix. (b) Scanning electron micrograph of a boron-nitride-coated sample also illustrating the fiber distribution.

TABLE 3. Flexural strength

Sample	Average strength (MPa)	Coefficient of variation (%)
N51A glass matrix	64	14.5
Nextel 480–glass	65.7	18.9
SnO_2-coated Nextel 480–glass	86.43	16.44
BN-coated Nextel 480–glass	76.3	5.1

3.2. *Mechanical properties*

The bend strengths of the unreinforced matrix and coated and uncoated fiber composite samples are given in Table 3. The results are an average of four tests. It is clear that the addition of the coated fibers did not lead to any loss of strength of the matrix; if anything there was an increase in the strength. The tin-dioxide-coated fiber composites exhibited the largest strength increase (30%) while the boron-nitride-coated fiber composites showed a smaller increment (15%) as compared to the uncoated fiber composites.

TABLE 4. Static fracture toughness

Sample	Average static K_{Ic} (MPa m$^{1/2}$)	Coefficient of variation (%)
Nextel 480–glass	1.11	8.38
SnO_2-coated Nextel 480–glass	0.937	2.84
BN-coated Nextel 480–glass	2.12	10.68

The results of the static fracture toughness tests (average of five each) are given in Table 4. Incorporation of the Nextel fibers (both coated and uncoated) into the glass matrix resulted in an increase in the static toughness of the composite. The maximum increase was observed for the boron-nitride-coated fiber composites. The tin-dioxide-coated samples showed the smallest increment, and the value for the toughness was in fact lower than that for the uncoated fiber samples.

A schematic of the stress–displacement curves and the failure modes for the composites is shown in Fig. 4. It is important to note that the slope of the load–displacement curves for all the composites up to the maximum load was constant and matrix cracking did not occur till that point. This behavior is significantly different from that of other ceramic fiber–ceramic matrix composites [21–23], which exhibit either multiple matrix cracking, or single matrix cracking before the maximum load is reached, or both. While the uncoated and tin-dioxide-coated fiber composites exhibited typically brittle characteristics (types 1 and 2 in Fig. 4), the boron-nitride-coated fiber composite exhibited fiber debonding and pull-out after the maximum load point (type 3 in Fig. 4). For the boron-nitride-coated fiber composites (curve 3), at point A on the stress–displacement curve, the matrix had cracked completely on both the tensile and compressive sides of the samples. The load beyond point A, however, dropped in a non-catastrophic manner. It is worth emphasizing that the energy absorbed beyond point A is not accounted for in the static toughness formula.

The formula for the static fracture toughness (eqn. (1)) is based on a linear elastic fracture mechanism, *i.e.* we assume that the load–displacement behavior of the composite is linear and that self-similar crack propagation occurs. The use of this expression is valid and useful in the present case up to the point the matrix cracked, because the load–displacement behavior of the composite was linear, and a single crack propagation up to that point. In order to account for the energy absorbed by the processes occurring beyond point A (maximum load), the fracture energy of the samples was calculated by measuring the area under the load–displacement curve [24, 25]. Such a measure of fracture energy spent in the fracture process is straightforward and pragmatic. Determining the area

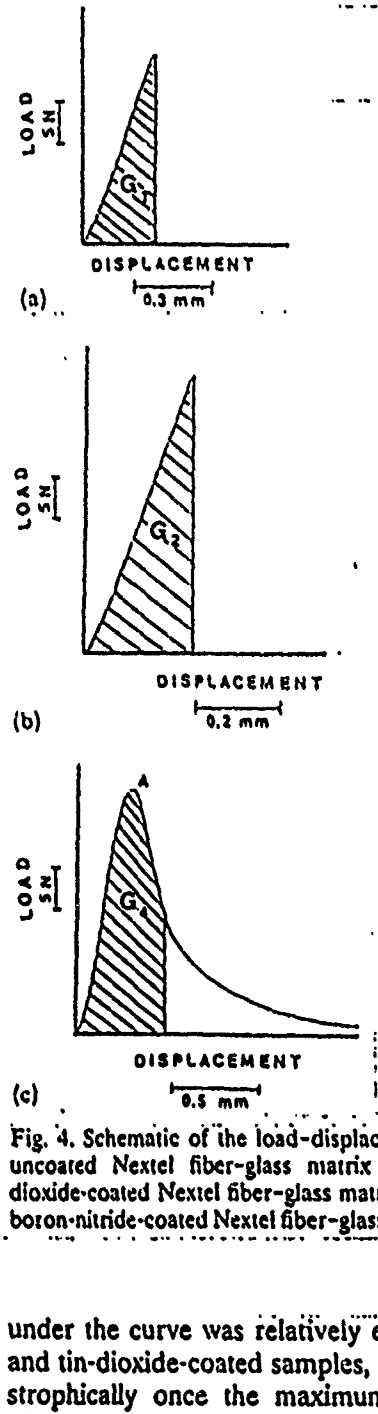

Fig. 4. Schematic of the load–displacement curves for: (a) the uncoated Nextel fiber–glass matrix composite, (b) the tin-dioxide-coated Nextel fiber–glass matrix composite, and (c) the boron-nitride-coated Nextel fiber–glass matrix composite.

TABLE 5. Fracture energies

Sample	Average fracture energy per unit area of crack surface ($J\ m^{-2}$)
N51A glass matrix	6–8 [21]
Nextel 480–glass	28.9
SnO_2-coated Nextel 480–glass	17.65
BN coated Nextel 480–glass (50% max. load)	152.7

under the curve was relatively easy for the uncoated and tin-dioxide-coated samples, since they failed catastrophically once the maximum load was reached. However, in the case of the boron-nitride-coated samples, the load–displacement curve was not as geometrically favorable as in the case of the aforementioned samples.

The problem was in trying to determine the cut-off point on the curve, since the load did not drop to zero even for a very large displacement. We decided to use 50% of the maximum load as the cut-off point. This choice was based on the fact that beyond this point the load on the composite had dropped to a fairly low value and seemed to remain fairly constant with progressive cross-head displacement. The results of the measured fracture energies for different samples are given in Table 5. The value for the N51A glass matrix is taken from ref. 26.

The different fracture mechanisms which can occur in ceramic fiber–ceramic matrix composites, where the stress and strain failure of the matrix are lower than those of the fiber, have been discussed by a number of researchers [27–29]. At the point where the failure strain of the matrix is reached, the matrix cracks and load is transferred to the fibers across the interface. Using a simple load balance, we obtain

$$\sigma^*_m A_m = 2\pi\tau r l_c N \qquad (2)$$

where σ^*_m is the fracture stress of the matrix, A_m is the area of the matrix, τ is the interfacial bond strength, r is the radius of the fiber, l_c is the length of the fiber over which the load is transferred (and is also equal to the length of the blocks into which the matrix cracks [30]), and N is the total number of fibers.

Rearranging eqn. (2) we get

$$l_c = \frac{\sigma^*_m V_m r}{2\tau V_f} \qquad (3)$$

where V_f is the volume fraction of the fibers and V_m is the volume fraction of the matrix.

From eqn. (3) it can be seen that a high value of τ leads to a smaller l_c and vice versa. In the case of the systems investigated, the magnitude of the interfacial bond and the flexural mode of testing suppressed multiple matrix cracking (small l_c), and only a single matrix crack was observed in all of the samples tested. In a flexural test, the maximum tensile stress is highly localized to a region at the center of the sample, which is not conducive to multiple fracture in the matrix. In such a case a single crack is initiated at the center of the sample, as can be seen in Fig. 5. The failure mode of the composite beyond this point is controlled by the fiber–matrix bond. If the bonding between the fiber and matrix is very strong, fiber pull-out does not occur, and failure of the matrix usually results in failure of the fibers and the composite as well (types 1 and 2 in Fig. 5). If the fiber–matrix bond is relatively weak, then the fiber debonds and pulls out of the matrix, and the

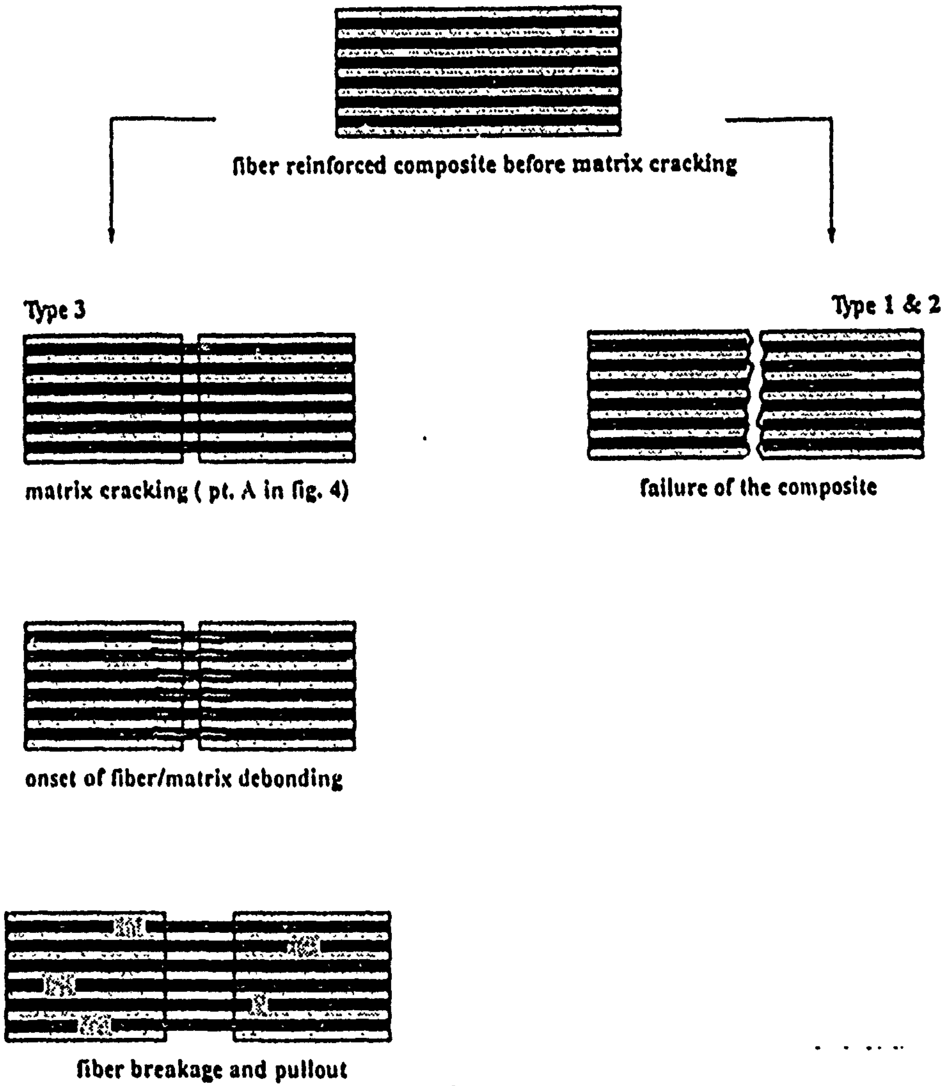

Fig. 5. Schematic of the failure modes observed in the different composites: type 1, uncoated Nextel fiber-glass matrix composite; type 2, tin-dioxide-coated Nextel fiber-glass matrix composite; type 3, boron-nitride-coated Nextel fiber-glass matrix composite.

composite fails in a more graceful manner (type 3 in Fig. 5).

In the case of a composite exhibiting such features (absence of multiple matrix cracking), if the load transferred to the fibers is insufficient to induce debonding, the fracture energy of the composite is simply the volume-weighted sum of the surface energies of the fiber and matrix. Let us call it case 1, and denote the fracture energy in this case as G_1, which is given by [29]

$$G_1 = 2(V_f\gamma_f + V_m\gamma_m) \tag{4}$$

where V represents the volume fraction, γ the surface energy and the subscripts f and m represent the fiber and matrix respectively.

In the presence of a coating (case 2) eqn. (4) can be modified to give the fracture energy G_2 as

$$G_2 = 2[V_f\gamma_f + V_i\gamma_i + (1 - V_f - V_i)\gamma_m] \tag{5}$$

where the subscript i denotes the interphace (coating).

If the fiber-matrix debonding stress is much lower than the fiber failure stress, debonding will occur before fiber failure (and after matrix cracking) (case 3). As the loading continues, the debonding extends along the interface, and the fiber slips and dissipates energy by friction. If the fiber strength is not distributed (*i.e.* the Weibull modulus is high), the fibers break in the plane of the main matrix crack, and the degree of fiber slippage is minimum. The fracture energy G_3, in this case can be written as [31]

$$G_3 = G_2 + \text{debonding contribution} \tag{6}$$

If the Weibull modulus of the fibers is small, the fibers will break at different points along their length, and additional energy will be required for fiber pull-out. We can write the fracture energy for this case G_4 as [32]

$$G_4 = G_3 + \text{pull-out contribution} \qquad (7)$$

In eqns. (6) and (7) we have omitted the detailed expressions for the debonding and pull-out components.

Scanning electron microscopy of the fracture surfaces of the samples revealed some interesting information and was very useful in corroborating some of the conclusions drawn from the mechanical tests. The fracture surface of an uncoated Nextel 480-glass sample can be seen in Fig. 6. The fracture features are characteristically brittle and specimen failure was catastrophic in nature. The presence of the fibers in the matrix did not seem to affect the nature of the crack growth in the matrix and the fracture surface was very planar. The features on the tin dioxide samples were very similar to those observed on the fracture surface of an uncoated fiber composite (Figs. 7(a) and 7(b)). These composites also broke suddenly after reaching the maximum load. A point worth noting in this case was the nature of the tin dioxide coating. The coating in this case appeared to have an irregular surface texture. Neither of the two samples (uncoated and tin dioxide coated) exhibited any indication of fiber debonding or pull-out.

Fracture of the boron-nitride-coated Nextel 480 glass composites exhibited features different from those observed in the case of the previous composites (Figs. 8(a) and 8(b)). Extensive fiber-matrix debonding and fiber pull-out were observed over the entire fracture surfaces. The pull-out, however, did seem to occur irregularly in that the pull-out lengths of the fibers over the entire cross-section varied. The average pull-out length was 40 μm. On the basis of these observations, the various fracture energy terms were computed from the area under the load-displacement curves and are provided in Table 6. The following conclusions can be drawn on the basis of the present work. The uncoated

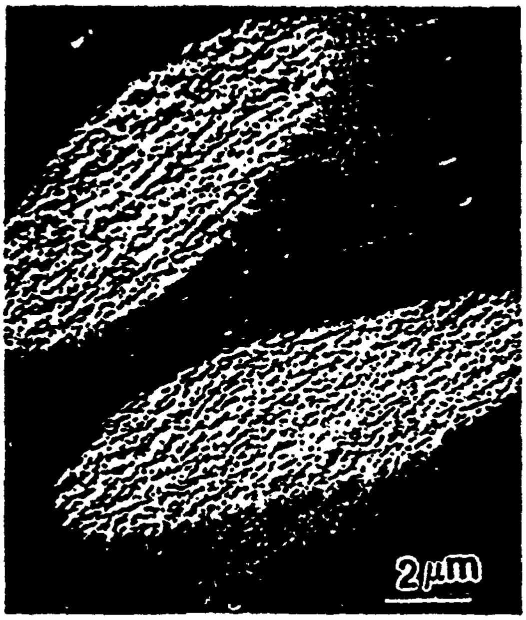

Fig. 6. Scanning electron micrograph of a fracture surface of an uncoated Nextel fiber-glass matrix composite.

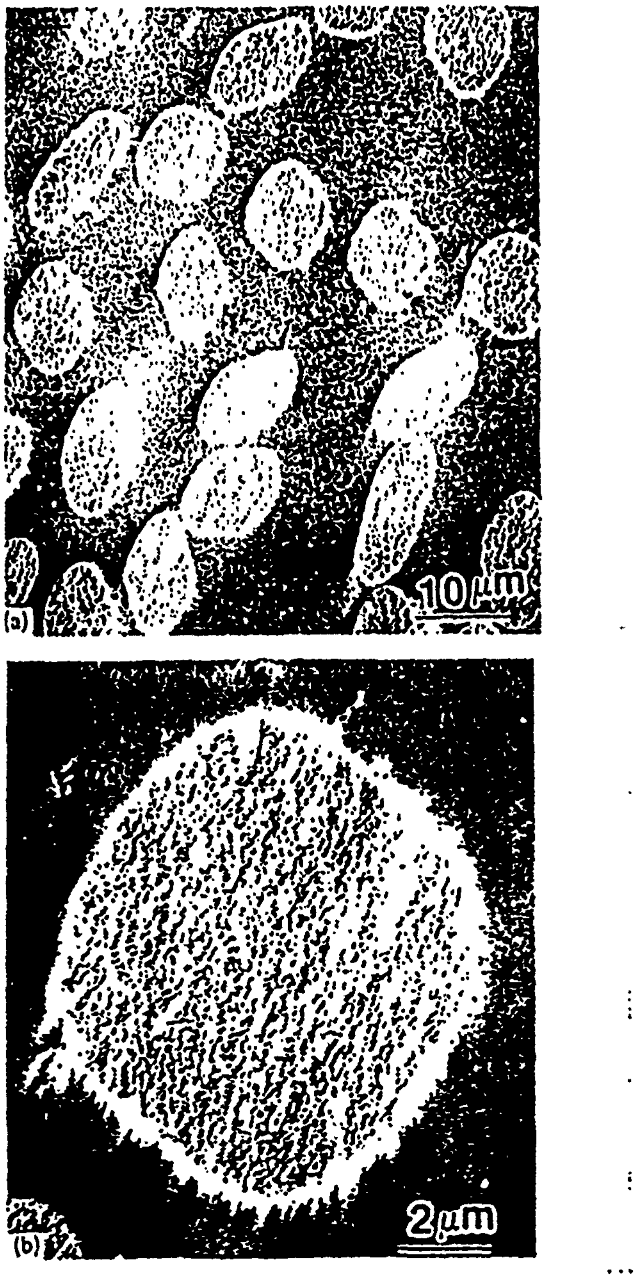

Fig. 7. Scanning electron micrographs of a fracture surface of a tin-dioxide-coated Nextel fiber-glass matrix composite illustrating (a) the nature of the tin dioxide coating, and (b) the absence of fiber debonding and pull-out in composite failure.

Fig. 8. (a), (b) Scanning electron micrographs of a boron-nitride-coated Nextel fiber–glass matrix fracture surface illustrating debonding and pull-out.

fibers were relatively strongly bonded to the glass matrix and hence exhibited reasonably high strength but relatively no improvement in the toughness. The tin-dioxide-coated samples were also strongly bonded to the matrix. Although the coating does not react chemically with alumina, it reacted with the silica in the glass matrix and fiber (mullite). In addition, the surface irregularities on the coating aided in mechanical bonding.

TABLE 6. Various components of the total fracture energy of different composites

Composite sample	Fracture energy (J m^{-2})			
	G_1	G_2	G_3	G_4
Uncoated Nextel-glass	28.9	—	0	0
SnO_2-coated Nextel-glass	—	17.65	0	0
BN-coated Nextel-glass	—	75.9	—	152.7

The boron-nitride-coated fiber samples exhibited a lower strength as compared to the tin-dioxide-coated samples but significantly higher toughness values. The energy absorbed in the fracture process was an order of magnitude higher as compared to the uncoated and tin-dioxide-coated samples. A very important point is that the improvement in the fracture energy absorbed was not obtained at the expense of a reduction in fracture strength. These boron-nitride-coated Nextel fiber composites still maintained a reasonable degree of their strength as can be seen in Table 3. The increased energy absorption was due to fiber-related processes such as debonding and pull-out, which were possible because of the relatively weak bonding provided by the boron nitride coating.

4. Conclusions

The present work demonstrates the feasibility of using boron-nitride-coated Nextel 480 fibers as a reinforcement for the N51A glass matrix. The results obtained indicate that the choice of the coating is important as it affects the overall mechanical behavior of these composites. As expected, the tin dioxide coating did not provide an improvement in the toughness because of the chemical and mechanical bonding between the coating and matrix as well as between the coating and fiber. The boron nitride coating on the other hand exhibited the most desirable characteristics. A reasonably high strength and a fracture toughness significantly above that of the unreinforced glass were obtained in this system.

Acknowledgments

This work was supported by the U.S. Office of Naval Research (contract N00014-89-J-1459). The research was also sponsored in part by the U.S. Department of Energy, Assistant Secretary for Conservation and Renewable Energy, Office of Transportation Systems, as part of the High Temperature Materials Laboratory User Program, under contract DE-AC05-840R21400 with Martin Marietta Energy Systems. Thanks are due to Mr. J. O'Kelly of 3M Corporation for coating the Nextel 480 fibers.

References

1 D. B. Marshall and A. G. Evans, *J. Am. Ceram. Soc., 68* (1985) 225.

2 A. G. Evans and R. M. McMeeking, *Acta Metall., 34* (1986) 2435.

3 K. M. Prewo, *J. Mater. Sci., 21* (1986) 3590.

4 B. Budianski, J. W. Hutchinson and A. G. Evans, *J. Mech. Phys. Solids, 34* (1986) 167.

5 E. Y. Luh and A. G. Evans, *J. Am. Ceram. Soc., 79* (1987) 466.

6 R. L. Lehman and C. A. Doughan, *Comp. Sci. Tech., 37* (1990) 149.

7 D. C. Phillips, N. Park and R. J. Lee, *Comp. Sci. Tech., 37* (1990) 249.

8 A. G. Evans, *J. Am. Ceram. Soc., 73* (1990) 187.

9 K. K. Chawla, *Composite Materials: Science and Engineering*, Springer, New York, NY, 1987.

10 A. Maheshwari, K. K. Chawla and T. A. Michalske, *Mater. Sci. Eng. A, 107* (1989) 269.

11 F. D. Gac, *Rep. LA 11592-T*, Los Alamos National Laboratory, Los Alamos, NM, 1989.

12 R. N. Singh and S. Gaddipati, *J. Am. Ceram. Soc., 71* (1988) C 100.

13 D. P. Partlow, *Adv. Ceram. Mater., 3* (1988) 553.

14 M. K. Brun and R. N. Singh, *Adv. Ceram. Mater., 3* (1988) 553.

15 D. D. Johnson, A. R. Holtz and M. F. Grether, *Ceram. Eng. Sci. Proc., 8* (1987) 744.

16 R. N. Singh, *Ceram. Eng. Sci. Proc., 8* (1987) 636.

17 K. K. Chawla, *Composite Materials: Science and Engineering*, Springer, New York, NY, 1987, p. 134.

18 K. M. Prewo and J. J. Brennan, *J. Mater. Sci., 15* (1980) 463.

19 G. K. Bansal and W. H. Duckworth, *Am. Soc. Test. Mater., Spec. Tech. Publ., 678* (1979) 38–46.

20 T. Macke, J. M. Quenisset, D. Neuilly, J. P. Rocher and R. Naslain, *Comp. Sci. Tech., 37* (1990) 267.

21 D. B. Marshall, A. G. Evans, *J. Am. Ceram. Soc., 68* (1985) 225.

22 G. C. Wei and P. F. Becher, *Am. Ceram. Soc. Bull., 64* (1985) 298.

23 R. N. Singh, *J. Am. Ceram. Soc., 73* (1990) 2390.

24 D. C. Phillips, *J. Mater. Sci., 7* (1972) 1175.

25 R. A. J. Sambell, A. Briggs, D. C. Phillips and D. H. Bowen, *J. Mater. Sci., 7* (1972) 676.

26 T. A. Michalske and J. R. Hellmann, *J. Am. Ceram. Soc., 71* (1988) 725.

27 H. Osmani, D. Rouby and G. Fantozzi, *Comp. Sci. Tech., 37* (1990) 191.

28 D. B. Marshall, B. N. Cox and A. G. Evans, *Acta Metall., 33* (1985) 2013.

29 A. G. Evans, *J. Am. Ceram. Soc., 73* (1990) 187.

30 J. Aveston, G. A. Cooper and A. Kelly, in *Properties of Fiber Composites*, IPC Science and Technology Press, Sutton, 1971, p. 15.

31 B. Marshall and B. N. Cox, *Acta. Metall., 33* (1985) 2013.

32 J. K. Wells and P. W. R. Beaumont, *J. Mater. Sci., 20* (1985) 1275.

Appendix F : Effect of Interfacial Roughness on Fiber Pullout in Alumina/Tin Dioxide/Glass Composites.

EFFECT OF INTERFACIAL ROUGHNESS ON FIBRE PULLOUT IN ALUMINA/SnO_2/GLASS COMPOSITES

R. Venkatesh and K.K. Chawla
Department of Materials and Metallurgy
New Mexico Institute of Mining and Technology
Socorro, NM 87801

Alumina and glass form a strong chemical bond and the resulting composite is brittle [1,2]. An SnO_2 coating that has no diffusion in alumina and very little diffusion in glass acts as an efficient diffusion barrier as well as a weak interphase that aids in crack deflection [3,4]. Some researchers (5,6) have shown the importance of interfacial roughness in fibre/matrix debonding characteristics during fibre push-out and pull-out tests. In another study [7], we show that roughness induced interfacial stress is an order of magnitude higher than radial tensile thermal stress in PRD-166 (Al_2O_3-ZrO_2) fibre/SnO_2 coating/N51A glass matrix composite. This roughness induced interfacial stress prevented any sliding of the SnO_2 coated fibre in a nanoindenter pushout test up to a load of 110 mN and also affected the pull-out characteristics of the fibre in alumina (PRD-166)/SnO_2/glass composites. Figure 1 shows the partial fibre pull-out and separation of the alumina/SnO_2 interface in a flexural test. Note also the very rough surface of the PRD-166 fibre.

In order to verify this effect of roughness, we fabricated an N51A glass matrix composite reinforced with SnO_2 coated Saphikon monofilaments. Saphikon is a single crystal alumina fibre with a diameter of 125 μm as compared to 20 μm for alumina (PRD-166) fibre, but more importantly, the surface of Saphikon is smoother than that of PRD-166 fibre.

Three-point bend test fracture surface of alumina (PRD-166) fibre/SnO_2/glass composite is shown in Fig.1 (a and b). Fracture surface of Saphikon/SnO_2/glass composite is shown in Figs. 2 and 3. Note the neat fiber pull-out in Saphikon/SnO_2/glass composite. The fibre pullout lengths in Saphikon fiber/SnO_2/glass composite are greater than alumina

(PRD-166) fibre/SnO_2/glass composites. Average pullout length in Saphikon/SnO_2/glass composite was 106 μm, which is about five times larger than in alumina (PRD-166) fibre/ SnO_2/glass composite. Fig. 4(b and c) shows energy dispersive analysis of the pulled out Saphikon fibre surface, at regions marked a and b in Fig. 4a, respectively. In region a, the EDS analysis shows only Al and no Sn. This is as expected since SnO_2 and Al_2O_3 have no mutual solid solubility and hence fibre debonding and pull-out takes place at Al_2O_3/SnO_2 interface. Region b shows existence of some Si and Sn. This could be due to diffusion of some Sn into glass and vice-versa.

Thus, we can conclude that in addition to the radial tensile thermal stress, interfacial roughness has a pronounced effect on the extent of fibre pull-out. This will, in turn, affect toughness in ceramic matrix composites.

Acknowledgements

This work was supported by the Office of Naval Research, Contract No. N0014-89-J-1459. Thanks are due to Dr. S. Balsone of Wright Patterson Air Force Base and Dr. A.H. Muir, Jr. of the Rockwell Science Center for providing the Saphikon fiber.

References

(1) J.F. Bacon, K.M. Prewo, and R.D. Veltri, in Proc: Second Int. Conf. on Composite Materials, Toronto, Canada, AIME, New York, 1978, p.752.

(2) T.A. Michalske and J.R. Hellmann, J. Am. Cer. Soc., 71(9), (1988) 725.

(3) A. Maheshwari, K.K. Chawla, and T.A. Michalske, Material Science and Engg., A107, (1989) 269.

(4) M. Siadati, K.K. Chawla, and M.K. Ferber, J. Mater. Sci., 26, (1991) 2743.

(5) R.J. Kerans and T.A. Parthasarathy, J. Am. Cer. Soc., 74, (1991) 1585.

(6) P.D. Jero and R.J. Kerans, Scripta Met., 24, (1990), 2315.

(7) K.K. Chawla, M.K. Ferber, and R. Venkatesh, ~~to be published~~. submitted for publication.

List of Captions

Figure 1 Fracture surface of alumina (PRD-166) fibre/SnO_2/glass composite showing partial fibre pull-out and separation of the alumina (PRD-166) fibre/SnO_2 interface. Note also the very rough surface of the PRD-166 fibre. (a) low magnification (b) high magnification

Figure 2 Fracture surface of Saphikon/SnO_2/glass composite. Note the neat fibre pull-out.

Figure 3 Fracture surface of Saphikon/SnO_2/glass composite. Note the fibre debonding at the Saphikon/SnO_2 interface.

Figure 4(a) Fracture surface of Saphikon/SnO_2/glass composite. (b) Energy dispersive analysis of pulled out Saphikon fibre surface at region marked a in Fig. 4a showing only Al and no Sn. (c) Energy dispersive analysis of pulled out Saphikon fibre surface at region marked b in Fig. 3a showing presence of both Si and Sn.

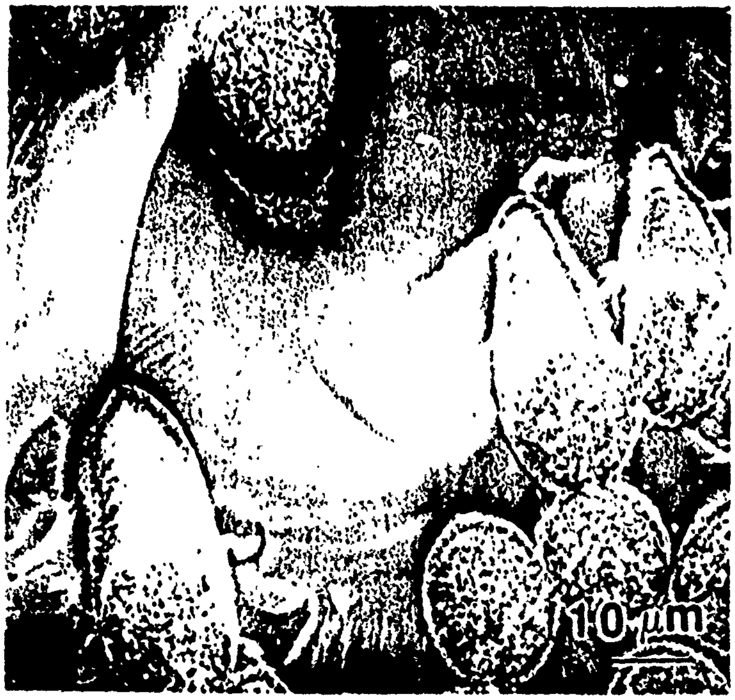

Fig 11a

Fig. 21

F - 2

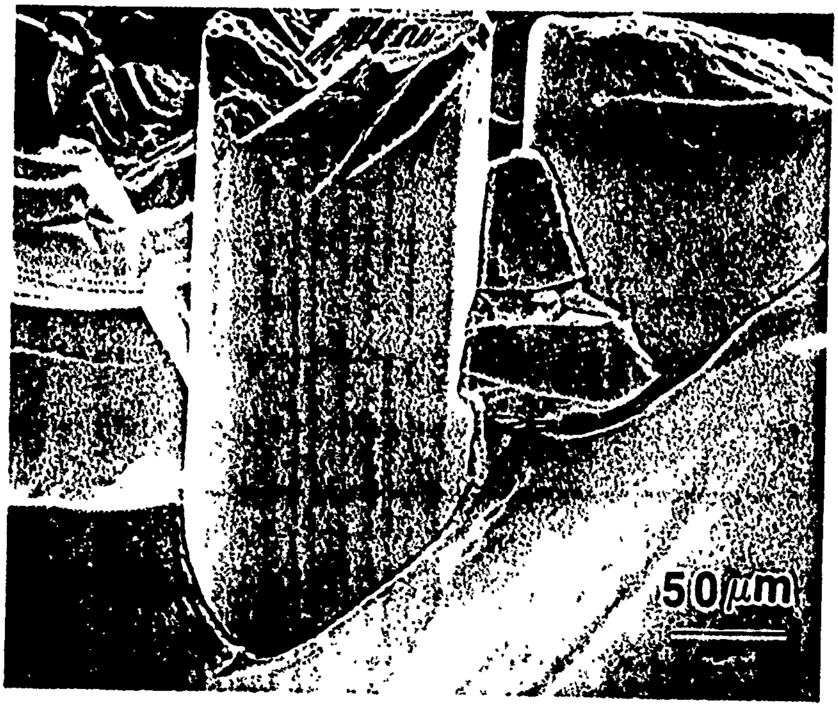

Fig 3

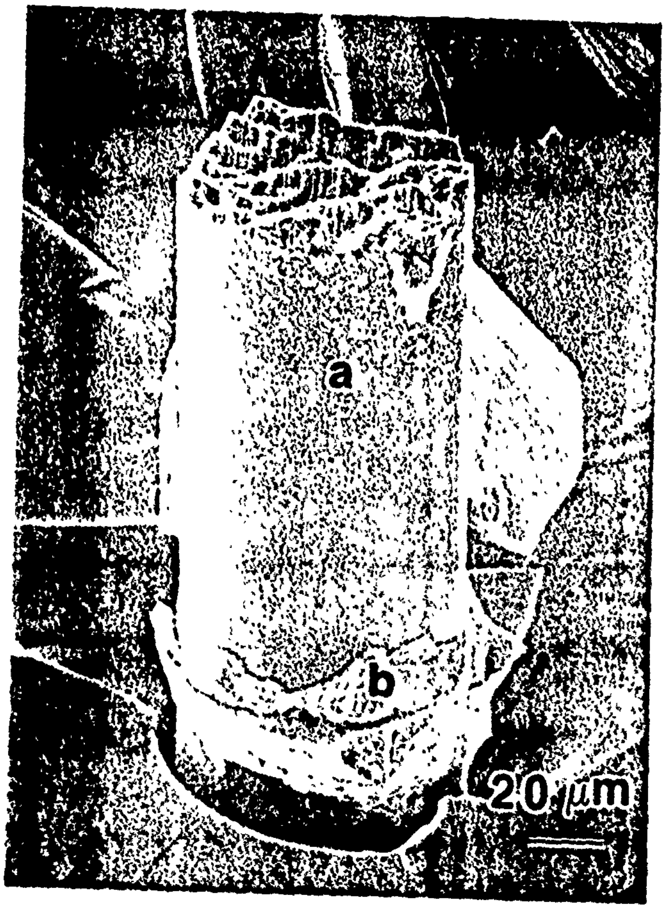

[illegible] 2

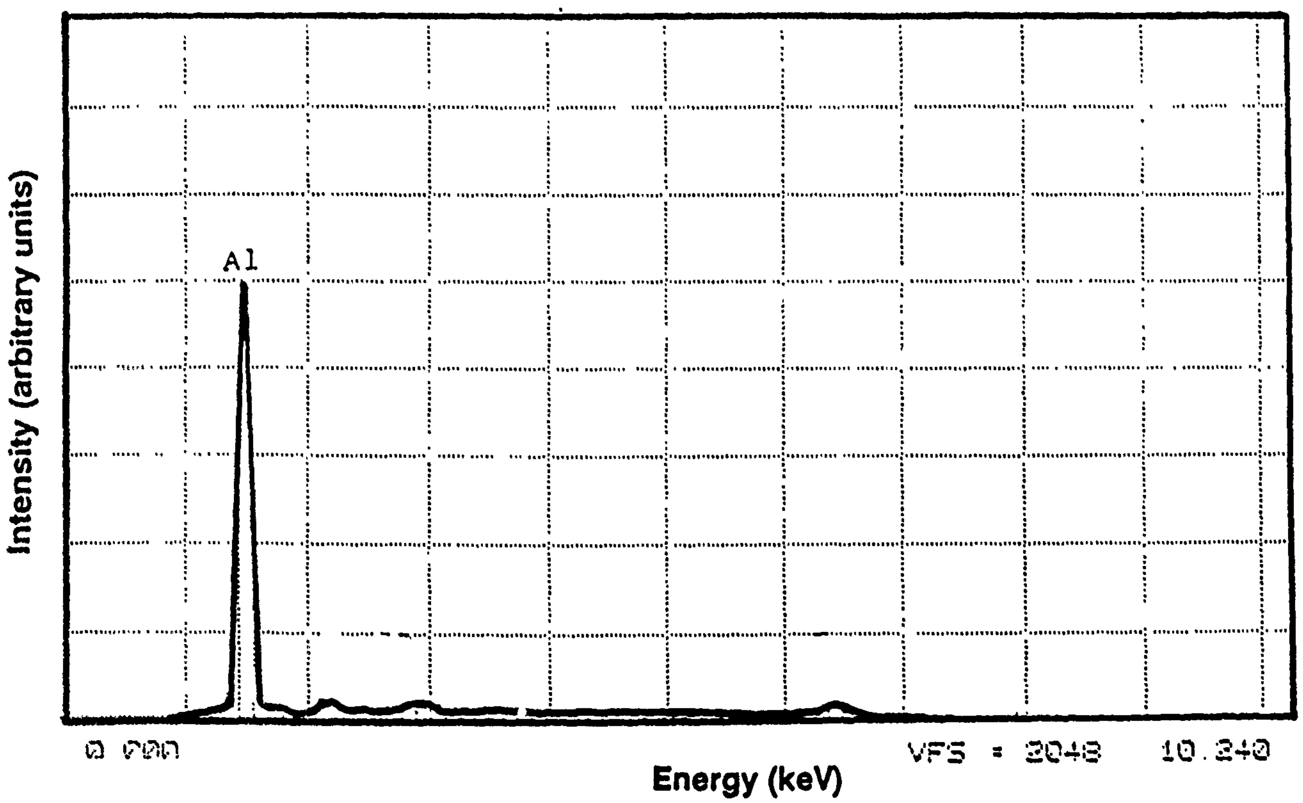
Intensity (arbitrary units)
Al
0.000
VFS = 2048
10.240
Energy (keV)

Fig 4b

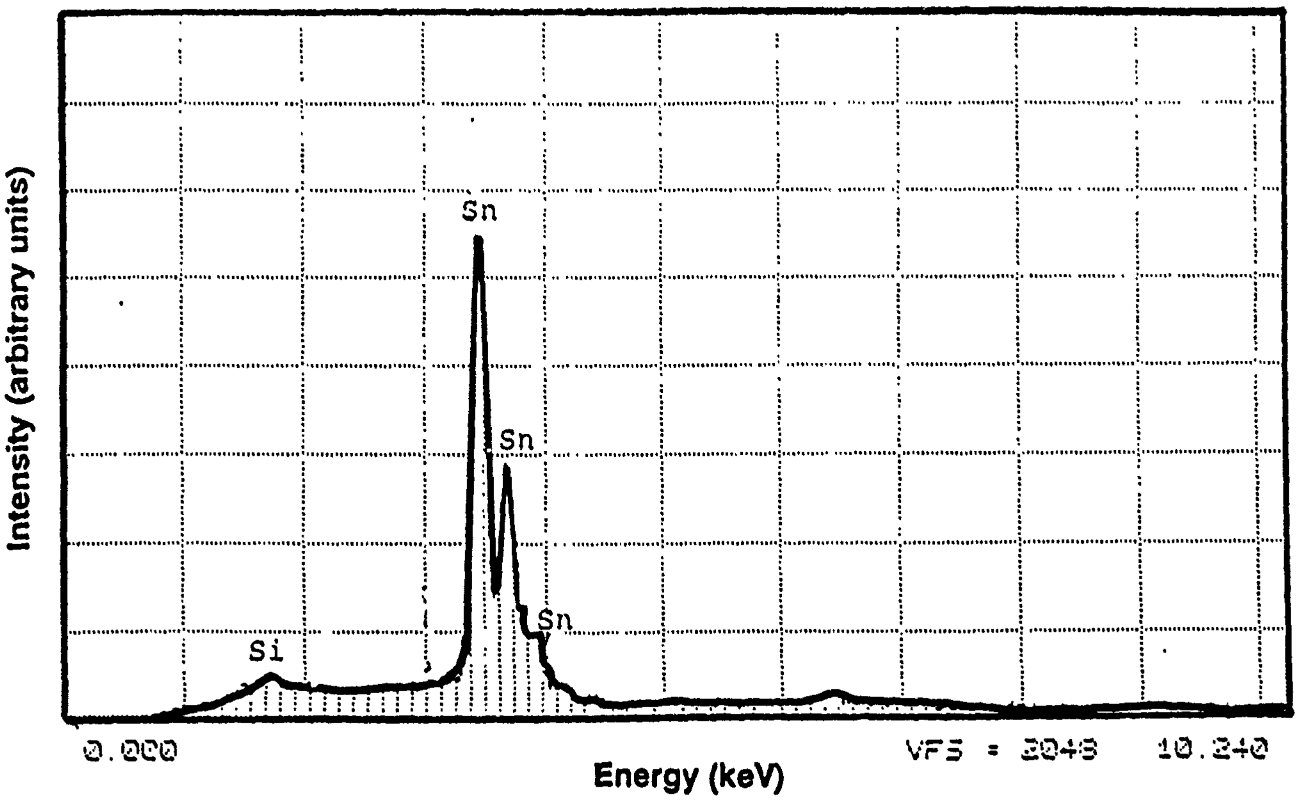
Intensity (arbitrary units)
Sn
Sn
Sn
Si
0.000
VFS = 2048
10.240
Energy (keV)

Fig 4 c

Appendix G : Effect of Boron Nitride Coating on the Tensile Strength of Nextel 480 Fibers.

EFFECT OF BORON NITRIDE COATING ON TENSILE STRENGTH OF NEXTEL 480* FIBER

by

J.A. Fernando[1], K.K. Chawla[1], M.K. Ferber[2], and D. Coffey[2]

[1]**Department of Materials and Metallurgical Engineering**
New Mexico Institute of Mining and Technology
Socorro, New Mexico 87801

[2]**High Temperature Materials Laboratory**
Oak Ridge National Laboratory
Oak Ridge, TN 37831

* Trade mark of the 3M Company.

I. Introduction

The attractive thermal and mechanical properties of ceramics have provided the incentive to increase the toughness, i.e., the energy absorbed in the fracture process or work of fracture. Methods of increasing toughness in ceramics include addition of second phase particles and incorporation of whiskers/fibers. Increase in toughness of fiber–reinforced ceramic composites is achieved via matrix microcracking, interfacial delamination, and crack deflection at fiber–matrix interface in conjunction with fiber debonding and subsequent fiber pullout [1]. The interface between fiber and matrix, without an interfacial coating, depends largely on the particular system and the temperatures during processing. By incorporating a known interfacial layer the interfacial properties are more controllable. It is important to analyze what the coating does to the fiber in terms of its tensile strength, surface characteristics, etc. Two main items in this regard are the coating surface roughness vis a vis uncoated fiber surface roughness and the residual thermal stress state at the fiber/coating interface [2,3]. Boron nitride and carbon are common coatings used in many high performance fiber reinforced composites [3]. An increase in the mean tensile strength of the boron nitride coated fibers can be expected due to the surface healing effect of the boron nitride coating [4,5]. Dhingra [5] reported a 50% increase in tensile strength of the SiO_2 coated alumina FP fiber in comparison to the uncoated fiber. A similar increase was also reported by Pysher [4] et al. in the case of SiO_2 coated PRD–166 fiber. In both cases, the increase was attributed to the healing of surface flaws. Figure 1 illustrates the idea of defect healing in a schematic manner. Nextel 480 is essentially a mullite fiber and, being an oxide fiber, is thermally very stable in air [1]. It is potentially an ideal reinforcing material for glass and ceramic composites. The relative smoothness of the boron nitride coated Nextel 480 fiber can also be very advantageous in enhancing the toughness due to the low interfacial frictional stresses during fiber pullout [3]. The aim of this work was to study the effect of boron nitride coating on the tensile strength of Nextel 480 fibers using a two parameter Weibull distribution.

III. Results and Discussion

3.1 Microstructural Characterization and Surface Defect Healing

The surface roughness of the uncoated and the boron nitride coated fibers are illustrated in Figure 2. It is clear that the boron nitride coated fiber surface is appreciably smoother than the uncoated fiber surface. The notch root radius, ϱ, and the depth of the notch, a, measurements were obtained using SEM micrographs. The average values of the ratio of a to ϱ were calculated to be 0.544 and 0.028 for the uncoated and boron nitride coated fiber surfaces, respectively. The cross–sectional area of the Nextel 480 fibers showed very little scatter; this was also verified by SEM and optical microscope.

The maximum stress for a defect in the form of a elliptical cavity occurs at the two extremities of the ellipse and is given by the well known Inglis [9] formula

$$\sigma_{\max} = \sigma(1 + 2a/b) \qquad (1)$$

where 2a and 2b are the major and minor axes of the ellipse, respectively. For an extremely flat ellipse the equation for the maximum stress becomes

$$\sigma_{\max} = \sigma\left(1 + 2\sqrt{a/\varrho}\right) \qquad (2)$$

where ϱ, the notch radius, is equal to b^2/a. Note that as ϱ becomes large due to the crack healing effect of the boron nitride coating, the stress concentration factor term, $2\sqrt{a/\varrho}$, becomes small and, hence, $\sigma_{\max}$ becomes small. The values of the $2\sqrt{a/\varrho}$ term were estimated from Figure 2 for the uncoated and boron nitride coated fiber to be 1.476 and 0.336, respectively. The estimation was made from an average of eight measurements in each case. For the same applied stress, these terms indicate that the maximum stress occurring at the tip of a notch on the surface of the boron nitride coated fiber is lower by a factor of 0.54 in comparison to the maximum stress occurring on the surface of the uncoated fiber.

3.2 Tensile Testing and Weibull Analysis

The fiber tensile strength was analyzed using a two parameter Weibull where $$\Gamma(n) = \int_0^\infty e^{-x}x^{n-1}dx$$

$$CV = 100(s/\bar{\sigma})$$

The plots of the natural log of the tensile strength, σ_i, and $\ln(\ln[(N+1)/(N+1-i)])$ of both the uncoated and boron nitride coated fibers are shown in Figures 3 and 4. The straight line plots indicate the applicability of Weibull distribution to tensile strength of these fibers, coated and uncoated. A mean tensile strength of 1766 MPa with a standard deviation 544 MPa was determined for the uncoated fibers. This mean strength value matches reasonably well with the 1900 MPa result of Johnson et al. [11] and the 1500 MPa result of Pysher et al. [4]. The gage lengths used in their tests were 51 mm and 75 mm, respectively. The boron nitride coated fibers showed an increase in mean tensile strength to 2905 MPa with a standard deviation of 762 MPa, see Table 3. The values of the Weibull modulus were 3.76 and 4.37 for the uncoated and boron nitride coated fibers, respectively. These values indicate a considerably large scatter in the strength values. However, a relatively large scatter in ceramic fibers is not unexpected due to their sensitivity to population and size of surface and internal flaws. Table 4 gives the Weibull modulus values for some similar high modulus, high strength oxide fibers. The Weibull modulus values obtained in our study compares well with the values for other ceramic fibers.

Assuming that the fibers (coated as well as uncoated) fail due to a surface flaw, for the same applied stress we obtained the ratio of maximum stress occurring at the tip of a notch on the surface of the boron nitride coated fiber to the maximum stress occurring on the surface of the uncoated fiber to be 0.54. The experimentally obtained Weibull mean strengths showed that uncoated fiber mean strength was lower than the boron nitride coated fiber mean strength by a factor of 0.61. This is in good agreement with the theoretical estimate. Thus, the smooth boron nitride coating on Nextel 480 fiber heals the surface defects and contributes to strength enhancement.

IV. Conclusions

The boron nitride coating on the Nextel 480 fiber resulted in a significant increase in the mean tensile strength. This increase was mainly due to the healing of surface defects by the coating. The effect of thermal stresses caused by the mismatch in the thermal expansion coefficients of the fiber and the coating was insignificant.

V. Acknowledgments

This work was supported by the Office of Naval Research, Contract No. N0014-89-J-1459. The research was also sponsored in part by the U.S. Department of Energy, Assistant Secretary for Conservation and Renewable Energy, Office of Transportation Systems, as part of the High Temperature Materials Laboratory User Program, under contract DE-AC05--840R21400 with Martin Marietta Energy Systems, Inc. Thanks are due to Mr. J. O'Kelly, 3M Co. for coating the Nextel 480 fibers and Mr. Julian Ambriz, New Mexico Tech., for assistance in single fiber tensile testing.

List of Tables

Table 1. Properties of the Nextel 480 Fiber* and the boron nitride coating.

Table 2. Chemical Composition of the Nextel 480 Fiber* (wt. %).

Table 3. Weibull Parameters of Uncoated and Boron Nitride coated Nextel 480 fibers.

Table 4. Weibull modulus for some ceramic fibers.

List of Figures

Figure 1. Illustration of the defect healing effect of the boron nitride coating.

Figure 2. The smooth surface of the boron nitride coating. Note the rougher surface of the Nextel 480 fiber surface.

Figure 3. Weibull plot for uncoated Nextel 480 fibers.

Figure 4. Weibull plot for boron nitride coated Nextel 480 fibers.

Figure 5. Thermal stress distribution in the BN coated Nextel 480 fiber system.

Table 3. Weibull Parameters of Uncoated and Boron Nitride coated Nextel 480 fibers.

Fiber condition	α, $MPa^{-\beta}$	β	Weibull Mean Strength, $\bar{\sigma}$, MPa	Standard Deviation, s MPa	Coefficient of Variation,%	Correlation Coefficient, r^2
Uncoated	0.42×10^{-12}	3.76	1766.03	544.50	30.83	0.980
Boron Nitride Coated (0.2μm)	0.47×10^{-15}	4.37	2905.57	761.63	26.21	0.982

Table 4. Weibull modulus, β, for some ceramic fibers.

Fiber	Gage Length (mm)	β	Ref.
Sumitomo Alumina Fiber	100	3 – 6	13
PRD–166 (Du Pont)	17	3 – 4	2
Fiber FP (Du Pont)	19.8	6.6	14
Nextel 480 (3M)	12	4	This work

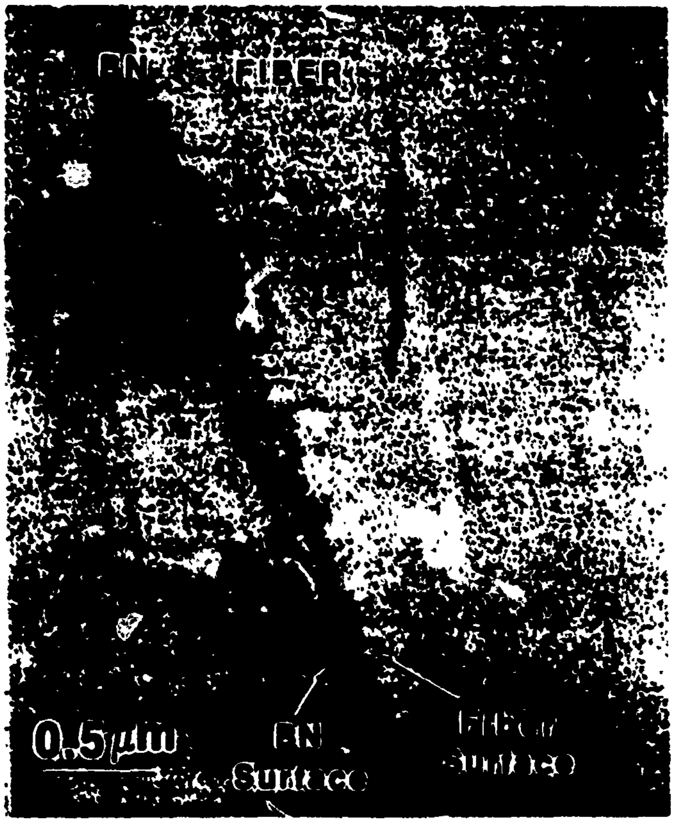

Figure 2. The smooth surface of the boron nitride coating. Note the rougher surface of the Nextel 480 fiber surface.

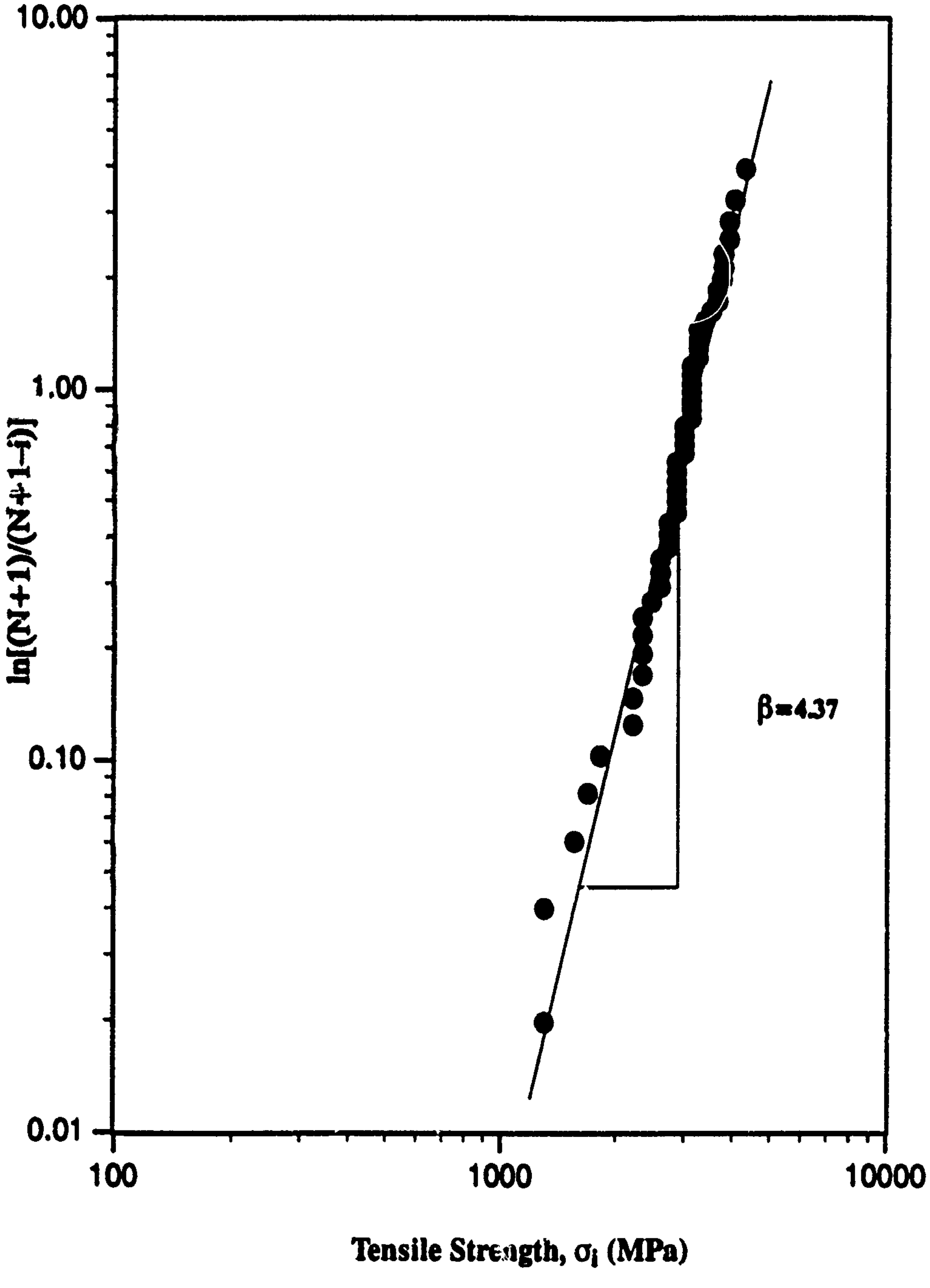

Figure 4. Weibull plot for boron nitride coated Nextel 480 fibers.

Appendix A

The cross-sectional area of the Nextel 480 fiber can be approximated as a simple combination of a rectangle with half circles at opposing ends.

$$\text{Area of fiber cross-section} = (M-m)m + \pi m^2/4$$

where M and m are defined in Figure A.2. From Figure A.1, we get $M = 12\ \mu m$ and $m = 8\ \mu m$. The equivalent diameter was calculated assuming a circular cross-section fiber having the same area as calculated above.

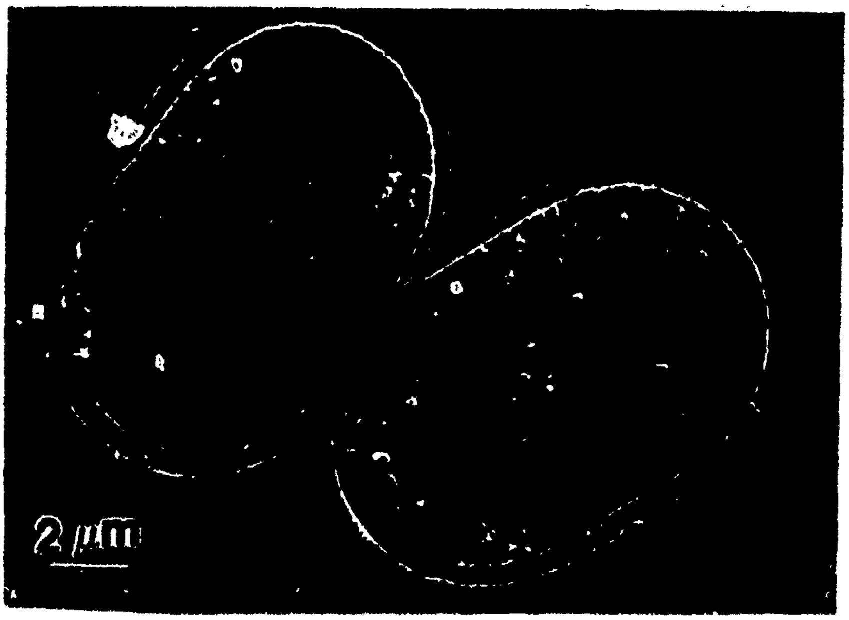

Figure A.1 SEM micrograph of uncoated Nextel 480 fiber embedded in glass. The glass around the fiber was etched away in order to delineate the fiber shape.

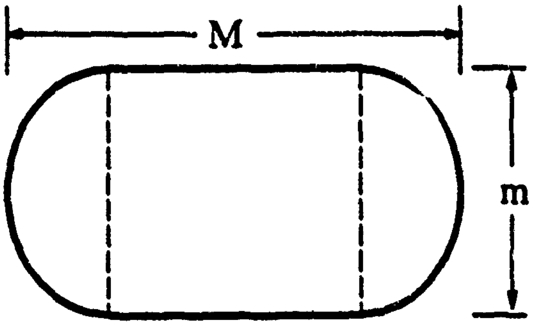

Figure A.2 Schematic of equivalent area of Nextel 480 fiber.

Appendix H : Some Observations on the Paper 'Influence of Tin Dioxide Interphase on the Residual Stresses in Alumina/Glass Composites.

Scripta METALLURGICA
et MATERIALIA

Vol. 26, pp. 859-860, 1992
Printed in the U.S.A.

Pergamon Press plc
All rights reserved

SOME OBSERVATIONS ON THE PAPER " INFLUENCE OF TIN DIOXIDE INTERPHASE ON THE RESIDUAL STRESSES IN ALUMINA FIBER / GLASS COMPOSITES " BY S.N. PATANKAR, C. SURYANARAYANA AND F.H. FROES

R. Venkatesh[1], K.K. Chawla[1], and M. Ferber[2]

[1] New Mexico Institute of Mining and Technology
Socorro, New Mexico 87801.
[2] Oak Ridge National Lab.,
High Temperature Materials Lab., Oak Ridge, TN 37831

(Received November 5, 1991)
(Revised November 14, 1991)

Patankar et al. (1) have recently evaluated thermal stress distribution in alumina fiber (PRD−166)/N51A glass and alumina/SnO_2/glass composites using models due to Hsueh et al. (2) and Vedula et al. (3,4). They concluded that these models predict compressive stresses at the SnO_2/glass interface which would adversely affect the toughness. In this communication we wish to discuss some of the errors involved in ref. 1 as well as point out our results of stress distribution in this composite system:

(1) The model of Hsueh et al. for thermal stresses is valid for low volume fraction of fibers (< 5% by volume). Thus, the use of the model of Hsueh et al. for glass matrix reinforced with 30 vol. % fibers in ref. 1 is not valid. The only way to use the model of Hsueh et al. for high volume fraction of fibers is to use the *self−consistent* model, i.e., outside the fiber one must use the average properties of the composite.

(2) In ref. 1, the authors have taken 770 °C as the setting temperature of N51A glass. This is incorrect. Based upon experiments conducted in our laboratory on this glass using an Orton dilatometer, this setting temperature is too high. For example, Fig. 1 shows that during cooling down to 500 °C viscous relaxation of glass occurred, i.e., up to this temperature the stresses were relaxed by viscous flow. Thus, the correct upper temperature to be taken for thermal stress evaluation is 500 °C.

(3) The authors in ref. 1 have taken wrong numerical values of thermal expansion coefficients for the alumina (PRD−166) fiber and SnO_2. Romine (5) reported a value of 9×10^{-6}/°C for thermal expansion of alumina (PRD−166) fiber. The correct value of thermal expansion for pure SnO_2 is 5.28×10^{-6}/°C (6). The thermal expansion coefficient value of SnO_2 taken by the authors in ref. 1 is for $SnO_2 + ZnO$. Using the correct values of thermal expansion coefficients, The model of Hsueh et al. (even though invalid) predicts a radial tensile stress at both alumina/SnO_2 and SnO_2/glass interface.

(4) Our studies (7,8) show no diffusion of Sn in alumina but some diffusion of Sn in glass. Hence, bonding at the alumina fiber/SnO_2 interface is purely mechanical and weaker than the bonding at the SnO_2/glass interface. In ref. 1, the authors using the model of Hsueh et al. (even though invalid) predict radial tensile stress at fiber/SnO_2 interface and compressive radial stress at SnO_2/glass interface. Even based on their erroneous calculations, they should have noted that the radial tensile stress at fiber/SnO_2 interface would still be effective in crack deflection and fiber debonding there.

(5) Using a cylindrical model we show (9) radial tensile stress at both fiber/SnO_2 and SnO_2/glass interface. Indentation cracks were made to travel from the glass matrix to the alumina fiber (9). In alumina/glass composite, because of the strong chemical bond, the indentation crack traveled unimpeded from glass to the fiber. In alumina/SnO_2/glass composite, the crack did not penetrate the fiber: instead it followed the fiber/SnO_2 interface. The radial tensile stress combined with the weak bonding at the fiber/SnO_2 interface provided conditions favorable for crack deflection. This is a very desirable attribute from a toughness point of view.

(6) The primary scope of the model of Vedula et al. is for composites reinforced with anisotropic fibers. Vedula et al. have concentrated on the stresses in the matrix. In ref. 1 the authors do not show the stress variation

0036-9748/92 $5.00 + .00

in the alumina/SnO_2/glass composites from the fiber to the matrix. In fact, they do not even show an interphase region. In order to use the model of Vedula et al. the authors in ref. 1 should have modified the equations given by Vedula et al. so as to calculate the stresses in the fiber and coating as well. The compressive radial stress at the coating/matrix interface could be due to inaccurate numerical values taken by the authors for thermal expansion coefficients of alumina (PRD−166) fiber and tin dioxide.

Acknowledgments

This work was supported by the Office of Naval Research (contract N00014−89−J−1459). Support was also received in part by the US Department of Energy, Assistant Secretary for Conservation and Renewable Energy, Office of Transportation Systems, as part of the High Temperature Materials User Program, under contract DE−AC05−840R21400 with Martin Marietta Energy Systems, Inc.

References

(1) S.N. Patankar, C. Suryanarayana, and F.H. Froes, Scripta Met. et Mater., 25, 1787(1991).
(2) C.H. Hsueh, P.F. Becher, and P. Angelini, J. Am. Cer. Soc., 71, 929(1988).
(3) M. Vedula, R.N. Pangborn, and R.A. Queeney, Composites, 19, 133(1988).
(4) M. Vedula, R.N. Pangborn, and R.A. Queeney, Composites, 19, 55(1988).
(5) J.C. Romine, Ceram. Eng. Sci. Proc., 8, 411(1987).
(6) K.M. Merz, W.R. Brown, and H.P. Kirchner, J. Am. Cer. Soc., 45, 531(1962).
(7) A. Maheshwari, K.K. Chawla, and T.A. Michalske, Mater. Sci. and Eng., 25, 363(1989).
(8) K.K. Chawla, R. Venkatesh, A. Choudhary, and J.R. Hellmann, to be published.
(9) K.K. Chawla, M. Ferber, and R. Venkatesh, to be published.

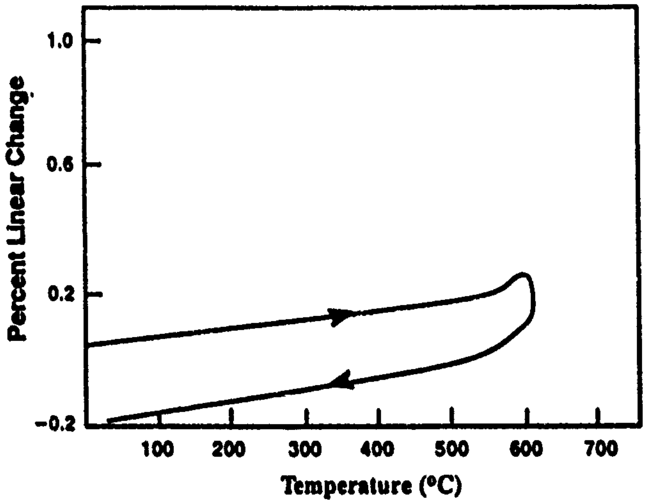

Fig.1 Thermal expansion and contraction of N51A glass. On cooling from 600 °C structural relaxation of the glass occurs up to 500 °C.

APPENDIX I: REPORT DISTRIBUTION

Addressees	Number of Copies
Scientific Officer Code : 1131N Steven G. Fishman Office of Naval Research 800 North Quincy Street Arlington, Virginia 22217-5000	3
Administrative Grants Officer Office of Naval Research Resident Representative N68583 Administrative Contracting Officer University of New Mexico, RM 204 Bandelier Hall West Albuquerque, New Mexico 87131-0001	1
Director, Naval Research Laboratory Attn : Code 2627 Washington, DC 20375	6
Defense Technical Information Center Building 5, Cameron Station Alexandria, Virginia 22314	12
Mr. W.D. Peterson New Mexico Tech Socorro, New Mexico 87801	1